University of Alberta

Asymptotic Descriptions of Seismic Waves

by

Jeremy B. Gallop ©

A thesis submitted to the Faculty of Graduate Studies and Research in partial fulfillment of the requirements for the degree of Doctor of Philosophy

in

Geophysics

Department of Physics

Edmonton, Alberta

Fall 1999

National Library
of Canada

Acquisitions and
Bibliographic Services

395 Wellington Street
Ottawa ON K1A 0N4
Canada

Bibliothèque nationale
du Canada

Acquisitions et
services bibliographiques

395, rue Wellington
Ottawa ON K1A 0N4
Canada

Your file Votre référence

Our file Notre référence

The author has granted a non-exclusive licence allowing the National Library of Canada to reproduce, loan, distribute or sell copies of this thesis in microform, paper or electronic formats.

L'auteur a accordé une licence non exclusive permettant à la Bibliothèque nationale du Canada de reproduire, prêter, distribuer ou vendre des copies de cette thèse sous la forme de microfiche/film, de reproduction sur papier ou sur format électronique.

The author retains ownership of the copyright in this thesis. Neither the thesis nor substantial extracts from it may be printed or otherwise reproduced without the author's permission.

L'auteur conserve la propriété du droit d'auteur qui protège cette thèse. Ni la thèse ni des extraits substantiels de celle-ci ne doivent être imprimés ou autrement reproduits sans son autorisation.

0-612-46838-0

Canada

University of Alberta

Library Release Form

NAME OF AUTHOR:	Jeremy B. Gallop
TITLE OF THESIS:	Asymptotic Descriptions of Seismic Waves
DEGREE:	Doctor of Philosophy
YEAR THIS DEGREE GRANTED:	1999

Permission is hereby granted to the University of Alberta Library to reproduce single copies of this thesis and to lend or sell such copies for private, scholarly or scientific research purposes only.

The author reserves all other publication and other rights in association with the copyright in the thesis, and except as hereinbefore provided neither the thesis nor any substantial portion thereof may be printed or otherwise reproduced in any material form whatever without the author's prior written permission.

Jeremy B. Gallop
Apt.408
9903 104th Street NW,
Edmonton, AB,
T5K 0E4

May 11, 1999

"I hate to disappoint you, sir, but I am afraid that the salary is not adequate. An oil magnate is currently dangling thousands before me trying to tempt me to be his personal secretary. At the moment, I am trying to decide whether I can accept the man's materialistic worldview. I suspect that I am going to finally tell him, 'Yes.'"
"We'll include twenty cents a day for carfare," Mr. Gonzalez pleaded.
"Well. That does change things.", Ignatius conceded.

A Confederacy of Dunces

University of Alberta

Faculty of Graduate Studies and Research

The undersigned certify that they have read, and recommend to the Faculty of Graduate Studies and Research for acceptance, a thesis entitled **Asymptotic Descriptions of Seismic Waves** submitted by **Jeremy B. Gallop** in partial fulfillment of the requirements for the degree of Doctor of Philosophy in Geophysics.

M. Sacchi (Supervisor)

E S Krebes

E. Krebes (External)

M. R

M. Razavy (Chairman)

H V Roessel

H. Van Roessel

W. Jones

T. Spanos

DATE: May 7, 1999

Abstract

The calculation of seismic waves in complex media is an area which still contains challenges to be met. When considering Cagniard's problem, where a plane interface separates homogeneous isotropic media, high frequency asymptotic representations are known to break down at critical angles of incidence. Formulae have previously been derived to correct this, to be used in conjunction with regular asymptotic expressions. We present formulae which are more generally applicable, since we account for the contribution of leaky modes, which can be asymptotically significant. We therefore arrive at a series of approximations based on the ray approach, which model seismic waves in a plane layered system.

The diffraction of seismic waves is also a stumbling block for regular asymptotic expressions until relatively recently. There now exist approximations that smooth abruptly truncated wavefields calculated by zero order Asymptotic Ray Theory, which play the role of diffractions. We present an example of how to compute these diffractions for a complex model. The question as to whether diffracted waves calculated in the aforementioned manner can actually cross additional interfaces has not been addressed until now. We show that these waves do in fact satisfy boundary conditions, and point out some limitations of their applicability.

Acknowledgements

I would like to acknowledge the late Franta Hron for his constant support and encouragement. In addition, thanks are due to the UGL who gave me access to their computational facilities, and saved my sanity.

Preface

While broadly classified as an investigation of asymptotic descriptions of seismic waves, the thesis really has two distinct parts. Chapters 1 through 3 deal with waves in the specific geometry of plane layered homogeneous media. New formulae are derived and applied to characterize the different seismic phases. In Chapter 4 we change gears quite a bit and look at diffracted waves, the descriptions of which can be applied in far more complicated media. We follow the results of others (mainly K.D. Klem-Musatov), providing numerical examples and covering a small theoretical point that has been overlooked in the literature. The latter topic was carried out at the beginning of the Ph.D., and has been published in two papers. The results found in the first three chapters have only recently been submitted for publication.

J.B.G.

Contents

1 Asymptotic Techniques **1**
- 1.1 Introduction 1
- 1.2 Exact Seismic Response in Cagniard's Problem 2
- 1.3 Steepest Descents Approximations 6
  - 1.3.1 Dominant Points in Ray Parameter Plane 7
  - 1.3.2 The Reflected Wave 8
  - 1.3.3 The Head Wave 9
  - 1.3.4 The Leaky Wave 10
  - 1.3.5 Generalization to Many Layers 14
- 1.4 Non-Uniform Approximations 15
  - 1.4.1 Example: a pole-saddle-branch point interference 18
  - 1.4.2 Case Formulae 21
  - 1.4.3 Relative Importance of Terms 25
  - 1.4.4 Boundary Layers 26
  - 1.4.5 Phase Corrections for the Non-Uniform Expansion 28
- 1.5 Uniform Asymptotic Approximation 32
- 1.6 Method of Červený and Ravindra 39
- 1.7 Chapter Summary 43

2 Numerical Results **44**
- 2.1 Introduction 44
- 2.2 Location of Poles 44
- 2.3 Harmonic Wave Amplitude Curves 50
- 2.4 Seismograms 56
- 2.5 Chapter Summary 67

3 Numerical Techniques **70**
- 3.1 Introduction 70
- 3.2 Real Contour Method 71
  - 3.2.1 Filon's Method 75
  - 3.2.2 Generalized Filon Method 75
- 3.3 Complex Contour 79

3.4 Special Functions 84
    3.4.1 $D_{1/2}(z)$ and $D_{3/2}(z)$ 84
    3.4.2 $D_{-1}(z)$ 85
    3.4.3 $\mathcal{F}(z,w)$ 87
3.5 Finding Roots 88
3.6 Chapter Summary 90

4 Edge Diffracted Waves **91**
4.1 Introduction 91
4.2 Review of Theory 92
    4.2.1 Polarization 95
    4.2.2 Continuation of the Geometrical Eikonal 95
    4.2.3 Continuation of the Geometrical Amplitude 97
4.3 Diffracted Waves at Interfaces 97
    4.3.1 Interface Complications 102
4.4 Numerical Example: The Amoco Model 104
    4.4.1 Interface Complications 114
4.5 Chapter Summary 114

Conclusions **116**

A Truncated Steepest Descents Contour **118**

B Asymptotic Series Proof **121**

C Perturbations of function $W(w)$ **125**

List of Figures

1.1 Model geometry. 3
1.2 Pre-Critical contours of integration in the complex ray parameter plane. 6
1.3 Post-critical contour of integration in complex ray parameter plane. . . 8
1.4 Time domain picture of leaky pulse. 13
1.5 Transformation of steepest descents contour. 20
1.6 Error in replacing Parabolic Cylinder Functions with their asymptotic terms (part 1). 28
1.7 Error in replacing Parabolic Cylinder Functions with their asymptotic terms (part 2). 29
1.8 Another transformation of the steepest descents contour. 31
1.9 The descent contour of Červený and Ravindra. 41

2.1 Distances from saddle point to poles on different Riemann Sheets. . . 46
2.2 Contour plot of poles on $(-++\!+)$ sheet (part 1). 48
2.3 Contour plot of poles on $(-++\!+)$ sheet (part 2). 48
2.4 Contour plot of poles on $(--++)$ sheet (part 1). 49
2.5 Contour plot of poles on $(--++)$ sheet (part 2). 49
2.6 AVO: The zero order ART approximation to the reflected P-wave from the first interface. 51
2.7 AVO: Comparison of numerical and asymptotic results for the P-wave reflection from the bottom of layer 1. 52
2.8 AVO: The zero order ART approximation to the reflected P-wave from the third interface. 52
2.9 AVO: Comparison of numerical and asymptotic results for the P-wave reflection from the bottom of layer 3. (part 1) 53
2.10 AVO: Comparison of numerical and asymptotic results for the P-wave reflection from the base of layer 3 (part 2). 53
2.11 AVO: Comparison of numerical and asymptotic results for the P-wave reflection from the base of layer 3 (part 3). 54
2.12 AVO: Comparison of numerical and asymptotic results for the P-wave reflection from the base of layer 3 (part 4). 54
2.13 Seismograms: Zero order ART approximation to the reflected wave from the first interface. 59

2.14 Seismograms: The exact reflected P-wave from the first interface. . . . 59
2.15 Seismograms: The reflected P-wave from the first interface calculated by Case formulae. 60
2.16 Seismograms: The difference between the exact and zero order ART reflections from the first interface. 60
2.17 Seismograms: The difference between the exact and asymptotic (Case formulae) reflections from the first interface. 61
2.18 Seismograms: The zero order ART approximation of the reflected wave from the third interface (adjusted model). 61
2.19 Seismograms: The exact reflected wave from the third interface (adjusted model). 62
2.20 Seismograms: The asymptotic reflected wave from the third interface (adjusted model). 62
2.21 Seismograms: Error in ART for reflection from third interface (adjusted model. 63
2.22 Seismograms: Error in asymptotic (non-uniform formulae) for the reflection from third interface (adjusted model). 63
2.23 Seismograms: Leaky pulse from the third interface (adjusted model). . 64
2.24 Comparison of normalized average error for ART and exact seismograms. 68
2.25 Comparison of normalized average error for non-uniform asymptotic and exact seismograms. 68

3.1 Numerical integrations: real axis 129 pt. trapezoidal scheme. 73
3.2 Numerical integrations: real axis 257 pt. trapezoidal scheme. 74
3.3 Numerical integrations: real axis 129 pt. generalized Filon method scheme. 79

4.1 Diffraction geometry. 93
4.2 Cross section of boundary layer amplitude. 94
4.3 Diffracted waves incident upon a smooth interface. 98
4.4 Diffracted waves incident upon a non-smooth interface. 103
4.5 The Amoco model. 105
4.6 The zero order ART response to the Amoco model with and without diffractions. 107
4.7 Ray diagrams containing sample rays for the six dominant arrivals of zero order ART. 108
4.8 Partial diffractions (part 1). 109
4.9 Partial diffractions (part 2). 110
4.10 Partial diffractions (part 3). 111
4.11 Partial diffractions (part 4). 112
4.12 Boundary complications. 115

List of Tables

2.1 Salt Model Parameters 51

Chapter 1

Asymptotic Techniques

1.1 Introduction

The seismic response of a single plane interface separating homogeneous, isotropic media (Cagniard's Problem) has been extensively studied, with analyses being carried out using both Fourier and Laplace transforms. The former usually result in high frequency asymptotic approximations, while the latter can be used to find the exact time domain response (see Aki and Richards, 1980 for a summary of techniques). Regular asymptotic approximations have a rather limited applicability, as they are invalid for some angles of incidence (close to critical angles). Červený and Ravindra (1971) and Brekhovskikh (1980) derived similar high frequency solutions that are valid near critical angles, for elastic and acoustic waves respectively. Smirnova (1966) also studied this problem. However, these formulae prove to be inaccurate for a large suite of geologic models. Previous derivations have neglected the presence of leaky wave singularities close to branch points, and we give formulae for more generally valid asymptotic expansions. The latter combined with regular asymptotic formulae are less costly to compute than a numerical integration of the exact formula. They also generalize to a (homogeneous) multi-layered structure, when one desires a ray-based solution. When curved interfaces and inhomogeneity are modelled, one must use the more elaborate results of Thomson (1990), who has arrived at corrections to ray theory near critical angles for acoustic waves.

There has, in the past, been some resistance to the notion of lower Riemann sheet contributions to seismograms for the simple plane layer case (Gupta, 1970). However, Chapman (1972) utilized the exact nature of the Cagniard-deHoop method to demonstrate the role of leaky poles' contribution to seismograms for Lamb's Problem. We also aim to clarify the effects of leaky waves, including their influence upon the reflected P-wave, using an asymptotic frequency domain approach.

1.2 Exact Seismic Response in Cagniard's Problem

We are going to investigate the response of a layered system to a far-field point source. To make use of high frequency asymptotic approximations, we must construct a ray-based solution in its exact form. Ray solutions have the advantage that frequency is a factor only in the exponent (see for example Chapman, 1985), and this allows us to make use of a proper steepest descents approximation. The disadvantage of a ray decomposition is that an infinite set of rays is required to characterize the exact seismic response, and hence practically we are only modelling a partial wavefield (although this has interpretational advantages). Since we are looking at piecewise homogeneous media, potentials are adequate to describe the wavefield.

Aki and Richards (1980) show that for cylindrical symmetry we need only the scalar potentials Φ, Ψ and χ, such that

$$\mathbf{u} = \nabla\Phi + \nabla \times \nabla \times (0,0,\Psi) + \nabla \times (0,0,\chi) \tag{1.1}$$

in cylindrical coordinates (see Figure 1.1), and each potential must satisfy a scalar wave equation in order for the displacement $\mathbf{u}$ to satisfy the basic vector elastodynamic equation:

$$\rho\frac{\partial^2\mathbf{u}}{\partial t^2} = (\lambda + \mu)\nabla(\nabla \cdot \mathbf{u}) + \mu\nabla^2\mathbf{u}, \tag{1.2}$$

where λ and μ are the *Lamé* parameters and ρ is the density. The representation given in equation (1.1) also has the advantage in that each potential represents a particular type of wave, namely P, SV and SH from left to right. The potential χ decouples and propagates independently, while Φ and Ψ couple at horizontal interfaces. We use a spherically symmetric source potential

$$\Phi_0 = \alpha_1 \frac{e^{-i\omega(t-R/\alpha_1)}}{i\omega R} \tag{1.3}$$

which approximates the displacement of a far-field P-wave located in the first medium. We shall set up the solution for the reflection from a single interface, and then later generalize to the multi-layered problem. Our coordinates are set up in Figure 1.1. Each potential must satisfy an equation of the form

$$c^2\nabla^2\eta = \frac{\partial^2\eta}{\partial t^2} \tag{1.4}$$

where we need not consider the source term, since the incident wave has been prescribed in equation (1.3). We can use separation of variables in cylindrical coordinates to find the general solution for either side of the interface:

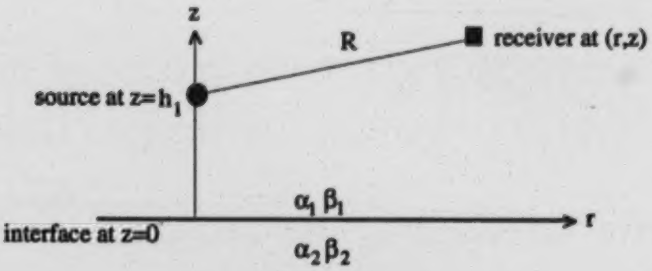

Figure 1.1: Model geometry.

$$\eta = \sum_{m=0}^{\infty} \int_{-\infty}^{\infty} \int_0^{\infty} F(\omega) \left[A_m(k)e^{i\nu z} + B_m(k)e^{-i\nu z}\right] e^{-i\omega t + im\phi} J_m(kr)\, dk\, d\omega \tag{1.5}$$

where $\nu = \sqrt{\omega^2/c^2 - k^2}$. The harmonic dependence of our source allows us to dispense with the inverse fourier transform. We can later use superposition to find the result for an arbitrary source time series, noting that we are assuming $\omega > 0$ throughout, and for negative frequencies we must take the complex conjugate of any results derived (see Červený and Ravindra, 1971; we shall hereafter refer to this book as C & R). The symmetry of the source allows us to discard all but the mode $m = 0$, and clearly the SH potential is identically zero. Potentials for upgoing and downgoing P and SV waves on either side of the interface can be written using a form similar to that in equation (1.5), choosing appropriate velocities. The source can be written in the same form (Aki and Richards, 1980):

$$\Phi_0 = \int_0^\infty J_0(kr) e^{i\nu_1|z-h_1|} \frac{\alpha_1 k}{-i\omega\nu_1} dk \tag{1.6}$$

where $Im(\nu_1) > 0$, and $c = \alpha_1$. Using this and equation (1.1) and Hooke's Law in cylindrical coordinates, one can equate displacements and traction across the interface and to find the coefficients A and B. The algebra is tedious and has been carried out in many places, so we do not repeat it here. The resulting exponents show the relative phase delay of the different rays, and the coefficients of the exponents are similar to the plane wave reflection/transmission coefficients, generalized to complex angles of incidence (where $k = \omega \sin\theta/c$ and θ is the angle of incidence). Explicit expressions for the coefficients can be found in C& R. We will only quote the result for the reflected P-wave, which we shall primarily be studying.

$$\Phi^{ref} = \frac{\alpha_1 e^{-i\omega t}}{\omega} \int_0^\infty R(k) J_0(kr) e^{i\nu_1(z+h_1)} \frac{k\,dk}{\nu_1} dk \tag{1.7}$$

is the reflected wave potential, and one needs to make several manipulations before it is in a form that can be easily approximated. One uses the identity

$$J_0(kr) = (1/2)[H_0^{(1)}(kr) + H_0^{(2)}(kr)] \tag{1.8}$$

and the fact that $R(-k) = R(k)$ along with $H_0^{(2)}(-kr) = -H_0^{(2)}(kr)$ to get the form

$$\Phi^{ref} = \frac{\alpha_1 e^{-i\omega t}}{2\omega} \int_{-\infty}^\infty R(k) H_0^{(1)}(kr) e^{i\nu_1(z+h_1)} \frac{k\,dk}{\nu_1} dk. \tag{1.9}$$

We also work in the complex ray parameter (p) domain so we must substitute $k = \omega p$.[1] By taking the gradient of the potential we get the displacement, and then we approximate the Hankel functions by the far offset approximation. This assumes $|\omega p r|$ is large, and is appropriate for the region that we are interested in studying (critical angles). To approximate the integral for near offsets one must use another expansion of the Hankel function. The result that we need is

$$\begin{bmatrix} u_z \\ u_r \end{bmatrix}^{ref} = \alpha_1 e^{i\pi/4 - i\omega t} \sqrt{\frac{\omega}{2\pi r}} \int_{C_0} R(p) e^{\omega\phi(p)} \begin{bmatrix} p^{1/2} \\ p^{3/2}\nu_1^{-1} \end{bmatrix} dp \tag{1.10}$$

where the exponent is $\phi(p) = i[rp + (h_1 + z)\nu_1]$. The contour is shown in Figure 1.2 along with a sample pre-critical angle steepest descents contour. The contour must avoid the origin due to the far offset approximation already made. The reflection coefficient is rather complicated and is given by

$$R = -1 + 2\nu_1 D^{-1}(\alpha_2\beta_2\nu_2 X^2 + \beta_1\alpha_2\rho_1\rho_2\nu_4 + q^2p^2\nu_2\nu_3\nu_4) \tag{1.11}$$

where

$$\begin{aligned} D &= \alpha_1\alpha_2\beta_1\beta_2 p^2 Z^2 + \alpha_2\beta_2\nu_1\nu_2 X^2 + \alpha_1\beta_1\nu_3\nu_4 Y^2 \\ &\quad + \rho_1\rho_2(\beta_1\alpha_2\nu_1\nu_4 + \alpha_1\beta_2\nu_2\nu_3) + q^2p^2\nu_1\nu_2\nu_3\nu_4 \\ q &= 2(\rho_2\beta_2^2 - \rho_1\beta_1^2),\ X = \rho_2 - qp^2,\ Y = \rho_1 + qp^2,\ Z = \rho_2 - \rho_1 - qp^2 \\ \nu_1 &= \sqrt{1/\alpha_1^2 - p^2},\ \nu_2 = \sqrt{1/\beta_1^2 - p^2},\ \nu_3 = \sqrt{1/\alpha_2^2 - p^2},\ \nu_4 = \sqrt{1/\beta_2^2 - p^2}. \end{aligned}$$

Most frequency domain formulations choose $Im\{\nu_j\} = 0$ for branch cuts; we choose $Re\{\nu_j\} = 0$, noting that the choice of branch cuts does not affect the results. We also use the notation of Phinney (1961) to denote positions on the eight sheeted Riemann surface. As we shall mainly look at the case for which $\alpha_2 > \beta_2 > \alpha_1 > \beta_1$, our sheets are represented by

$$\Big(sgn(Re\{\nu_3\}), sgn(Re\{\nu_4\}), sgn(Re\{\nu_1\}), sgn(Re\{\nu_2\}) \Big).$$

---

[1] We note that such a substitution eliminates the frequency dependence from the coefficient $R(k)$, since we are using a ray-based expansion (normally the frequency dependence would remain).

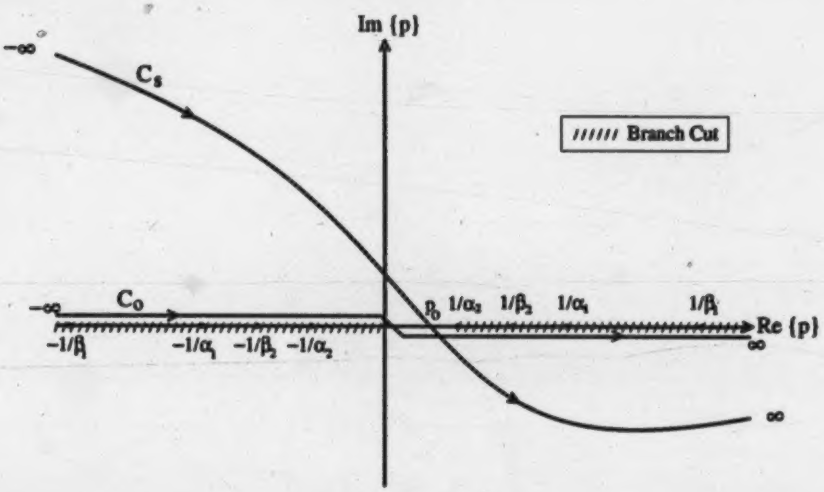

Figure 1.2: The contours of integration in the complex ray parameter plane. C_0 and C_s are the initial and steepest descents contours, respectively. Point p_0 represents the saddle point of the exponent.

The initial contour, C_0, must lie on the top Riemann sheet $(++++)$ so that the reflected wave is travelling away from the boundary. In addition, C_0 must lie in the quadrants for which $Im\{\nu_j\} \geq 0$, to assure boundedness of the integrand for $|z| \to \infty$. (We relax this slightly to avoid the singularity at the origin, arising from our far offset approximation). This contour can be deformed to the equivalent steepest descents contour, C_s, so long as one is careful to avoid points where $R(p)$ is not analytic. This may include excursions into other quadrants and Riemann sheets, and will not violate the boundedness condition, as we shall see.

1.3 Steepest Descents Approximations

This is a method for finding an approximate value for complex integrals of a certain type. One requires that the integral contain a large parameter, which in our case is the frequency.[2] The method of steepest descents is well known, and we shall not re-capitulate the theory here (see Bender and Orszag, 1978 for a good summary). Rather we shall assume some general knowledge of the method, and proceed to applying it to our particular problem.

1.3.1 Dominant Points in Ray Parameter Plane

The main observable seismic phases arise from an asymptotic analysis about dominant points in the integral in equation (1.10). There is one saddle point at which $\phi'(p_0) = 0,\ 0 < p_0 < 1/\alpha_1$, producing a reflected wave. The branch points at $p = 1/\alpha_2$ and $p = 1/\beta_2$ cause regular head waves, whereas the branch point at $p = 1/\beta_1$ gives rise to an inhomogeneous head wave. Depending upon the material parameters, there may exist top sheet poles on the real axis past $p = 1/\beta_1$, and these represent Stoneley interface waves. Finally, there are always a variety of lower sheet (leaky) poles present (Gilbert and Laster, 1962). In this thesis we shall not consider inhomogeneous head waves or Stoneley waves.

The steepest descents contour is shown in Figure 1.3 for a post-critical angle of incidence. Since the saddle point is now located on a branch cut, the contour must continue onto the lower sheet $(-+++)$. The contour must also loop around the branch point at $p = 1/\alpha_2$, and this loop has one leg on the $(++++)$ sheet and the other on the $(-+++)$ sheet. Also shown is a possible leaky pole location (p_L) which forces a residue to be taken, if the contour is to be deformed continuously from C_0. A second and similar loop contour would be drawn if $p_0 > 1/\beta_2$. We assume that p_0, p_L and $1/\alpha_2$ are sufficiently 'far apart' so that each contribution may be calculated independently. Later we shall make precise the meaning of 'far apart'. Below we give a brief review of the asymptotic contributions (for vertical displacement only), where each dominant point is considered independently. We shall give a slightly more detailed description of the leaky wave contribution, as this has not been documented satisfactorily in the frequency domain, in the literature

---

[2] Rigorous treatment requires the definition of a dimensionless parameter, such as $\omega/\alpha_1 \times$some intrinsic length scale. However, this is equivalent to proper interpretation of the results when using ω as our large parameter. It is common to use the latter method and we shall follow it throughout.

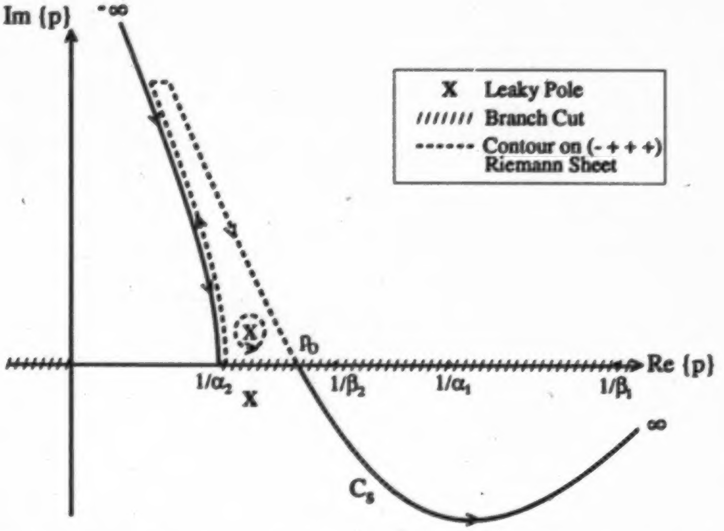

Figure 1.3: The steepest descents contour for a post-critical angle of reflection, which must loop about the branch point at $p = 1/\alpha_2$. Sample leaky poles from the $(- + ++)$ sheet are shown, one of which requires a residue.

1.3.2 The Reflected Wave

The well known reflected wave contribution looks like

$$
\begin{aligned}
u_z^{ref} &\sim \alpha_1 \frac{R(p_0)\sqrt{p_0}}{\sqrt{r}\,\rho} e^{-i\omega t+\omega\phi(p_0)}, \qquad \rho = |\phi''(p_0)|^{1/2} \\
&= \frac{R(p_0)\cos\theta_0}{L} e^{-i\omega(t-\tau)} \qquad (1.12)
\end{aligned}
$$

where $L = \sqrt{r^2 + (h_1 + z)^2}$ is the geometrical spreading, $R(p_0)$ is the plane wave reflection/transmission coefficient and τ is the travel time. Note that we have used the fact that $p_0 = \sin\theta_0/\alpha_1$. This is the zero order approximation, and the amplitude is frequency independent. The geometrical spreading is characterized by $\sqrt{\sin\theta_0/r}$ and $\sqrt{1/|\phi''(p_0)|}$; the first factor is the root of the radius of curvature of the wavefront perpendicular to the plane of incidence, and the second factor is proportional to the root of the radius parallel to the plane of incidence. (This is true for the multi-layered case as well). This result agrees with the zero order term of Asymptotic Ray Theory, which is not derived from an exact (closed form) representation of the wavefield. Details of the latter theory can be found in Hron and Kanasewich (1971).

1.3.3 The Head Wave

The head wave contribution can be written

$$\begin{aligned} u_z^{head} &\sim \alpha_1 \frac{\Gamma_{1k1}}{\omega\sqrt{r}\sqrt{r-r_c}} e^{-i\omega t+\omega\phi(p_b)+i\pi/2} \\ &= \frac{\alpha_1\Gamma_{1k1}}{\omega\sqrt{r}\sqrt{r-r_c}} e^{i\pi/2-i\omega(t-\tau_h)} \end{aligned} \tag{1.13}$$

where r_c is the critical offset ($r_c = (h_1+z)\tan\theta_c$), and Γ_{1k1} is the head wave coefficient whose relationship to $R(p_b)$ will be shown later (the Case 2 asymptotic formulae). If $k = 3$ or 4 then this is the head wave corresponding to a critically refracted P-wave or S-wave, respectively. The first and third numbers are 1 since we have specified an incident and reflected P-wave. There are 26 possible head wave types, and for these we refer to C&R. There are many properties of head waves documented in C& R, so we just point out the relevant major issues. Firstly, we see that the head wave term is $O(1/\omega)$, and would thus normally be considered negligible in the zero order approximation. However, the above expression is also singular at $r = r_c$, due to the confluence of the branch point with the saddle point in the complex-p plane. Thus there is a region surrounding the critical offset where special methods must be used to calculate the asymptotic behavior of the head and reflected waves.

1.3.4 The Leaky Wave

Leaky waves are less well known than the usual body phases, so we offer some introductory comments. A complete description can be found in the classic paper by Phinney (1961), and others (Gilbert and Laster, 1962). The leaky wave is a diffraction phenomenon associated with P and S-wave coupling at an interface. It arises from a singularity in the complex ray parameter plane (a zero in D in equation (1.11)). When the steepest descents contour crosses the simple pole singularity, a residue must be taken and this gives us the amplitude of the leaky wave. This is clearly similar to the Rayleigh and Stoneley waves, whose contributions also arise from a pole singularity. However, there are important differences. The Rayleigh and Stoneley poles lie on the real axis to the right of $1/\beta_1$ in the complex plane, so that the saddle point never interferes with the pole. Also, since their pole lies on the real axis, these waves propagate along the interface (decaying only geometrically) and are exponentially decaying in the direction perpendicular to the interface. Thus they are of little interest in reflection seismology, save for the Rayleigh waves propagating along the free surface. Leaky waves on the other hand, have *complex* pole locations lying on lower Riemann sheets. Thus they may decay or grow exponentially in the perpendicular direction from the interface, and decay exponentially parallel to it, so may be regarded only as quasi-interface waves. The pole is often located close to branch points, where the saddle may interfere. The real part of the pole location is associated with the propagation velocity of the pulse, although these waves are rarely observed independently, as they are low amplitude (and frequency) waves which often interfere with the regular reflected and head waves. Due to the fact that they travel faster than some body phases[3] (and slower than others), their energy may be radiated as the slower body phases,[4] which means that they 'leak' energy, and accounts for the fact that they decay exponentially along the interface. Thus their influence on reflected and head waves can be significant making them important in reflection or refraction seismology.

---

[3] Stoneley (Rayleigh) waves travel slower than all body waves, and their energy is trapped along an interface. Hence their amplitudes decay exponentially only away from the interface, and not along it.

We next look at the mathematical description of the leaky waves from asymptotic analysis to show how the properties mentioned above come to be. From the residue contribution (as shown in Figure 1.3) we find

$$u_z^{leaky} \sim \alpha_1 e^{-i\omega t + i3\pi/4 + \omega\phi(p_L)} \left(\frac{2\pi\omega}{r}\right)^{1/2} p_L^{1/2} R_L \tag{1.14}$$

with

$$R_L = Res_{p=p_L}\{R(p)\}.$$

The condition for which the residue need be evaluated is derived from the fact that $Im\{\phi(p)\}$ is constant along a steepest descents contour. Hence the residue is included if

$$Im\{\phi(1/\alpha_2)\} < Im\{\phi(p_L)\} < Im\{\phi(p_0)\}, \qquad Im\{p_L\} \geq 0 \tag{1.15}$$

Since $Im\{\phi(p_0)\} = \tau$, the reflected wave travel time, and $Im\{\phi(1/\alpha_2)\} = \tau_h$, the head wave travel time, we see that the leaky wave arrives between the head wave and reflected wave on the seismogram. Given that the residue was added when crossed by the steepest descents contour, and remains in a descent region after the contour has passed, it follows that $Re\{\phi(p_L)\} < 0$. Thus, u_z^{leaky} is itself negligible when considering the leading asymptotic behavior, since it is exponentially small as $\omega \to \infty$. However, as we shall see in the next section, the leaky pole produces an asymptotically significant contribution to the seismogram when it is located sufficiently close to the branch point or saddle point. The two general characteristics of the leaky pulse mentioned above are identical in the work of Chapman (1972), and Gilbert and Laster (1962), who did not use a frequency domain method to compute seismograms. They found the leaky pole contribution to be a broad and low amplitude pulse arriving between the reflected and head waves.

---

[4] This can be seen through the use of Snell's Law.

Since the pole lies in the first quadrant (on the sheet $(- + ++)$) it is clear that $Im\{\sqrt{1/\alpha_1^2 - p_L^2}\} < 0$, making the real coefficient of z positive in the exponent. From a plane wave perspective, this leads to an apparent violation of the boundedness condition for the integrand, for z large. However, for the spherical wave we see that $z \rightarrow \infty \Longrightarrow p_0 \rightarrow 0$, removing the residue. One would expect an initial increase followed by a decrease in amplitude of the leaky pulse when moving away from the interface, as has been touched upon by Brekhovskikh (1980). The real coefficient of r in the exponent is negative, making the leaky pulse decay exponentially with epicentral distance. We therefore conclude that the leaky pole will have maximum influence upon the seismogram when the pole has just been crossed by the steepest descents contour, which corresponds in the time domain to the leaky pulse interfering with (emerging from) the front of the reflected wave. Poles located to the left of the steepest descents contour which loops the branch point will not contribute a residue, and their greatest influence will be exerted upon the interfering head and reflected waves near (and just past) the critical angle.

We can view a typical leaky pulse given by equation (1.14) in the time domain, since it is possible to carry out the inverse Fourier transform exactly. We can write for a general input time series $f(t) \leftrightarrow F(\omega)$,

$$u_z^{leaky}(r, z, t) \sim \alpha_1 \left(\frac{2\pi}{r}\right)^{1/2} \left|p_L^{1/2} R_L\right| \cdot f(t - \tau_L) \star g(t) \tag{1.16}$$

where

$$g(t) = \frac{\partial}{\partial t} \frac{e^{i\pi/2}}{2\pi} \int_{-\infty}^{\infty} \frac{sgn(\omega)}{\sqrt{|\omega|}} e^{i\theta sgn(\omega) - |\omega| a - i\omega t}\, d\omega. \tag{1.17}$$

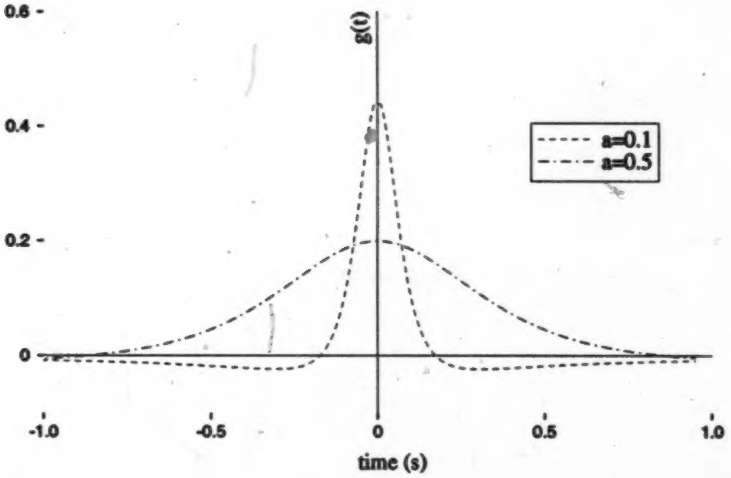

Figure 1.4: Time domain picture of leaky pulse. See text for explanation of parameter '*a*'.

and $\star$ denotes convolution. Above we have collected the phase into two terms, namely,

$$\theta = \arg(\sqrt{p_L}R_L) + 3\pi/4 \tag{1.18}$$

$$\tau_L = Im(\phi(p_L)) \tag{1.19}$$

where the latter can be though of as a leaky wave 'travel time'. Also we have used $Re(\phi(p_L)) = -a$, $a > 0$, which quantifies the attenuation of the pulse (a depends upon z and r). After some manipulation one finds that

$$g(t) = \frac{t}{2\sqrt{2\pi}(a^2+t^2)^{3/2}}\left[\frac{sgn(t)\cos\theta(a - 1/2\sqrt{a^2+t^2})}{\left(\sqrt{a^2+t^2}-a\right)^{1/2}} + \frac{\sin\theta(a + 1/2\sqrt{a^2+t^2})}{\left(\sqrt{a^2+t^2}+a\right)^{1/2}}\right]. \tag{1.20}$$

The phase of the pulse is usually non-zero, and depends upon the pole location.[5] We plot $g(t)$ in Figure 1.4 assuming zero phase, for two different attenuation constants. We see that the leaky pulse gets larger for smaller a, and approaches a delta function in the limit.

---

[5] It is not fixed for all cases like the pre-critical reflected wave ($\theta = 0$) and the head wave ($\theta = \pi/2$).

1.3.5 Generalization to Many Layers

The formulae for displacement given in equation (1.10) can be extended to represent a ray that has travelled along a specific path in a layered structure. In this case one must identify the path of interest and then change both $R(p)$ and $\phi(p)$ accordingly. We can use the same geometry as in Figure 1.1, and denote the thickness of the j^{th} layer by h_j $(j > 1)$. The primary P-wave reflected from the n^{th} interface (at the bottom of the n^{th} layer) can be written using equation (1.10) using the following substitutions:

$$\phi = i(pr + (h_1 + z)\nu_1^\alpha + 2\sum_{j=2}^{n} \nu_j^\alpha h_j) \tag{1.21}$$

where we must now define $\nu_j^\alpha = \sqrt{1/\alpha_j^2 - p^2}$. We us the notation of Aki and Richards (1980) which describes the upgoing and downgoing reflection and transmission coefficients:

$$R(p) = \grave{P}\acute{P}_n \prod_{j=1}^{n-1} \grave{P}\grave{P}_j \acute{P}\acute{P}_j, \tag{1.22}$$

where the reflection transmission coefficients are functions of ν_j^α and ν_j^β, $j = 1, ..., n+1$. The $\acute{P}$ and $\grave{P}$ symbols represent upgoing and downgoing P-waves, respectively. Labelling the Riemann sheets now becomes a little awkward, as there are now $4(n+1)$ sheets describing the surface. Similar substitutions can be found for a ray with any number of legs (i.e. multiples) and conversions. Again there is only one saddle point where $\phi'(p_0) = 0$, since we are dealing with a single ray. We have assumed that the P-wave is not evanescent, otherwise we cannot use a ray description to show its path (i.e. it would be a non-geometrical arrival). Therefore our offset is restricted so that the saddle point is situated where $\phi(p_0)$ is purely imaginary. This means that

$$0 < p_0 < 1/\alpha_j,\ 1/\beta_j, \qquad j = 1, ..., n. \tag{1.23}$$

However, it is still possible for $p_0 > 1/\alpha_{n+1}, 1/\beta_{n+1}$, which would give rise to loop contours and hence head wave contributions (similar to the single interface problem). Although we see that the branch point or leaky pole which may interfere with the saddle point are contained in the factor $\grave{P}\acute{P}_n$, the entire term in equation (1.22) is used in evaluating residue and branch point contributions. This accounts for the particular seismic phase's diminished influence at the surface, after passing through multiple interfaces. We shall continue to focus on the reflection from a single interface, noting that with the above substitutions our method is valid for a ray in a layered structure.

1.4 Non-Uniform Approximations

This section serves to demonstrate how to generate a non-uniform expansion that is accurate as critical points in an integrand coalesce. We use a very general notation, so that the nature of the approximation is made clear without cumbersome detail. In contrast to the steepest descents method, this is not commonly used, and hence it is worth looking at closely. Even so, we relegate any proofs needed (although they may be intuitively reasonable) to Appendices A and B, as they are not essential to understand the result. We then illustrate the method for a pole, branch point and saddle point in proximity, to go from the general to the specific, for one possible case. In the next section we shall present the specific formulae for different cases that arise in the study of our reflected P-wave, without derivation. We assume an integral of the form

$$I = \int_{C_s} f(p) e^{\omega\phi(p)}\, dp \tag{1.24}$$

where C_s is the steepest descents contour through the saddle point, p_0. Since f and ϕ are frequency independent, and ϕ contains a saddle point, this method is restricted to finding ray-based solutions. We truncate C_s, keeping only the portion in the vicinity of the saddle point, $\tilde{C}_s$. This introduces asymptotically negligible errors,[6] and we can now approximate $\phi(p)$ in a Taylor expansion (to second order) about the saddle, and we call this $\psi(p;p_0)$. We label the region surrounding the saddle point for which this expansion is valid D. Thus

$$I \sim \int_{\bar{C}_s} f(p) e^{\omega\psi(p;p_0)}\, dp. \tag{1.25}$$

We point out that this differs from the method of Bleistein and Handelsman (1986) who transforms $\phi(p)$ to a canonical exponent, instead of approximating it; our result applies only when critical points in $f(p)$ lie close to the saddle point. As the saddle point moves past the critical point a contour must necessarily loop the latter, and the above approximation of the exponent shall introduce errors. Therefore it is important to use more than one asymptotic expansion depending upon the saddle point's proximity to the critical point (i.e. this is a non-uniform approximation).

We next identify a set of critical points of $f(p)$, namely $\{p_k\}$ $k = 1, 2, ..., N$, which are assumed to be 'close' in the complex p plane. By this we mean that the sum of the first terms of the regular asymptotic expansions calculated for each point independently are inaccurate. The function $f(p)$ can be written as a product of functions, one of which is locally smooth in the region D.[7] Specifically,

$$f(p) = C(p;p_k)S(p) \tag{1.26}$$

where $S(p)$ is the smooth function in D. As an example of this, the reflection coefficient in the vicinity of the branch point $1/\alpha_2$ could be expressed as

$$R(p) = A(p) + B(p)\sqrt{1/\alpha_2 - p} \tag{1.27}$$

where A and B are smooth in some region surrounding $p = 1/\alpha_2$. The same can be done in the vicinity of a pole, or a combination of poles and branch points. The next step is to expand $S(p)$ using the well known Lagrange interpolation formula, making the polynomial exact at the $N+1$ points $\{p_k\}$, $k = 1, ..., N$ and the saddle p_0. Thus

---

[6] See Appendix A; this is only strictly valid for the contour passing through the saddle (and not those looping branch points).

[7] The integrand only contains branch points and poles of finite order, so one can always multiply and divide by the appropriate function to create a product of smooth and non-smooth functions.

$$S(p) = L_N(p) + e_N(p) \tag{1.28}$$

where

$$L_N(p) = \sum_{k=0}^{N} l_k(p) S(p_k) \qquad l_k = \prod_{j=0}^{N} \frac{p - p_j}{p_k - p_j},\ j \neq k$$

and e_N is the remainder from an N^{th} order interpolating polynomial, having the form

$$e_N(p) = \eta_N(p) \prod_{j=0}^{N} (p - p_j).$$

The above formula requires that p_k, $k = 0, 1..., N$ all be distinct, which is not always the case (e.g. for $p_0 \to 1/\alpha_2$). The coefficients of the powers of p can be re-arranged into forms which exist in the limit as critical points coalesce. This also puts the integrals in a form that is more easily recognizable in terms of special functions. If we write

$$\Phi_0 = \sum_{k=0}^{N} S(p_k) \int_{\tilde{C}_s} C(p; p_k) l_k(p) e^{\omega\psi(p;p_0)}\, dp \tag{1.29}$$

then an asymptotic sequence of functions, $\{\Phi_j\}$, may be found by repeating the above process, where the functions $\eta_N(p)$ are interpolated to find higher order terms in the sequence. One would need to include the neglected part of $\phi(p)$ for the higher order terms in the asymptotic sequence to have any relevance. Finally, it can be shown[8] that for $|\omega\phi''(p_0)/\alpha_1^2| \to \infty$,

$$I \sim \sum_{j=0}^{\infty} \Phi_j,\ \ \{\phi_j\} \tag{1.30}$$

where $\{\phi_j\}$ is an appropriately chosen auxiliary asymptotic sequence of functions. One can see that because $C(p; p_k)$ cannot be expanded in a series, Φ_0 will consist of a sum of integrals with parameters depending upon the distance between the points p_k, $k = 0, \ldots, N$. These integrals may in some instances be related to known special functions; otherwise they must be tabulated.

---

[8] This is fairly difficult for such a general formulation, and can be dealt with more easily on a case by case basis. In the example we shall derive specific formulae for one case, and prove the asymptotic nature of the series in Appendix B.

1.4.1 Example: a pole-saddle-branch point interference

Our starting point is the vertical component of the displacement of the reflected P-wave for a single interface, which was given in equation (1.10). We then recast the integrand using equation (1.27) and then expand the two functions as polynomials via

$$\begin{aligned}(p-p_L)A(p) &= \alpha_0 \frac{p-p_0}{p_L-p_0} + A(p_0)(p-p_L) + e_A(p) \qquad (1.31)\\ (p-p_L)B(p) &= \beta_0 \frac{(p-p_0)(p-p_b)}{(p_L-p_0)(p_L-p_b)} + B(p_b)\frac{(p-p_0)(p-p_L)}{(p_b-p_0)}\\ &\quad + B(p_0)\frac{(p-p_L)(p-p_b)}{(p_0-p_b)} + e_B(p). \qquad (1.32)\end{aligned}$$

where

$$\alpha_0 = Res_{p=p_L}A(p), \qquad \beta_0 = Res_{p=p_L}B(p). \qquad (1.33)$$

The above equations are exact, and the error in the polynomial approximation is represented by $e_A(p)$ and $e_B(p)$. We see that since A and B each contain a pole, the functions to be approximated by polynomials are $(p-p_L)A(p)$ and $(p-p_L)B(p)$. Due to the uniqueness of polynomial representations we can recast the above polynomials in the form

$$\begin{aligned}(p-p_L)A(p) &= a_0 + a_1(p-p_L) + e_A(p) \qquad (1.34)\\ (p-p_L)B(p) &= b_0 + b_1(p-p_L) + b_2(p-p_L)(p-p_b) + e_B(p) \qquad (1.35)\end{aligned}$$

which simplifies the integral representations.

Claim 1 *An asymptotic sequence of functions can be found*

$$\Phi_0 = a_{00}\int_{C_s} \frac{1}{p-p_L} e^{\omega\phi(p)}\,dp + a_{10}\int_{C_s} e^{\omega\phi(p)}\,dp$$

$$+b_{00}\int_{C_s}\frac{\sqrt{p_b-p}}{p-p_L}e^{\omega\phi(p)}\,dp+b_{10}\int_{C_s}(p_b-p)^{1/2}e^{\omega\phi(p)}\,dp$$
$$+b_{20}\int_{C_s}(p_b-p)^{3/2}e^{\omega\phi(p)}\,dp \tag{1.36}$$

and

$$\begin{aligned}\Phi_j &= \frac{a_{1j}}{\omega^j}\int_{C_s}e^{\omega\phi(p)}\,dp+\frac{b_{1j}}{\omega^j}\int_{C_s}(p_b-p)^{1/2}e^{\omega\phi(p)}\,dp\\ &\quad+\frac{b_{2j}}{\omega^j}\int_{C_s}(p_b-p)^{3/2}e^{\omega\phi(p)}\,dp \qquad j\geq 1\end{aligned} \tag{1.37}$$

and we claim that

$$u_z^{ref}\sim\sum_{n=0}^{\infty}\Phi_n, \qquad |\omega\phi''(p_0)|\to\infty \tag{1.38}$$

with respect to the auxiliary asymptotic sequence

$$\begin{aligned}\{\phi_j\} &= \frac{1}{|\omega\phi''(p_0)|^j}\left\{\left|\int_{C_s}e^{\omega\phi(p)}\,dp\right|+\left|\int_{C_s}(p_b-p)^{1/2}e^{\omega\phi(p)}\,dp\right|\right.\\ &\quad\left.+\left|\int_{C_s}(p_b-p)^{3/2}e^{\omega\phi(p)}\,dp\right|\right\}.\end{aligned} \tag{1.39}$$

There should be no confusion between the exponent ϕ and the sequence of functions $\{\phi_j\}$, the latter always having a subscript.

Proof 1 *We relegate the details of this to Appendix B.*

We take the zero order term as our approximation and can carry out some additional manipulation to put it in a form more amenable to calculation. The contour C_s may be truncated, and the exponent (ϕ) can be replaced by its Taylor expansion about the saddle,[9] as has been discussed earlier. Next the substitution

$$p=p_0+se^{i3\pi/4}/(\sqrt{\omega}\rho) \tag{1.40}$$

is made where $\rho=\sqrt{|\phi''(p_0)|}$. This puts the saddle at the origin, and rotates the contour. The contours can now be re-extended again without introducing significant errors. If we define

---

[9] $\psi(p;p_0)$ in our previous notation

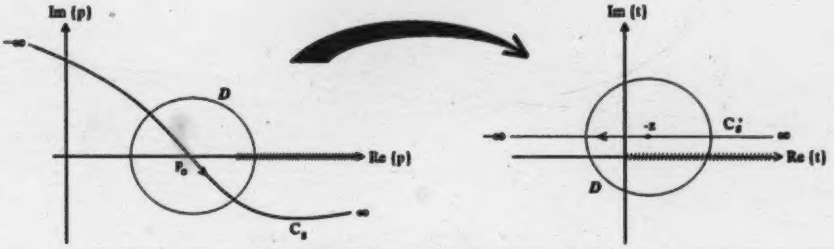

Figure 1.5: Transformation of steepest descents contour in complex plane (see text).

$$y = \sqrt{\omega}\rho e^{i\pi/4}(p_0 - p_L) \qquad z = \sqrt{\omega}\rho e^{i\pi/4}(p_0 - p_b) \tag{1.41}$$

then we quickly arrive at

$$u_z^{ref} \sim \alpha_1\sqrt{\frac{\omega}{2\pi r}}e^{i\pi/4-i\omega t+\omega\phi(p_0)}\int_{C_s'} ds\, e^{-s^2/2}\left\{\frac{a_0}{s-y} + \frac{a_1 e^{i3\pi/4}}{\sqrt{\omega}\rho}\right. \tag{1.42}$$

$$\left. + \frac{b_0 e^{-i\pi/8}}{\omega^{1/4}\rho^{1/2}}\frac{\sqrt{s-z}}{s-y} + \frac{b_1 e^{i5\pi/8}}{\omega^{3/4}\rho^{3/2}}\sqrt{s-z} + \frac{e^{-i5\pi/8}}{\omega^{5/4}\rho^{5/2}}(s-z)^{3/2}\right\}, \tag{1.43}$$

The roots in the above integrals are carried out on the top Riemann sheet, $\arg(s - z) \in [-3\pi/4, 5\pi/4)$; we chose the signs to agree with this arrangement. We next make the change of variables $t = s - z$ for the last three integrals, and $t = s - y$ for the first integral. We then employ the identities

$$\int_{C_s'} \sqrt{t}e^{-t^2/2-zt}\, dt = -\sqrt{2\pi}e^{i\pi/4+z^2/4}D_{1/2}(iz) \tag{1.44}$$

$$\int_{C_s'} t^{3/2}e^{-t^2/2-zt}\, dt = -\sqrt{2\pi}e^{i3\pi/4+z^2/4}D_{3/2}(iz) \tag{1.45}$$

$$\int_{C'} e^{-s^2/2}\, ds = -\sqrt{2\pi} \tag{1.46}$$

$$\int_{C_s'} \frac{1}{t}e^{-t^2/2-yt}\, dt = \sqrt{2\pi}e^{i\pi/2+y^2/4}D_{-1}(iy) \tag{1.47}$$

where the D_μ are parabolic cylinder functions. The final contour C_s' is shown in Figure 1.5 (substitute t-plane for p-plane). which leads to the final form of the Case 1 formula, given in the next section.

1.4.2 Case Formulae

We identify several cases in which two or three dominant points are sufficiently close in the complex ray parameter plane that standard asymptotic formulae become invalid. In each case we provide an asymptotic expansion which is accurate when the specified dominant points are 'close'. One might wonder why we find several different formulae, when one very general one would suffice. For example, a pole close to a saddle point could be modelled with a pole-saddle-branch point formula, putting the branch point far away. The goal of any asymptotic analysis is to seek the simplest possible representation for each case, which in turn increases the speed of computation. There is always a trade-off between simplicity and accuracy, the extreme being the original integral in equation (1.10), which is obviously accurate but cumbersome to compute. We therefore provide the simplest formula for any particular case that might arise.

Case 1: A simple pole, saddle point and branch point in proximity

$$\begin{aligned} u_z^{ref} \sim\ & \alpha_1 e^{-i\omega(t-\tau)} \left\{ a_0 \left(\frac{\omega}{\tau}\right)^{1/2} e^{i3\pi/4 - y^2/4} D_{-1}(iy) + \frac{a_1}{\tau^{1/2}\rho} \right. \\ & + b_0 \frac{\omega^{1/4} e^{i\pi/8 - z^2/2}}{(r\rho)^{1/2}} \mathcal{F}(z,w) + b_1 \frac{e^{i\pi/8 - z^2/4}}{\omega^{1/4}\tau^{1/2}\rho^{3/2}} D_{1/2}(iz) \\ & \left. + b_3 \frac{e^{-i5\pi/8 - z^2/4}}{\omega^{3/4}\tau^{1/2}\rho^{5/2}} D_{3/2}(iz) \right\}. \end{aligned} \tag{1.48}$$

Above, D_μ for $\mu = -1, 1/2, 3/2$, are parabolic cylinder functions (see Magnus and Oberhettinger, 1954), whereas $\mathcal{F}$ is not identifiable as a standard special function. It has the integral definition

$$\mathcal{F}(z,w) = \frac{-1}{\sqrt{2\pi}} \int_{-\infty}^{+\infty} \frac{\sqrt{t}}{t-w} e^{-t^2/2 - zt}\, dt \tag{1.49}$$

where the contour of integration passes above the singularity at $t = w$ as well as the branch point at the origin, and $Re\{\sqrt{t}\} > 0$ for $t \in \Re^+$. The variables in equation (1.48) are

$$\rho = |\phi''(p_0)|^{1/2} \qquad z = e^{i\pi/4}\sqrt{\omega}\rho(p_0 - p_b)$$

$$w = e^{i\pi/4}\sqrt{\omega}\rho(p_b - p_L) \qquad y = e^{i\pi/4}\sqrt{\omega}\rho(p_0 - p_L).$$

We have used, of course,

$$\sqrt{p}R(p) = A(p) + B(p)\sqrt{p_b - p}, \tag{1.50}$$

which relates our coefficients (below) to known quantities. The coefficients are

$$a_0 = Res_{p=p_L}\{A(p)\} \qquad b_0 = Res_{p=p_L}\{B(p)\} \qquad a_1 = A(p_0) - \frac{a_0}{p_0 - p_L}$$
$$b_1 = B(p_b) - \frac{b_0}{p_b - p_L} \quad b_2 = \frac{B(p_0) - B(p_b)}{p_0 - p_b} \quad b_3 = b_2 + \frac{b_0}{(p_0 - p_L)(p_b - p_L)}. \tag{1.51}$$

and are continuous in the limit $p_0 \to p_b$. Equation (1.48) expresses the interference between the reflected wave, a head wave and a leaky wave, although the individual form of each of these waves is not apparent in the above formula. It can be further augmented in a similar manner to incorporate a second distinct pole location; this situation arises often close to the smallest branch point, where two complex conjugate poles are nearby, without being separated by a branch cut. We note that $B(p_b) = -\sqrt{2}\Gamma_{1k1}$, $k = 3, 4$, where Γ_{ijk} are the well known head wave amplitude coefficients (C&R).

Case 2: A saddle point and branch point in proximity

$$u_z^{ref} \sim \alpha_1 e^{-i\omega(t-\tau)}\left\{\frac{A(p_0)}{\tau^{1/2}\rho} + \frac{B(p_b)e^{i\pi/8 - z^2/4}}{\omega^{1/4}\tau^{1/2}\rho^{3/2}}D_{1/2}(iz) + \frac{b_2 e^{-i5\pi/8 - z^2/4}}{\omega^{3/4}\tau^{1/2}\rho^{5/2}}D_{3/2}(iz)\right\} \tag{1.52}$$

and all symbols are identical to Case 1. We have approximated A and B directly with polynomials, which are exact at $p = p_0$ and $p = p_b$. Note that this is a variation of the result given by C&R, describing the interference between a reflected and head wave. In their formula it is assumed that $b_2 \approx \left.\frac{dB}{dp}\right|_{p_b} \approx 0$, leaving only the $D_{1/2}$ term.

Case 3: A branch point and simple pole in proximity

This case describes the loop contour around the branch point for post-critical angles.

$$\begin{aligned} u_z^{ref} \;\sim\;& \alpha_1 \frac{\omega^{1/2} e^{-i\omega(t-\tau_h)+i\pi/4}}{\tau^{1/2} z_3^3} \left\{ b_2/\sqrt{2} - b_0\sqrt{2} z_3^2 \left(1 - y_3 e^{y_3^2/4} D_{-1}(y_3)\right)\right\} \\ & + \text{saddle point contribution} \end{aligned} \tag{1.53}$$

where several new variables need to be defined:

$$\rho_3 = |\phi'(p_b)|^{1/2} \qquad w_3 = e^{i\pi/4}\sqrt{\omega}\rho_3(p_b - p_L)$$
$$z_3 = e^{i\pi/4}\sqrt{\omega}\rho_3 \qquad y_3 = \sqrt{-2w_3 z_3}.$$

Equation (1.53) expresses the interference between a head wave and a leaky wave. The coefficients are the same as defined for Case 1, but there is no contribution from A since the contour loops the branch point (and A does not have a branch point at $p = p_b$). For this case a polynomial approximates $(p - p_L)B(p)$, and is exact at the points $p = p_b$ and $p = p_L$. Implicit in the derivation of the above equation was the assumption that $|\arg y_3| < 3\pi/4$, which serves to determine the sign of $\sqrt{-2w_3 z_3}$. The saddle point contribution is not specified because it can take more than one form. Above, we have only specified that a pole is close to a branch point, and the saddle point may be described by a regular asymptotic formula or another one of the case formulae, depending upon its position in the complex ray parameter plane relative to other dominant points.

Case 4: A saddle point and simple pole in proximity

The interference between the reflected wave and leaky wave is given by

$$\begin{aligned} u_z^{ref} \;\sim\;& \alpha_1 e^{-i\omega(t-\tau)} \left\{ \frac{1}{\sqrt{\tau}\rho} \left(p_0^{1/2} R(p_0) - \frac{p_L^{1/2} R_L}{p_0 - p_L} \right) \right. \\ & \left. + p_L^{1/2} R_L \frac{\omega^{1/2}}{\tau^{1/2}} e^{-y^2/4 + i3\pi/4} D_{-1}(iy) \right\} + \text{branch point contribution.} \end{aligned} \tag{1.54}$$

Again we do not give the precise branch point contribution, as we have made no assumption about the location of poles relative to branch points in deriving equation (1.54). The function we approximated by a polynomial was $\sqrt{p}R(p)(p-p_L)$, and this was made exact at $p=p_L$ and $p=p_0$.

More case formulae could be found, depending upon the media under study. The distance between branch points is a function of β_2/α_2 and α_1/α_2, and it is conceivable that two branch points (as well as a saddle point and poles) could interfere. Under Case 1 we mentioned that the formulae can be extended to accommodate more than one distinct (simple) pole. If we are to model rays in a multi-layered structure, multiple reflections from an interface near critical angles would give rise to poles in the integrand of order greater than unity; the methods used to derive these formulae would still apply, however the result would require new functions to be found, in addition to $\mathcal{F}$.

In equation (1.50) we have isolated the radical of interest, $\sqrt{p_b-p}$, which has made $A(p)$ and $B(p)$ functions of (p_b-p). An individual asymptotic analysis is carried out on each term. It is important to see that this division of $\sqrt{p}R(p)$ brings lower sheet poles to the top sheet in both A and B, forcing residues to be taken separately as the steepest descents contour crosses them. (Before bringing poles to the top sheet only a small subset required residues - see equation (1.15)). If a pole is situated such that no residue is warranted from the perspective of $\sqrt{p}R(p)$, it should cancel upon summation of the asymptotic terms from A and B. Cancellation errors can be catastrophic when carrying out the numerical computations, depending upon the locations of the poles. For $Im\{p_L\}<0$, the residues become exponentially large, and due to the finite precision of floating point number representation, cancellation is imperfect and the other terms in the formula are swamped. It is best to calculate both $\mathcal{F}$ and D_{-1} without any residues (so they are discontinuous functions) and as a final step in computation add in required residues according to equation (1.15). The following identity is useful:

$$D_{-1}(-y) = -D_{-1}(y) + \sqrt{2\pi}e^{y^2/4} \tag{1.55}$$

which we can use to find D_{-1} for a restricted range of argument, such that no residue is taken.

1.4.3 Relative Importance of Terms

We have seen that asymptotic expansions can be found when dominant points coalesce in the complex plane, if we use the methods outlined in Appendix B. The leading order terms are given as Case formulae, but one immediately notices that each term has a different frequency dependence.

Conjecture 1 *Can we truncate the Case formulae, retaining only the terms with the highest (positive) powers of ω?*

We illustrate using the Case 2 formulae, but the results apply to all. For Case 2, we might want to drop the term

$$\frac{b_2 e^{-i5\pi/8 - z^2/4}}{\omega^{3/4}\tau^{1/2}\rho^{5/2}} D_{3/2}(iz) \tag{1.56}$$

due to the presence of the $\omega^{-3/4}$ factor. Since the overall series was shown to be asymptotic in Appendix B, we need only show that

$$\lim_{\omega\to\infty} R = \lim_{\omega\to\infty} \left| \frac{\frac{b_2 e^{-i5\pi/8 - z^2/4}}{\omega^{3/4}\tau^{1/2}\rho^{5/2}} D_{3/2}(iz)}{\frac{A(p_0)}{\tau^{1/2}\rho} + \frac{B(p_b)e^{i\pi/8 - z^2/4}}{\omega^{1/4}\tau^{1/2}\rho^{3/2}} D_{1/2}(iz)} \right| = 0. \tag{1.57}$$

For the original leading order term Φ_0, we had similar functions (integrals) in the numerator and denominator in the above ratio (see Appendix B). Thus the fact that $\lim_{\omega\to\infty} R = 0$ was easily seen. More precisely, one could say that when using our original Φ_0, the above limit is approached uniformly: for any $\epsilon > 0$ there is a delta such that for $1/\omega < \delta$ and any point z, $R < \epsilon$ (δ only depends on ϵ). This is not necessarily true in equation (1.57); assuming that the limit is zero $\forall z$, we see that there is a pointwise convergence to the limit: for any $\epsilon > 0$ and any point z there is a δ such that whenever $1/\omega < \delta$, $R < \epsilon$ (in this case δ depends on ϵ and z).

The upshot is that one needs to investigate the above ratio of functions to make sure it is well behaved for the range of z for which Case 2 is required (see Boundary Layers). So long as the ratio is bounded one can make the truncation, but the result will be of *varying quality over the range of z* (due to the pointwise convergence mentioned above) and the overall quality will be determined by the peak value of the ratio. C&R took advantage of the size of the coefficients in Case 2, and showed that b_2 is often very small, making R small in turn. For the models they looked at the truncation proved adequate, although we prefer the generality of the Case formulae in their complete form.

1.4.4 Boundary Layers

We have, so far, made use of the concept of dominant points being 'close' in the complex ray parameter plane. In this section we clarify the exact definition of closeness, which involves defining boundary layers for our Case formulae, each with specific numerical limits in terms of known quantities.

The case formula in equations 1.48, 1.52 and 1.54 depend upon variables w, y, and z, of which only two are independent. These variables are, in turn, functions of the separation of the points p_0, p_b and p_L in the complex ray parameter plane, as well as frequency and $|\phi''(p_0)|$, which is proportional to the radius of curvature of the wavefront in the plane of incidence. If the variables have a large magnitude, the case formulae may be replaced with simpler expressions which match the regular asymptotic expansions. Thus for a given geologic model and signal spectrum, only a subset of the receivers and signal frequencies require the use of the case formulae, and we shall refer to these subsets as boundary layers.

For practical computation it is desirable to have a numerical estimate of the size of the boundary layers. As a rough guide we mark the boundary as the point at which the special function, of a given case formula, can be replaced by the leading term of its asymptotic expansion, such that the difference does not exceed some maximum percent of the original function. This, of course, is only an estimate as it does not bound the error in the overall formula, which clearly depends upon other factors.

Starting with Case 2, we look at replacing $D_{1/2}(iz)$ and $D_{3/2}(iz)$ for large $|z|$ by their leading terms, with one exception: for $\arg z = \pi/4$, we include the higher order term representing the head wave. Figure 1.6 shows that we expect a maximum error of about 10% if we make the boundary $|z| = 2$. Case 4 depends upon $e^{y^2/4}D_{-1}(y)$, which can be replaced by its leading term for $|y| \geq 4$, with an error between 5% and 10%, depending upon $\arg(y)$. The error boundary is plotted in Figure 1.7, where we only need consider $Re\{y\} > 0$ due to equation (1.55), and $Im\{y\} > 0$ due to the fact that $e^{\bar{y}^2/4}D_{-1}(\bar{y}) = \overline{e^{y^2/4}D_{-1}(y)}$ (the bar indicates complex conjugate). Case 3 has the same dependence on $D_{-1}(y)$, although it must be approximated by the leading two terms to provide the proper head wave contribution. This means that the boundary for Case 4 would overestimate the size of this layer (see Figure 1.7), since two terms can approximate the function better than one. We next make the assumption that the above boundaries in general reflect the limits of pole-saddle point, branch point-saddle point and branch point-pole influence. Using the above assumption (as well as $w_3z_3 \approx wz$), we defined the following tentative regions to represent the boundary layers:

$$C_1 = \{|z| \leq 2\} \cap \{|y| \leq 4 \cup |w| \leq 4\}$$

$$C_2 = \{|z| \leq 2\} \cap \{|y| > 4 \cup |w| > 4\}$$

$$C_3 = \{e^{-i\pi/4}z > 2\} \cap \{|\sqrt{2wz}| \leq 4\}$$

$$C_4 = \{e^{-i\pi/4}z > 2\} \cap \{|y| \leq 4\}.$$

where the C_k are the regions for the k^{th} case formula. The domain of regular asymptotic expansions is the complement of the set $C_1 \cup C_2 \cup C_3 \cup C_4$.

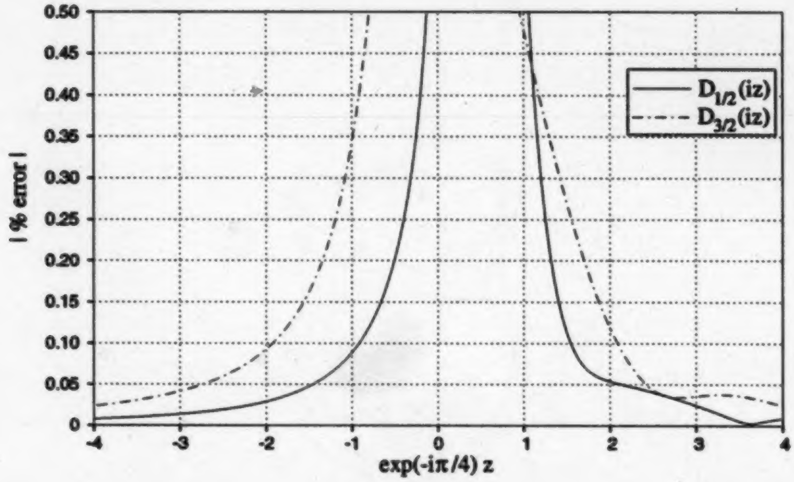

Figure 1.6: The error introduced by replacing the parabolic cylinder functions $D_{1/2}(iz)$ and $D_{3/2}(iz)$ with their leading order asymptotic terms. For post critical angles (i.e. $e^{-i\pi/4}z > 0$), we include the next term corresponding to the head wave contribution.

1.4.5 Phase Corrections for the Non-Uniform Expansion

The non-uniform expansion was found by approximating the exponent (ϕ) in the vicinity of the saddle point (p_0). We would expect this to be a poor approximation for the contour looping the branch point p_b[10] unless the saddle point is close by. Of course, for the non-uniform expansion we replace the formula by regular asymptotic expressions when the saddle is not close to the branch point. Here we conjecture that it is possible to have an unacceptable level of error within the boundary layers (obviously towards the edge) before we are able to replace the non-uniform expression with the regular asymptotic expressions. It should be pointed out that this situation has not been observed for any of the examples

---

[10] We are speaking of post-critical angles of reflection.

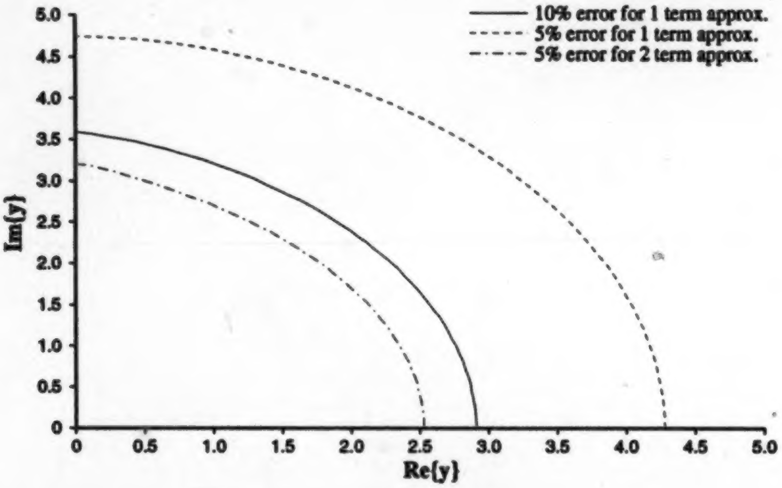

Figure 1.7: The boundaries at which $D_{-1}(y)$ can be replaced by one or two term approximations, for a given % error bound, labelled inset.

studied by the author, although a rather qualitative error tolerance was used. We have spoken only of the contour looping the branch point, but when a leaky pole is properly placed, a contour must loop this too (a residue is taken). However, the leaky pole contribution decays exponentially with offset, and so we find that at the edge of the boundary layer the residue is small enough that any errors from approximating the exponent locally are negligible (this is not so for branch points). To solve the problem for branch points, one can either engage a uniform approximation or try to correct the non-uniform one. In this section we look at the possible corrections, and in the following section we look at the uniform approximation. We shall focus on the pole-saddle-branch point problem as it is the most intricate, and all other case formulae may be treated in a similar manner. The way to correct the non-uniform approximation is to re-derive it, isolating each steepest descents contour. Thus, for post critical angles, referring to equation

(1.10) we can split the steepest descents contour as follows: $C_s = C_0 + C_b$ and

$$\begin{aligned} u_z^{ref} &\sim \alpha_1 e^{-i\omega t + i\pi/4}\sqrt{\frac{\omega}{2\pi r}}\left\{\int_{C_b} \frac{\sqrt{p-p_b}}{p-p_L} B(p) e^{\omega\phi(p)} + \int_{C_0} \sqrt{p} R(p) e^{\omega\phi(p)}\right\} \\ &= \alpha_1 e^{-i\omega t + i\pi/4}\sqrt{\frac{\omega}{2\pi r}}(I+J) \end{aligned} \tag{1.58}$$

where C_b is the contour looping the branch point and C_0 is the contour passing through the saddle point (the two join sufficiently far from the saddle).[11] We see that when rewriting the $\sqrt{p}R(p)$ as in equation (1.27), only the portion with the radical $\sqrt{p_b - p}$ is non-zero for the loop contour C_b. Clearly the non-uniform approximation made in section 1.4 *always* applies to the second integral (J), because the contour C_0 always passes through the saddle point. Thus we concentrate on the integral I, and will put the entire result together with J at the end.

Near the branch point we make the approximation

$$\phi(p) \sim \phi(p_b) + \phi'(p_b)(p - p_b) + (1/2)\phi''(p_b)(p - p_b)^2 \tag{1.59}$$

and we also expand the smooth function $B(p)$ in a polynomial, exact at the critical points as before in equation (1.32). If we introduce the transformation

$$p = p_b + s\frac{e^{i3\pi/4}}{\sqrt{\omega}\rho_b} \tag{1.60}$$

where $\rho_b = |\phi''(p_b)|^{1/2}$, then we get

$$\begin{aligned} I \sim \frac{e^{\omega\phi(p_b)}}{\omega^{1/4}\rho_b^{1/2}} &\left\{ b_0 e^{-i\pi/8}\int_{C_b'} \frac{\sqrt{s}}{s - w_b} e^{-s^2/2 - z_b s}\, ds + b_1 \frac{e^{i5\pi/8}}{\omega^{1/2}\rho_b}\int_{C_b'} \sqrt{s} e^{-s^2/2 - z_b s}\, ds \right. \\ &\left. + b_2 \frac{e^{i3\pi/8}}{\omega\rho_b^2}\int_{C_b'} s^{3/2} e^{-s^2/2 - z_b s}\, ds \right\}. \end{aligned} \tag{1.61}$$

Above we have introduced the variables which are similar to previous definitions except they are local to the branch point. As $p_0 \to p_b$ they become identical to the old definitions. Specifically, they are now

$$w_b = e^{i\pi/4}\sqrt{\omega}\rho_b(p_b - p_L) \qquad z_b = e^{-i\pi/4}\sqrt{\omega}\phi'(p_b)/\rho_b. \tag{1.62}$$

---

[11] We shall make the additional loop contour about the pole (if it is warranted) implicit in C_0.

We now employ the identities, taken from Bleistein and Handelsman (1986):

$$\int_{C_b'} \sqrt{s}e^{-s^2/2-zs}\, ds = -\sqrt{\pi}e^{z_b^2/4}D_{-3/2}(z_b) \tag{1.63}$$

$$\int_{C_b'} s^{3/2}e^{-s^2/2-zs} ds = -(3\sqrt{\pi}/2)e^{z_b^2/4}D_{-5/2}(z_b). \tag{1.64}$$

In addition, we modify the results of equation (1.48), to represent the contribution of J, which applies only to the contour C_0'. Figure 1.8 shows the three transformed contours C_b', C_0' and the original transformed steepest descents contour C_s'. We

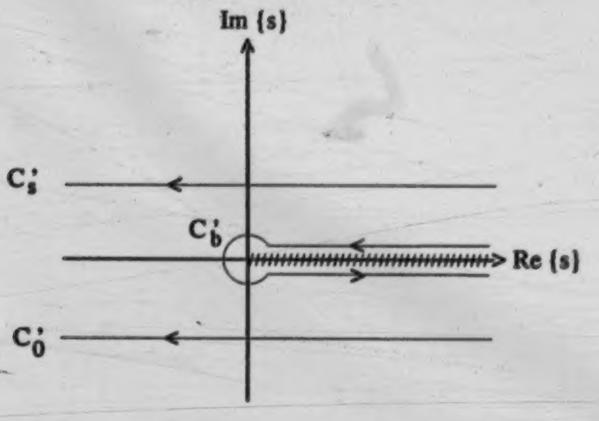

Figure 1.8: Transformation of the steepest descents contour using equation (1.60).

must use

$$\int_{C_0'} \sqrt{s}e^{-s^2/2-zs}\, ds = -\sqrt{2\pi}e^{i\pi/4+z^2/4}D_{1/2}(iz) + \sqrt{\pi}e^{z^2/4}D_{-3/2}(z) \tag{1.65}$$

$$\int_{C_b'} s^{3/2}e^{-s^2/2-zs} = \sqrt{2\pi}e^{-i\pi/4+z^2/4}D_{3/2}(iz) + (3\sqrt{\pi}/2)e^{z^2/4}D_{-5/2}(z). \tag{1.66}$$

Similarly, we must introduce a notation which differentiates $\mathcal{F}$ evaluated along the branch point and saddle point contours. Thus

$$\mathcal{F}_b(z_b, w_b) = \frac{1}{\sqrt{2\pi}}\int_{C_b'} \frac{\sqrt{s}}{s-w_b}e^{-s^2/2-z_bs}\, ds \tag{1.67}$$

$$\mathcal{F}_0(z, w) = \frac{1}{\sqrt{2\pi}}\int_{C_0'} \frac{\sqrt{s}}{s-w}e^{-s^2/2-zs}\, ds \tag{1.68}$$

and we point out for comparison that

$$\mathcal{F}(z,w) = \mathcal{F}_0(z,w) + \mathcal{F}_b(z,w). \tag{1.69}$$

Using these identities we can write a final result which has corrected the phase error introduced by the local approximation:

$$\begin{aligned}
u_z^{ref} \sim \alpha_1 e^{-i\omega t} \Bigg\{ & a_0 \sqrt{\frac{\omega}{\tau}} e^{i\omega\tau + i3\pi/4 - y^2/4} D_{-1}(iy) + \frac{a_1 e^{i\omega\tau}}{\sqrt{\tau}\rho} \\
& + \frac{b_0 \omega^{1/4} e^{i\pi/8}}{\sqrt{\tau}} \left[\frac{e^{i\omega\tau_h}}{\sqrt{\rho_b}} \mathcal{F}_b(z_b, w_b) + \frac{e^{i\omega\tau - z^2/2}}{\sqrt{\rho}} \mathcal{F}_0(z,w) \right] \\
& + \frac{b_1}{\omega^{1/4}\sqrt{\tau}} \left[\frac{e^{i\omega\tau - z^2/4 + i\pi/8}}{\rho^{3/2}} D_{1/2}(iz) + \frac{e^{i\omega\tau_h + z_b^2/4 - i\pi/8}}{\sqrt{2}\rho_b^{3/2}} D_{-3/2}(z_b) \right. \\
& \left. - \frac{e^{i\omega\tau - z^2/4 - i\pi/8}}{\sqrt{2}\rho^{3/2}} D_{-3/2}(z) \right] \\
& + \frac{b_2}{\omega^{3/4}\sqrt{\tau}} \left[\frac{e^{i\omega\tau - z^2/4 - i5\pi/8}}{\rho^{5/2}} D_{3/2}(iz) + \frac{3e^{i\omega\tau_h + z_b^2/4 + i5\pi/8}}{2\sqrt{2}\rho_b^{5/2}} D_{-5/2}(z_b) \right. \\
& \left. \left. - \frac{3e^{i\omega\tau - z^2/4 + i5\pi/8}}{2\sqrt{2}\rho^{5/2}} D_{-5/2}(z) \right] \right\}.
\end{aligned} \tag{1.70}$$

We see in the above formula that corrections are applied through the terms $D_{-3/2}(z)$ and $D_{-5/2}(z)$, which, as $z \to z_b$, disappear. Similarly, from equation (1.69) we see that corrections to $\mathcal{F}$ also disappear for $\rho \to \rho_b$ (i.e. $p_0 \to p_b$). In summary, we can correct for the phase errors introduced by truncating the exponent, by using a more cumbersome formula that contains functions that are similar to ones used in the original non-uniform formula.

1.5 Uniform Asymptotic Approximation

In this section we look at the result from a uniform approximation of the exact integral expressions. The result is said to be uniform with respect to the angle of incidence, and conveys that the approximation is valid for arbitrary angles. Note that this contrasts with regular asymptotic expressions (valid only away from critical angles) and our previous non-uniform approximation (valid only close to critical angles). This may sound like a superior result, and perhaps it is, in theory. However, we shall see that the added computational complexity involved is not worth the gain in universality (and elegance) of the expression. A better approach is to use a combination of non-uniform and regular asymptotic expressions to model the seismic wavefield. There is conceivably one instance in which the uniform expansion would be desirable. This would occur if the local approximations already developed contained unacceptably large errors near the edges of the boundary layers, caused by the truncation of the exponent (i.e. before we are able to use regular asymptotic formulae), as has been first pointed out in the last section. We shall go into some of the details of the derivation of the uniform expansion, as it has not been carried out in the literature for the case of a pole and a saddle and a branch point in close proximity. More formulae representing the other possible cases can be derived in a similar way, and we do not carry this out because the uniform approximation was not needed for our practical computations.

Again our integral is of the form (to simplify notation)

$$I = \int_{C_s} f(p) e^{\omega\phi(p)}\, dp, \qquad \omega \to \infty. \tag{1.71}$$

where $f(p)$ is defined to have a branch point at $p = p_b$, and a pole at $p = p_L$. The exponent $\phi(p)$ has a saddle point at $p = p_0$ and C_s is the steepest descents contour. We have assumed that $\phi''(p) \neq 0$. The above integral is meant to be one part of the total seismic reflection response, which can be related to previous notation via

$$f(p) = B(p)\sqrt{p_b - p}. \tag{1.72}$$

(The $A(p)$ term can be treated similarly). The idea behind uniform expansions (see Bleistein and Handelsman, 1986), is to make an exact transformation of the exponent (ϕ) to a canonical exponent. The canonical exponent should retain the essential character of the original (in our case it must contain a saddle point).

Thus a natural choice for the transformation is

$$\phi(p) = -t^2/2 - zt + \rho, \tag{1.73}$$

where we have the freedom to define the constants z and ρ (we have already specified the coefficient of the 2^{nd} order term, anticipating relating our results to Parabolic Cylinder Functions). Following Bleistein and Handelsman's choices,

$$\begin{aligned} t = -z \ &\leftrightarrow \ p = p_0 \\ t = 0 \ &\leftrightarrow \ p = p_b. \end{aligned} \tag{1.74}$$

Substitution leads to

$$\rho = \phi(p_b) \qquad z = -\sqrt{2(\phi(p_0) - \phi(p_b))} \tag{1.75}$$

and

$$t = -z - \sqrt{2(\phi(p_0) - \phi(p))}. \tag{1.76}$$

The negative root is taken to make it easier to relate the result to our non-uniform approximations. (The branch cut is taken along the nagative real axis). We want the transform to be conformal in some region D surrounding the saddle point,[12] so that the transformation is a one to one mapping. The condition that the transformation is conformal is that

$$\frac{dt}{dp} = \frac{\phi'(p)}{\sqrt{2(\phi(p_0) - \phi(p))}} \tag{1.77}$$

be finite and non-zero in our region D. That this is actually so can be seen by applying l'Hospital's rule at $p = p_0$:

$$\left.\frac{dt}{dp}\right|_{p=p_0} = \frac{\phi''(p)}{dt/dp} \tag{1.78}$$

which leads to

$$\left.\frac{dt}{dp}\right|_{p=p_0} = -\sqrt{-\phi''(p_0)}. \tag{1.79}$$

---

[12] We also truncate the contour C_s keeping only that part which lies in D, introducing asymptotically small errors.

We can arrive at the same result a different way, and this provides some insight into our formulae. If we expand for small $|p - p_0|$ then

$$\frac{dt}{dp} \approx \frac{-\phi''(p_0)(p - p_0)}{-\sqrt{-\phi''(p_0)(p - p_0)^2}}. \tag{1.80}$$

The above reduces to equation (1.79), if $\forall p$

$$(p - p_0) = \sqrt{(p - p_0)^2}. \tag{1.81}$$

While this may seem a trivial result, it is of consequence from a computational point of view (i.e. actually finding z). For we see that

$$\arg[(p_b - p_0)^2] = \begin{cases} 2\pi & p_b < p_0 \\ 0 & p_b > p_0 \end{cases} \tag{1.82}$$

so that taking the square root we get a difference of sign.[13] Thus for the reflected seismic wave we may equivalently write [14]

$$z = \begin{cases} +e^{i\pi/4}\sqrt{2|\phi(p_0) - \phi(p_b)|} & p_b < p_0 \\ -e^{i\pi/4}\sqrt{2|\phi(p_0) - \phi(p_b)|} & p_b > p_0. \end{cases} \tag{1.83}$$

The above result, which we recognize as the root of the difference between the reflected and head wave travel times, makes sense as it preserves the geometry of our problem (the saddle point now passes through the branch point continuously in one direction in the complex t plane). Although the reflected wave travel time is always greater than the head wave travel time, our parameter z differentiates between the pre- and post-critical zones by a change of sign. All of this followed from the condition that the transformation must be conformal. It is interesting to note that this formula employs the head wave travel time in the pre-critical zone where no head wave actually exists - often we see asymptotic formulae depending upon mathematical constructions, which are analytic continuations of physical quantities into regions where they have no physical meaning.[15] We shall see this again in Chapter 4 when we study diffracted waves.

---

[13] A computer would assume $\arg[(p_b - p_0)^2] = 0$ always.

[14] Since $\arg[\phi(p_0) - \phi(p_b)] = \pi/2 + \arg[(p_b - p_0)^2]$

[15] This phenomenon is not restricted to asymptotics, but rather can be seen throughout mathematics. For example, at the most basic level one may ponder as to the possible meaning of -1 eggs in a basket. This does not, however, detract from the great utility of negative numbers.

Thus we have (if $\tilde{C}_t$ is our truncated, transformed contour)

$$I \sim e^{\omega\rho} \int_{\tilde{C}_t} G(t) e^{-\omega(t^2/2+zt)}\, dt \tag{1.84}$$

where

$$G(t) = f(p) \cdot dp/dt. \tag{1.85}$$

Now $G(t)$ has a branch point at $t = 0$ (or $p = p_b$) and a pole at $t = t_L = -z - \sqrt{2(\phi(p_0) - \phi(p_L))}$ (or $p = p_L$). Thus we can write

$$I \sim e^{\omega\rho} \int_{\tilde{C}_t} \frac{\sqrt{t}}{t - t_L} H(t) e^{-\omega(t^2/2+zt)}\, dt \tag{1.86}$$

and

$$H(t) = f(p) \frac{dp}{dt} \frac{t - t_L}{\sqrt{t}} \tag{1.87}$$

where $H(t)$ is a (locally) smooth function, which we may approximate by Lagrange polynomials that are exact at $p = p_L$, $p = p_0$ and $p = p_b$. The coefficients must be re-arranged, and it turns out that it is equivalent to expanding in the following series:

$$H(t) = h_0 + h_1(t - t_L) + h_2(t - t_L)\,t + J(t) \cdot (t - t_L)(t + z)\,t \tag{1.88}$$

where $J(t)$ is another smooth function. The coefficients are

$$\begin{aligned} h_0 = H(t = t_L) \qquad h_1 &= \frac{H(t + 0) - H(t = t_L)}{t_L} \\ h_2 = \frac{H(t = -z) - H(t = t_L)}{z(z + t_L)} &+ \frac{H(t = 0) - H(t = t_L)}{t_L(z + t_L)}. \end{aligned} \tag{1.89}$$

Our result stands at

$$\begin{aligned} e^{-\omega\rho} I \sim h_0 \int_{\tilde{C}_t} \frac{\sqrt{t}}{t - t_L} e^{-\omega(t^2/2+zt)}\, dt + h_1 \int_{\tilde{C}_t} \sqrt{t} e^{-\omega(t^2/2+zt)}\, dt \\ + h_2 \int_{\tilde{C}_t} t^{3/2} e^{-\omega(t^2/2+zt)}\, dt + \int_{\tilde{C}_t} t^{3/2}(t + z) J(t) e^{-\omega(t^2/2+zt)}\, dt. \end{aligned} \tag{1.90}$$

At this point we extend the truncated and transformed contour to ±∞, again only introducing asymptotically small errors. If we integrate by parts the last term we get

$$\frac{1}{\omega}\int_{C_t}\left((3/2)\sqrt{t}J + t^{3/2}\frac{dJ}{dt}\right)e^{-\omega(t^2/2+zt)}\,dt \tag{1.91}$$

which, if J is smooth, is asymptotically negligible when compared to the three previous terms. One might worry about the existence of dJ/dt at $p = p_0$ (and hence the smoothness in this vicinity) in view of that part of J found in equation (1.77). However it can be shown that

$$\left.\frac{d^2p}{dt^2}\right|_{p=p_0} = \frac{1}{\sqrt{-\phi''(p_0)}} \tag{1.92}$$

remembering that we assume $\phi''(p_0) \neq 0$. We see that the last term in equation (1.90) has a form similar to the original integral in equation (1.86) being studied, in the sense that the integrand contains the product of a smooth function and a function that cannot be approximated. Thus the above approximation process can be continued, generating an asymptotic series, the dominant three terms of which are given in equation (1.90). We can now relate the above integrals to special functions, once the direction of the transformed contour has been nailed down. Part of the steepest descents contour in the complex p plane can be parameterized local to the saddle point as (where we are considering direction)

$$p = p_0 + se^{-i\pi/4}, \qquad s \in \Re^+ \tag{1.93}$$

so that

$$2(\phi(p_0) - \phi(p)) \approx -\phi''(p_0)s^2 \tag{1.94}$$

and since $\arg[\phi''(p_0)] = -\pi/2$ we have

$$t \approx -z - s \tag{1.95}$$

near the saddle point. Thus for pre-critical angles our contour extends from $+\infty$ to $-\infty$ above the branch point at $t = 0$. This is enough to discern the following relationships:

$$\begin{aligned}\int_{C_t} \frac{\sqrt{t}}{t-t_L} e^{-t^2/2-\sqrt{\omega}zt}\,dt &= \sqrt{2\pi}\mathcal{F}(\sqrt{\omega}z, \sqrt{\omega}t_L)\\ \int_{C_t} \sqrt{t}e^{-t^2/2-\sqrt{\omega}zt}\,dt &= -\sqrt{2\pi}e^{i\pi/4+\omega z^2/4}D_{1/2}(i\sqrt{\omega}z)\\ \int_{C_t} t^{3/2}e^{-t^2/2-\sqrt{\omega}zt}\,dt &= -\sqrt{2\pi}e^{i3\pi/4+\omega z^2/4}D_{3/2}(i\sqrt{\omega}z).\end{aligned} \tag{1.96}$$

If we redefine z to include the $\sqrt{\omega}$ factor and let $w = \sqrt{\omega}t_L$ then we arrive at the result

$$I \sim \sqrt{2\pi}e^{\omega\phi(p_b)}\left\{\frac{h_0}{\omega^{1/4}}\mathcal{F}(z,w) - \frac{h_1}{\omega^{3/4}}e^{i\pi/4+z^2/4}D_{1/2}(iz) - \frac{h_2}{\omega^{5/4}}e^{i3\pi/4+z^2/4}D_{3/2}(iz)\right\}. \tag{1.97}$$

This bears a strong resemblance to the corresponding portion of the non-uniform formula for Case 1 derived previously. However, a great part of this similarity is notational, since the underlying variables z and w and the coefficients h_0, h_1 and h_2 have a much more complicated form than did the originals. We shall now explore the connection between the uniform and the non-uniform results.

The variables may be approximated for small $|p_0 - p_b|$ and small $|p_0 - p_L|$ to give

$$\begin{aligned} z &\approx \sqrt{\omega}\sqrt{-\phi''(p_0)}\,(p_0 - p_b)\\ w &\approx \sqrt{\omega}\sqrt{-\phi''(p_0)}\,(p_b - p_L)\end{aligned} \tag{1.98}$$

which are exactly the ones found using a non-uniform formula. The coefficients are fairly complicated, and so we only look at the example of h_0:

$$h_0 = \lim_{t\to t_L \text{ or } p\to p_L}\left\{f(p)\frac{dp}{dt}\frac{t-t_L}{\sqrt{t}}\right\}. \tag{1.99}$$

If we assume $|p_L - p_0|$ is small, and remembering that in the seismic problem $f(p) = \sqrt{p_b - p}B(p)$, then we can find

$$h_0 = \frac{p_L - p_0}{\phi'(p_L)}[-\phi''(p_0)]^{3/4} \cdot \lim_{p\to p_L}(p_L - p)B(p) \tag{1.100}$$

which is not yet recognizable, and has a removable singularity to boot. We do point out that

$$\lim_{p\to p_L}(p_L - p)B(p) = -Res_{p=p_L}B(p) = -b_0 \tag{1.101}$$

where b_0 was originally defined back in equation (1.34) Also, in our previous notation

$$-\phi''(p_0) = i\rho^2. \tag{1.102}$$

If we evaluate this using dp/dt at $p = p_0$ (assuming it varies slowly), we get

$$h_0 = b_0 e^{-i\pi/8} / \sqrt{\rho} \tag{1.103}$$

Putting this into the original reflected wave integral we find

$$I \sim \frac{\alpha_1 b_0 \omega^{1/4} e^{i\pi/8}}{\sqrt{r\rho}} \mathcal{F}(z, w) \tag{1.104}$$

which is exactly the contribution found in the non-uniform expansion (see equation (1.48)). A similar simplification can be carried out for all the coefficients in equation (1.97) (and for other integrals making up the uniform approximation to the reflected wave, if we derived them). In summary, the non-uniform expansion is the uniform expansion simplified for small $|p_0 - p_L|$ and $|p_0 - p_b|$.[16] Since we shall see that the non-uniform expansion in conjunction with regular asymptotic expressions is capable of modelling the reflected wave properly, the added complexity of the uniform expansion makes it of theoretical interest only.

1.6 Method of Červený and Ravindra

Červený and Ravindra (1971) derived a non-uniform asymptotic expansion in the vicinity of the critical angle of a reflected wave. Their result is not generally applicable because they failed to account for the leaky pole singularities. Rather than dismissing this outright, we shall examine some of the aspects of the derivation, which has the unique property of being valid for near grazing angles (recall that generally non-uniform expansions are not valid at grazing angles, due to the presence of a branch point in the exponent). This is achieved through a combination of exact transformation of the exponent, and local approximation.

---

[16] Since p is not dimensionless, it would be more accurate to say $|\alpha_1 p_0 - \alpha_1 p_L| \ll 1$ and $|\alpha_1 p_0 - \alpha_1 p_b| \ll 1$.

The vertical component of the displacement of the reflected P-wave has been given as

$$u_z \sim \alpha_1 e^{-i\omega t+i\pi/4}\sqrt{\frac{\omega}{2\pi r}}\int_{C_s} R(p)e^{\omega\phi(p)}\,dp, \tag{1.105}$$

where we are looking at the reflection from a single interface. C&R then change from the steepest descents contour, C_s, to a new one which provides a convenient parameterization of the terms in the exponent. This new contour, Ω, must coincide with C_s in the vicinity of the saddle point. One can still make steepest descents approximations provided that the contour still lies on a path of descent (although not the steepest). The two contours, C_s and Ω are considered asymptotically equivalent, meaning that the asymptotic expansions using either contour differ by, at most, an exponentially small amount. The contour chosen by C&R is given by

$$\sqrt{1/\alpha_1^2-p^2}=\sqrt{1/\alpha_1^2-p_0^2}+xe^{-i\pi/4}, \qquad x\in\Re. \tag{1.106}$$

We have not used p_b to represent the branch point, as this referred to one of several possible branch points in $R(p)$; here the radical we are considering is also in the exponent and the branch point represents grazing angles (for the P-wave case $p_0 = 1/\alpha_1$). Clearly for the new contour $x = 0 \Leftrightarrow p = p_0$, and

$$\left.\frac{dp}{dx}\right|_{x=0} = -e^{-i\pi/4}\frac{\sqrt{1/\alpha_1^2-p_0^2}}{p_0^2}, \tag{1.107}$$

so that the contour runs parallel to the steepest descents contour near the saddle point. Figure 1.9 shows a comparison of the contours in the complex ray parameter plane for an angle of incidence of 37°. Also shown is the path along which $Re\{\phi\} = 0$, which is the path of neutral ascent. For the transformation of C& R to be valid, the transformed contour must lie between the steepest descents contour and the path of neutral ascent. The transformation makes the exponent

$$\tilde{\phi}(x) = ir\sqrt{p_0^2+ix^2-2xe^{-i\pi/4}\sqrt{1/\alpha_1^2-p_0^2}} \;+\; i(h_1+z)\left(xe^{-i\pi/4}+\sqrt{1/\alpha_1^2-p_0^2}\right). \tag{1.108}$$

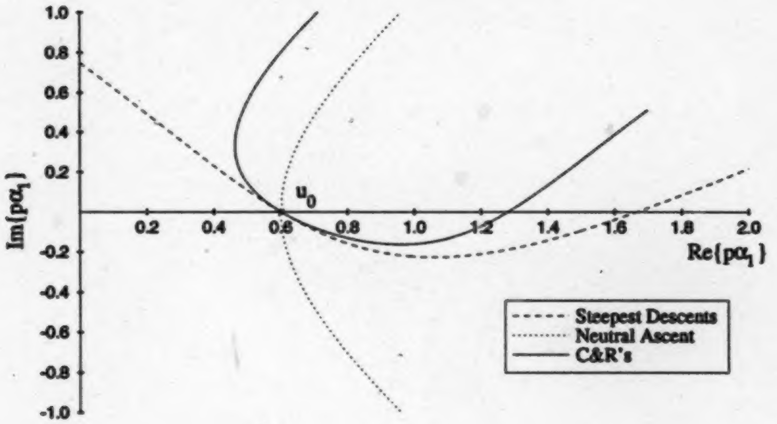

Figure 1.9: The descent contour of Červený and Ravindra near the saddle point. The boundary of descent (line of neutral ascents) is also shown for comparison. The saddle is at $p\alpha_1 = u_0 = \alpha_1 p_0$, and grazing incidence is at $p\alpha_1 = 1$.

This has a more complicated form than $\phi(p)$, but we can now approximate it by

$$\tilde{\phi}(x) \approx \tilde{\phi}(0) + 1/2\tilde{\phi}''(0)x^2 \tag{1.109}$$

which doesn't lose accuracy for $p_0 \to 1/\alpha_1$, in contrast to approximating $\phi(p)$ by its two term Taylor expansion.[17] Thus, this method is particularly suited for studying waves near grazing angles (for small contrasts in velocity across the interface, the critical points approach grazing rays, i.e. $1/\alpha_2 \to 1/\alpha_1$). It combines elements of uniform expansions with non-uniform expansions. The rest of the derivation is fairly pedestrian and can be found in the book by C&R, so we do not repeat it here.

A limitation of this method is that it applies *in its present form* only for restricted angles of incidence. This can be seen by examining the behaviour of the contour far from the saddle point. We have for large $|p|$

---

[17] Note that the transformed exponent has a saddle point, preserving the essential character of the original exponent.

$$\frac{dp}{dx} \approx e^{i\pi/4} \tag{1.110}$$

so that the contour makes an angle $\arctan(1) = 45°$ to the real axis. The path of neutral ascents can be parameterized as follows:

$$Re\{\phi\} = 0 \tag{1.111}$$

$$\text{so} \tag{1.112}$$

$$\frac{p_0 p}{\sqrt{1/\alpha_1^2 - p_0^2}} + \sqrt{1/\alpha_1^2 - p^2} = x^2, \qquad x \in \Re \tag{1.113}$$

where we have omitted the constant factor of $(h_1 + z)$. For large $|x|$ we can find that

$$\frac{dp}{dx} \approx 2x\left(p_0\sqrt{1/\alpha_1^2 - p_0^2} + i(1/\alpha_1^2 - p_0^2)\right) \tag{1.114}$$

which forms an angle of $\arctan(\frac{\sqrt{1/\alpha_1^2 - p_0^2}}{p_0})$ with the real axis. The condition that Ω follows a path of descent the comes down to

$$\frac{\sqrt{1/\alpha_1^2 - p_0^2}}{p_0} < 1 \tag{1.115}$$

or, $\theta > 45°$, where θ is the angle of incidence. Thus for an angle of incidence of 45° the contour for this method ascends, and so the method of steepest descents doesn't apply. This is a drawback of the method, and is one reason why we originally opted for using purely non-uniform derivations. The drawback is actually not as serious as it seems, since for all angles of incidence the contour is in a region of descent near the saddle point, and can be truncated introducing only negligible errors (much as we did when deriving the uniform expansions). The portion retained is all descents, and can then be re-extended to $\pm\infty$, again introducing only negligible errors. Of course, only the first term in the expansion is of use after such a procedure.

1.7 Chapter Summary

We have described the exact closed form solutions for a wave reflected from a plane interface separating homogeneous, isotropic media, and shown how it may be extended when considering a wave following a particular raypath in a homogeneous, isotropic system of layers. To avoid computing these integrals exactly (using some numerical technique) we have employed the method of steepest descents. Near critical angles the regular steepest descents approximation (which coincides with ART) is no longer valid; we have proceeded to use a modification of the steepest descents method to arrive at several non-uniform approximations to be used in conjunction with ART. These formulae are non-uniform in the sense that they are only valid for a particular range of offsets and frequencies, precisely in the regions where regular ART fails (boundary layers). In the next chapter we shall evaluate our approximation through comparison with numerical integration of the integrals representing the exact reflected waves.

For comparison, we have also looked at the uniform approximations of Bleistein and Handelsman (1986), which are valid at all frequencies and offsets. The uniform formulae had a rather complicated form which is masked by the simple notation. We shall see in Chapter 2 that the non-uniform formulae provide an adequate solution, making the uniform approximations of theoretical interest only. Briefly we summarized the technique of Červený and Ravindra, which contained an interesting combination of uniform and non-uniform formulae.

Chapter 2

Numerical Results

2.1 Introduction

We have derived asymptotic approximations for seismic waves, and would now like to test the results. We shall compare the amplitudes from our derivations with a numerically derived solution both in the time and frequency domains (we look at harmonic incident waves). A specific geology is chosen to base the comparison upon, which brings out the different interference phenomena that we are trying to model. We also take a limited look at the location of leaky poles in the complex ray parameter plane, as this has (to the best of our knowledge) only been carried out by Chapman (1972) for Lamb's Problem (i.e. a free surface).

2.2 Location of Poles

It is useful to gain a qualitative idea of the movement of the leaky poles for various geologic models, so we can gauge which types of media have important leaky wave considerations. In Chapter 1 we saw that from a strict high frequency asymptotic point of view, leaky waves are negligible unless they interfere with a body phase. Thus their importance is measured by the distance of the pole to the closest branch point or saddle point in the complex ray parameter plane (keeping in mind that this is only true for post-critical angles, so this is valid when the saddle point is to the right of the branch point). We also point out that the closer the pole is to the real axis (to the left of the particular branch point representing grazing rays), the smaller $|Re\{\phi(p_L)\}|$ in equation (1.14), and hence the less attenuated the pulse. The location of leaky poles in the complex ray parameter plane is a function of the material properties of the two media, $\alpha_1, \alpha_2, \beta_1, \beta_2$, and ρ_1/ρ_2.[1] If we introduce a dimensionless variable pv, where v is one of the four wave velocities, then the poles vary only as functions of $\alpha_1/\alpha_2, \sigma_1, \sigma_2$, and ρ_1/ρ_2, where σ is Poisson's ratio. The velocity v can be chosen to normalize the pole location relative to the branch point of interest. Since the distance from the saddle point and branch point to the leaky pole approximately determines the magnitude of the leaky pulse, this choice of normalization allows us to quickly assess the relative importance of pole locations from a diagram where velocities are not fixed. We need to narrow the field of enquiry, as there are many possible pole locations. There is a possible leaky pole associated with each type of head wave, of which there are 26. This depends upon which phase we are looking at (P and/or S), whether we have upgoing or downgoing waves, and the different velocity distributions. Ultimately one would like a map of all poles on all eight Riemann sheets for all possible velocity combinations. This would fill volumes, and so we restrict ourselves to one of the more common situations. We shall look for the poles that affect the upgoing reflected P-wave, when the P-wave velocity in the lower medium is greater than or equal to the P-wave velocity in the upper medium. (Reasonable since velocity generally increases with depth). The reflected wave in this situation is influenced by the head wave associated with the transmitted P-wave (branch point is at $p = 1/\alpha_2$, and the code is 131 according to C& R) and the head wave associated with the transmitted (and converted) S-wave (branch point at $p = 1/\beta_2$, and code 141 according to C& R). For poles near $p = 1/\alpha_2$ we must look on the sheet $(- + ++)$, both above and below the real axis, as was shown in Chapter

---

[1] See equation (1.12).

1. When we look for poles near the branch point $1/\beta_2$, we need to search the sheet $(--++)$ above the real axis, and $(+-++)$ below the real axis. The reason why this is so is shown in Figure 2.1, where we see that any poles on the $(--++)$ sheet below the real axis are much farther away (in terms of a continuous Riemann sheet) from $p = 1/\beta_2$ than poles on the $(+-++)$ sheet. Even so, we found that poles on the $(+-++)$ sheet to be generally far away

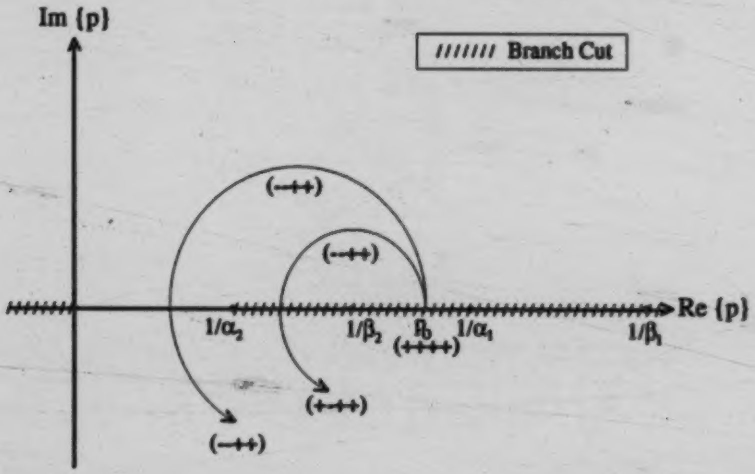

Figure 2.1: A description of the distance from the saddle point to poles on the different Riemann sheets.

from $1/\beta_2$ for the models studied, and so do not investigate them further. In the following, we map out only the poles that are close to the branch point in question, even though more leaky poles are present.[2] Due to the above mentioned normalization arguments, we use the complex $p\alpha_2$ plane, when mapping the leaky poles from the $(-+++)$ sheet, and the $p\beta_2$ plane, when mapping the leaky poles on the $(--++)$ sheet. Pole locations are shown only for the 1^{st} quadrant, keeping in mind that corresponding complex conjugate poles are to be found in the 4^{th} quadrant. The latter poles' existence follows from the fact that $R(p)$ coincidentally obeys the 'reflection principle' on a given Riemann sheet, from the theory of complex variables. The poles have not been represented when they lie on the real axis, where they are generally isolated. In Figures 2.2 and 2.4 we have contoured pole locations by varying $n = \alpha_1/\alpha_2$ and σ_1, while holding $\sigma_2 = .315$ constant at a value typical for limestones. The density ratio is not held constant, but varies according to $\rho_j = 0.31\alpha_j^{1/4}$ (Sheriff and Geldart, 1983). (The actual values plotted had ρ_2 very slightly deviate from this relationship). In this way we can change n to model varying velocity contrasts, and σ_1 to reflect different top media lithologies, while keeping the densities at realistic values. Figures 2.3 and 2.5 map the pole locations as a function of n and σ_2, while keeping $\sigma_1 = .25$ constant.

---

[2] How many poles are there in total? This is a tough one, since it would involve expanding D in equation (1.12) into a polynomial and then observing what order polynomial we are left with. The algebra would be immensely tedious for such a marginally useful result. One can obtain an upper bound by recognizing how many times the expression $D = 0$ would need to be squared to get rid of the square-root terms. This gives us an upper bound of 48 poles, but is likely considerably less. For the simple case of Lamb's problem where $\alpha_1 = \beta_1 = 0$, one can use the above method of estimating to give a maximum of 8 poles, and doing the algebra results in actually only a 6^{th} order polynomial (due to some cancellation).

Both Figures 2.2 and 2.3 show that the poles move closer to the branch point $p = 1/\alpha_2$ for lower n. Therefore, the need for Cases 1, 3 and 4 arises from a combination of small $|\omega\phi''(p_0)|$ and large velocity contrast across the interface. This is in agreement with the observations of C&R, who found that their formulae (Case 2) were not applicable for strong contrasts in velocity, and recommended its use only for $.75 \leq n \leq .95$. Changing Poisson's ratio tends to rotate the poles about the branch points. Increasing σ_1 moves the poles to the left of the branch cut, while the opposite holds true for changes in σ_2. Thus for low σ_1[3] (high σ_2[4]) it is more likely that a residue will need to be evaluated, whereas for high σ_1 (low σ_2) the pole will likely avoid the steepest descents contour. However, as we shall see, poles that do not require a residue may still have a significant influence upon the reflected wave. Figure 2.4 is not quite a contour map, since the pole locations

---

[3] 'harder rocks'

[4] 'softer rocks'

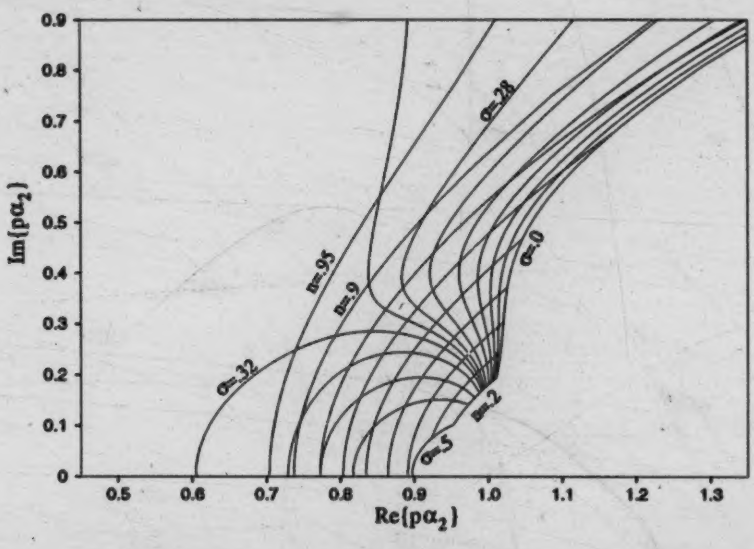

Figure 2.2: The locations of poles on the $(- + ++)$ sheet plotted as a function of $n = \alpha_1/\alpha_2$ and σ, the latter being Poisson's ratio in the upper medium. The contour interval for n is .1, unless otherwise labelled. The contour interval for σ is .05, unless otherwise labelled. The branch point is located at $p\alpha_2 = 1$.

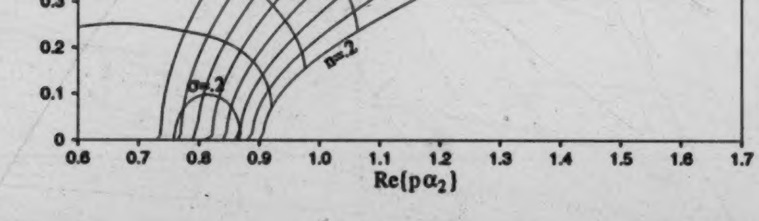

Figure 2.3: The locations of poles on the $(- + ++)$ sheet plotted as a function of $n = \alpha_1/\alpha_2$ and σ, the latter being Poisson's ratio in the lower medium. Other parameter values are described in the text. The contour intervals for n and σ is .1 and .05, respectively.

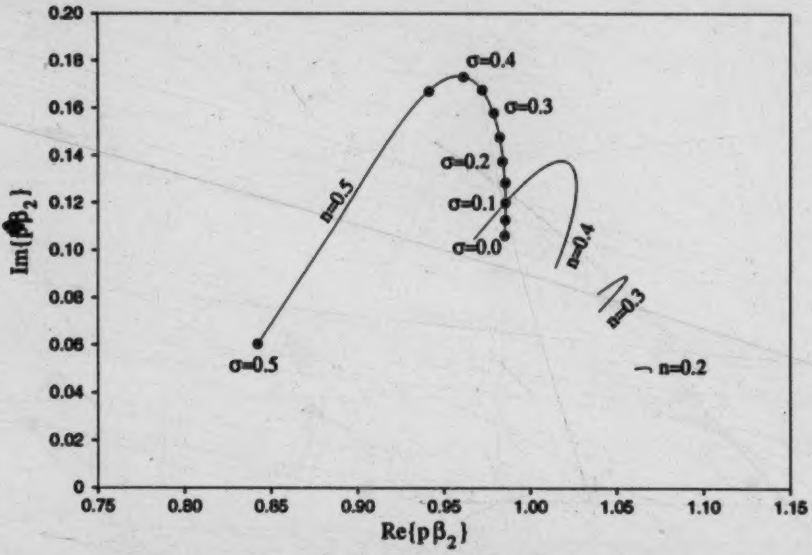

Figure 2.4: Here we plot poles on the $(--++)$ sheet as a function of $n = \alpha_1/\alpha_2$ and σ (upper medium). A contour map is not possible, so representative poles are plotted and labelled. The branch point is located at $p\beta_2 = 1$

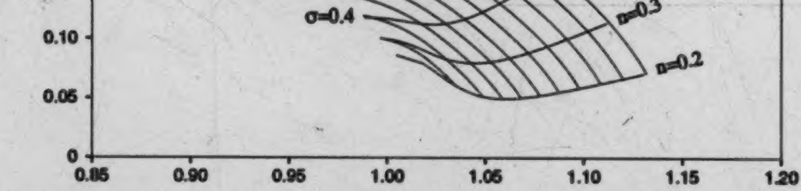

Figure 2.5: Again we plot poles on the $(--++)$ sheet, this time varying $n = \alpha_1/\alpha_2$ and σ (lower medium).

are not single valued functions of n and σ_1 (contour would cross). Thus we have just plotted curves of poles for varying n, and on $n = .5$ we have placed dots which represent the different values of σ_1. We cannot plot all values of n and σ_1 and σ_2; we need the branch point $1/\beta_2$ to lie to the left of $1/\alpha_1$ (the grazing ray for our reflected P-wave), for the poles to have any significance. Both Figures 2.4 and 2.5 show that the poles move in a clockwise rotation about $p = 1/\beta_2$ as n gets smaller. It would also appear that extreme values of σ_1 (high or low) and high values of σ_2 lead to the most prominent leaky pole effects.

2.3 Harmonic Wave Amplitude Curves

We apply our results to a system of homogeneous layers, taking the parameters from Ogilvie and Purnell (1996). This model is particularly suitable as it consists of a salt bed beneath layers of sediment, providing both high and low velocity contrasts across interfaces. Table 1 summarizes the salt model. We assume the source presented in Chapter 1, and only model primary P-wave reflections. The receivers are located in the first medium, and the free surface effects are ignored. We calculate amplitude vs. offset curves, and compare the results from using a patchwork of non-uniform approximations (see Chapter 1) to a numerical integration, for a 20Hz incident wave. The numerical integration is carried out using an integrand similar to equation (1.10), but for pressure, since the first medium is water. We integrate along a complex contour in the ray-parameter plane[5], and do not include contours which represent the inhomogeneous head wave and regular interface wave contributions.

The contrast in velocities across the first interface is not great, which suggests that the leaky poles are not important for an asymptotic description of the reflected wave. Figure 2.6 shows the amplitude calculated by zero order ART, which is sharply peaked about the critical offset. For the most part, only Case 2 is needed

---

[5] See Chapter 3 for details.

Table 2.1: Salt Model Parameters

Material	α (m/s)	β (m/s)	ρ (g/cc)	thickness (m)
water	1500	0	1.01	1036
sediment	2040	772	2.05	464
sediment	2106	850	2.10	542
salt	4481	2530	2.14	884

according to the boundary layers described earlier, and the result is plotted in Figure 2.7. The oscillatory nature of the curves arises from the interference between the reflected and head waves for post critical angles, keeping in mind the source is monochromatic. We see a slight jump in amplitude at the edge of the Case 2 boundary layer, and this is a result of using a non-uniform expansion. That is, as the saddle point moves away from the branch point, amplitude discrepancies increase, and are a maximum at the edge of the boundary layer. This accumulation of error is then abruptly corrected as we pass back into

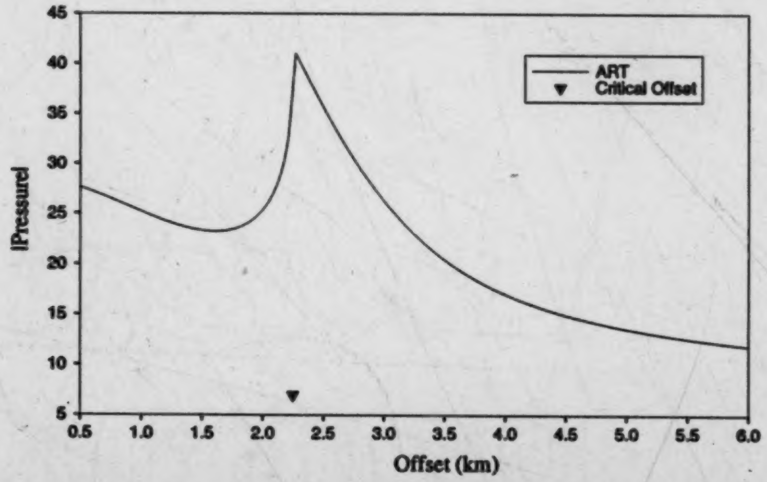

Figure 2.6: The zero-order ART approximation to the reflected P-wave from the first interface. The triangle marks the critical offset, corresponding to the angle at which the transmitted P-wave is critically refracted. These conventions are adhered to in Figures 2.7 through 2.12.

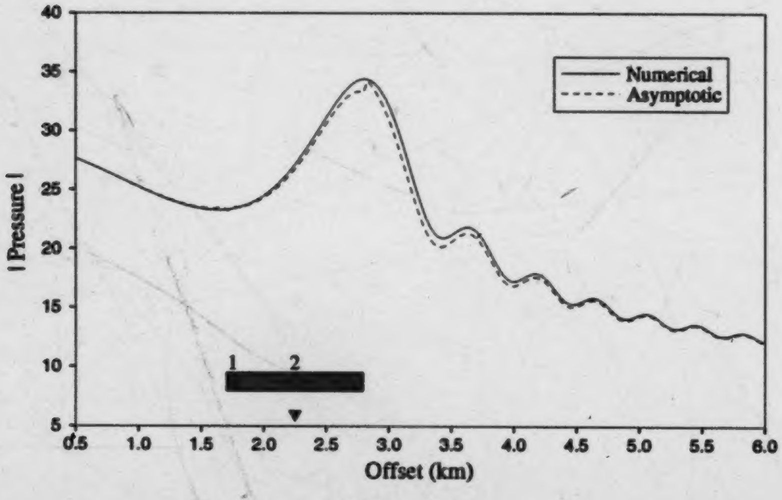

Figure 2.7: Comparison of numerical and asymptotic results for the P-wave reflection from the bottom of layer 1. The range over which the case formulae are used is shaded. Where no labels (or shades) exist, regular leading order asymptotic expressions are used, except for post-critical angles where first order head wave terms are included.

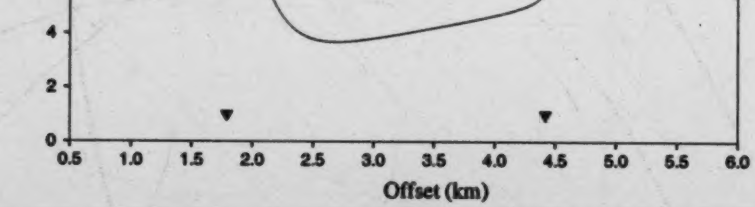

Figure 2.8: The zero order ART approximation to the reflected P-wave from the third interface. Note the second critical offset, corresponding to the angle at which the transmitted (and converted) S-wave is critically refracted.

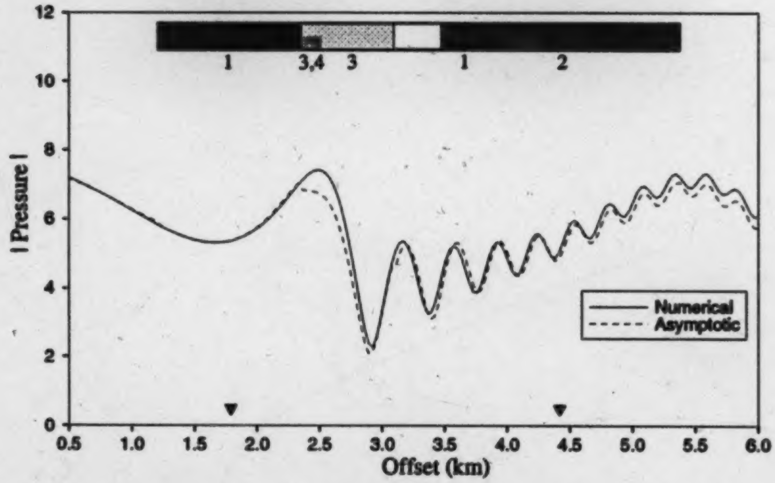

Figure 2.9: Comparison of numerical and asymptotic results for the P-wave reflection from the bottom of layer 3.

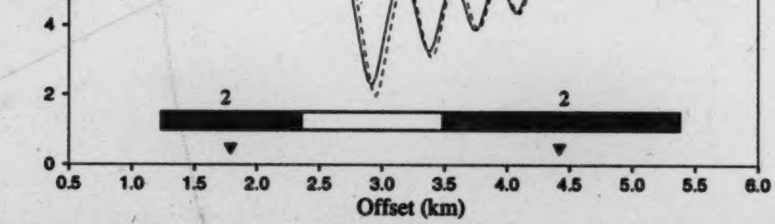

Figure 2.10: Comparison of numerical and asymptotic results for the P-wave reflection from the base of layer 3. Here the asymptotic label implies the use of the Case 2 formula only, in conjunction with regular asymptotic expressions.

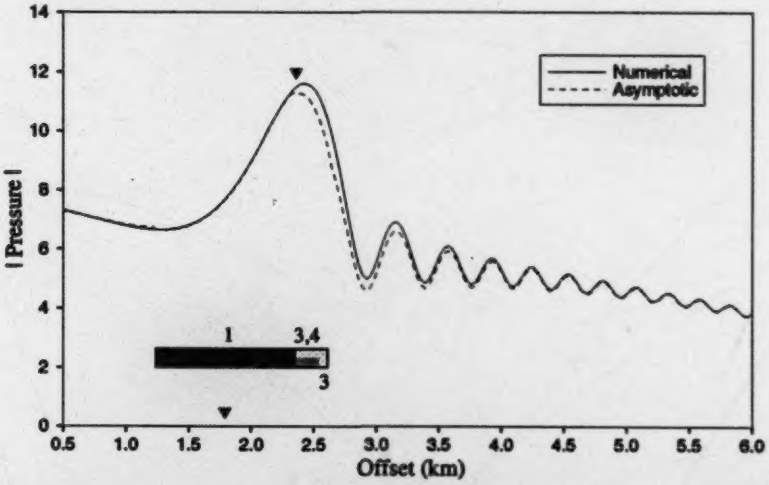

Figure 2.11: Comparison of numerical and asymptotic results for the P-wave reflection from the bottom of layer 3. In this instance Poisson's ratio in layer 4 has been adjusted to $\sigma = .35$. The upper triangle refers to the offset at which a residue from a pole on the sheet $(- + ++)$ first need be included (it is included for all subsequent offsets as well).

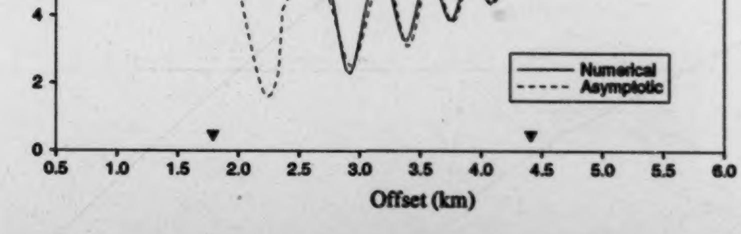

Figure 2.12: Comparison of numerical and asymptotic results for the P-wave reflection from the bottom of layer 3. Here the asymptotic label implies the use of all case formulae where needed, except that poles with a negative imaginary part are neglected.

using the regular asymptotic formulae. The contrast in velocities across the third interface is large, and one expects the leaky pole influence to be greater. The zero order ART amplitude curve is shown in Figure 2.8, where now two critical offsets exist. Figure 2.9 compares the results for this interface, and shows where each case formula has been used. The match is imperfect at offsets of 2.4-2.6 km. This is actually where we pass from Case 1 to Cases 3 and 4. A better match can be found by extending the boundary between Case 1 and Cases 3 and 4 to $|z| = 3$, for post-critical reflection. Poisson's ratio for layers 3 and 4 is .40 and .266 respectively. This is high in layer 3, and as a consequence the leaky poles are situated to the left of the steepest descents contours, so no residues are evaluated in the asymptotic calculation of the wave amplitudes. Yet we see they have a significant influence when we compare Figures 2.9 and 2.10, the latter using only Case 2 to find amplitudes. If a branch point were the only dominant point influencing the saddle, then Case 2 would suffice. It is easy to see that within the Case 1 region, Case 2 provides completely inaccurate results, while in the region where Cases 3 and 4 apply, we see that regular asymptotic expansions (Figure 2.8) are also not adequate. In order to provide an example where a residue needs to be evaluated, we change the model by increasing the value of Poisson's ratio in the fourth layer to .35. Figure 2.11 shows the numerical and asymptotic results, and indicates at what offset a residue is first needed from the $(-+++)$ sheet. We see a good agreement, although it decreases somewhat again in the transition from Cases 1 to 3 and 4. The transition seems to occur where the residue is first taken, although this is merely coincidental; one can show this for higher frequencies, where the boundaries (since they are frequency dependent) shift inwards and the residue location remains the same. In Figure 2.12 we look at the effect of omitting poles below the real axis on the $(-+++)$ and $(--++)$ sheets, hypothesizing that they might have a marginal influence, especially after adjusting the original model (poles have moved more to the right in the complex ray parameter plane). We see that this has no effect near the second critical offset, while it invokes a significant change near the first critical offset. The former is no surprise, for the pole below the real axis on the $(--++)$ sheet is separated from the steepest descents contour by the branch cut originating at $p = 1/\alpha_2$, and is therefore distant in terms of a continuous Riemann surface. In contrast, the pole below the real axis on the sheet $(-+++)$ is relatively close to the steepest descents contour (see Figures 2.1 and 1.3).

2.4 Seismograms

We have shown that our Case formulae are asymptotic solutions applicable at high frequencies. For the case of a 20Hz monochromatic wave, they have been shown to be reasonably accurate representations of the reflected wave. However, it is not entirely clear that the results will be applicable to a seismic pulse, which is composed of a continuous spectrum of frequencies. Thus we construct a pulse that is the first derivative of a Gaussian, namely,

$$f(t) = 2\zeta t e^{-\zeta t^2} \tag{2.1}$$

where the parameter ζ can be chosen such that the spectrum of the pulse has a specified peak frequency ($\omega_{peak} = \sqrt{2\zeta}$). This pulse has no energy at $\omega = 0$, which is a characteristic of seismic waves in general. The reflection seismograms appear phase shifted because the source is formulated in terms of displacement (as defined in Chapter 1), but we measure pressure in the top medium (they are $\pi/2$ out of phase). We start out by looking at a pulse whose peak frequency is at 20Hz. In Figure 2.13 we see the reflected P-wave as computed by zero order ART (this implies that the head wave is omitted). The seismograms have been shifted in time by the difference in the reflected wave travel times between a given offset and the nearest offset. This makes the reflected wave appear to arrive at the same time, which allows us to more clearly observe the phase and amplitude changes from trace to trace. One can view this as using a reduced time $t-\tau_j+\tau_1$ on the vertical axis, where τ_j is the arrival time of the reflected wave at the j^{th} offset. A phase change in the reflected wave is readily visible across the critical offset. Figure 2.14 shows the exact response, which includes a head wave. Due to the time shifting, the head wave emerges from the reflected wave with a non-linear arrival time vs. offset. No leaky pulse is present, due to the pole location for this interface. We see from Figure 2.16 the difference between the exact and ART seismograms is concentrated about the critical offset, and of course must include the head wave. Figure 2.15 contains the seismograms computed using the non-uniform asymptotic formulae of Chapter 1, and Figure 2.17 shows the error in the result. As expected, the error is much smaller than for the ART seismograms, as was seen in our harmonic analysis. We also compute seismograms for the reflected wave from the third interface, with the model adjusted so that a residue is evaluated (i.e. Poisson's ratio is increased to .35 in the fourth layer). This way we can compute a leaky pulse in the time domain to confirm its properties. Figure 2.18 shows the ART reflection for the modified third interface. Seismograms have been scaled by a constant factor for plotting, so the absolute amplitude cannot be compared to the reflection from the first interface. However, we still see the large amplitude buildup near the critical offset, which is decreased somewhat in the exact seismograms (Figure 2.19). The latter contain only one set of head waves since changing the Poisson ratio in the fourth medium moved the second critical point to much larger offsets. The case formulae perform well, and the result is shown in Figure 2.20, and the error is plotted in Figure 2.22. For comparison, we compute the error in the ART seismograms (Figure 2.21), which in this case is quite large. We also see some significant error at the smallest offset trace in Figures 2.22 and 2.21, but this is actually due to our 'exact' seismograms being computed with the far offset approximation and so are slightly in error for near offsets (see Chapter 1 for more details). Figure 2.23 shows the isolated leaky pulse from the third interface, arising from a residue contribution. The pulse is displayed at a magnification of 20× the reflected wave's scale, as it would otherwise be too small to be seen. This supports our analysis in Chapter 1, which suggested that acting alone the leaky pulse is an asymptotically negligible arrival. However, we have witnessed the large change in amplitudes brought about by the presence of a leaky pole, leading us to the conclusion that the leaky pulse nevertheless does have a pronounced influence which cannot be quantified through a simple linear superposition of time domain arrivals, near the critical offset where phases interfere. We see that the leaky pulse rapidly decreases in amplitude with increasing offset, as we previously surmised. The pulse is also low frequency (compare with the reflected wave in Figure 2.19), arrives roughly between the reflected and head waves, and is entirely absent at pre-critical offsets. Overall, we can say that the non-uniform formulae provide a good match with exact seismograms for the pulse whose dominant frequency is 20 Hz.

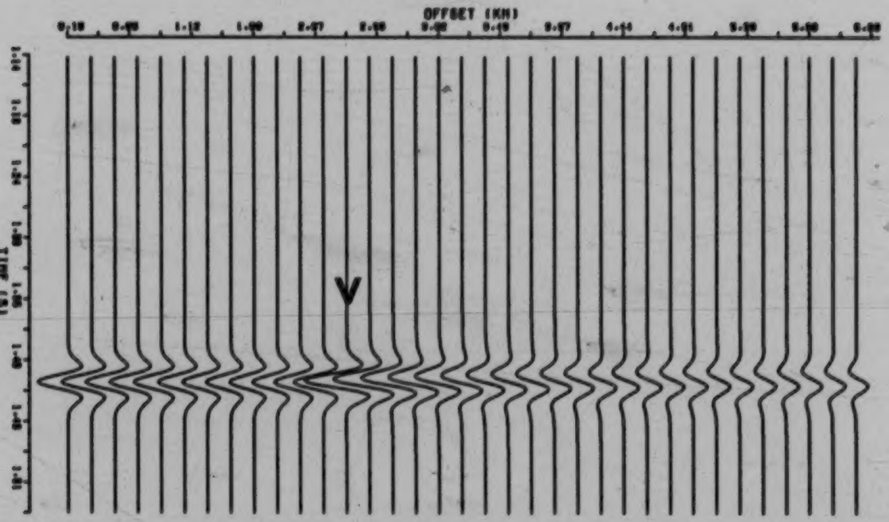

Figure 2.13: Zero order ART approximation to the reflected wave from the first interface. The seismogram at each offset has been time shifted so that the reflection arrives at the same time as the smallest offset arrival. Thus the vertical axis is the reduced time $t - \tau_j + \tau_1$, where τ_j is the travel time of the reflected wave at the j^{th} offset. The critical offset is marked by an arrow. This convention is used for all following seismograms.

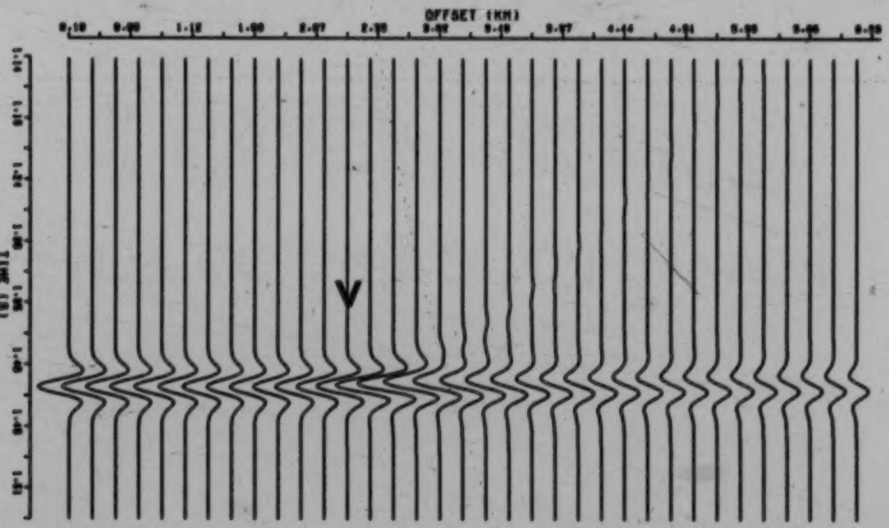

Figure 2.14: The exact reflected P-wave from the first interface, as found by numerical integration. Note the faint head wave which intersects the reflected wave at about 3km offset.

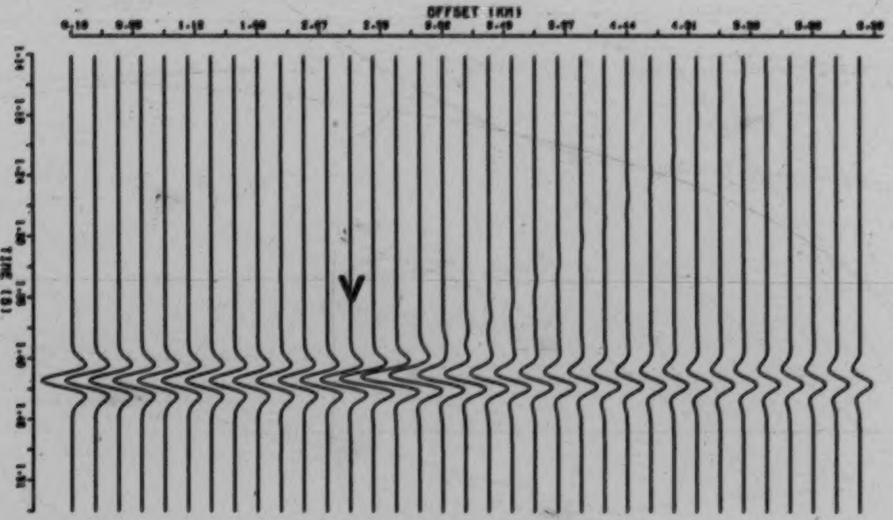

Figure 2.15: The reflected P-wave from the first interface as calculated by the non-uniform asymptotic formulae derived in Chapter 1.

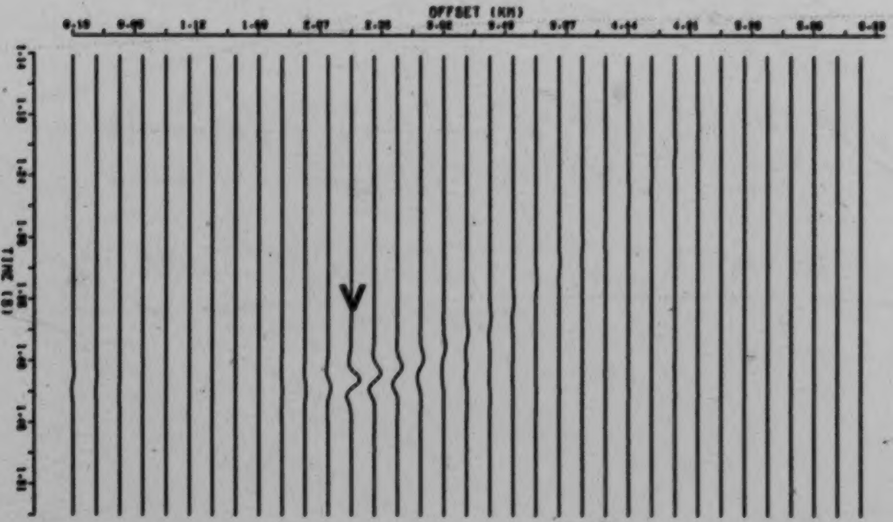

Figure 2.16: The difference between the exact and zero order ART reflections from the first interface.

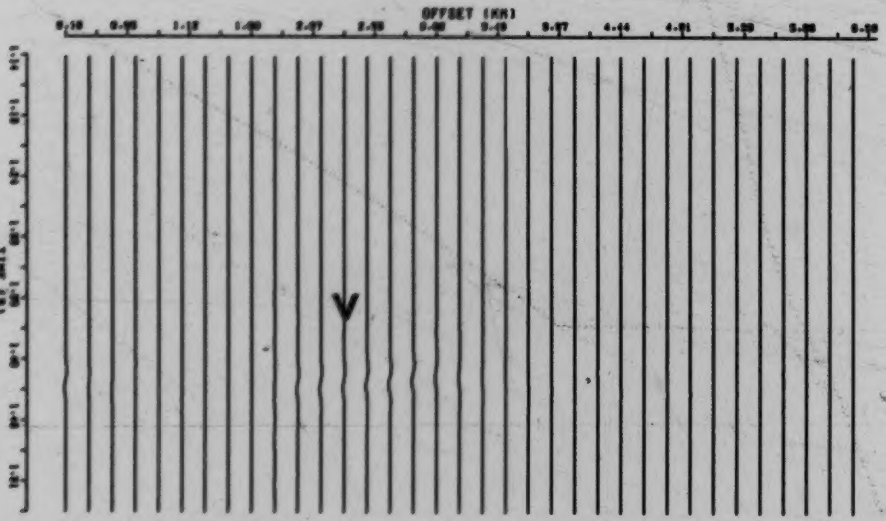

Figure 2.17: The difference between the exact and asymptotic (non-uniform formulae) reflections from the first interface.

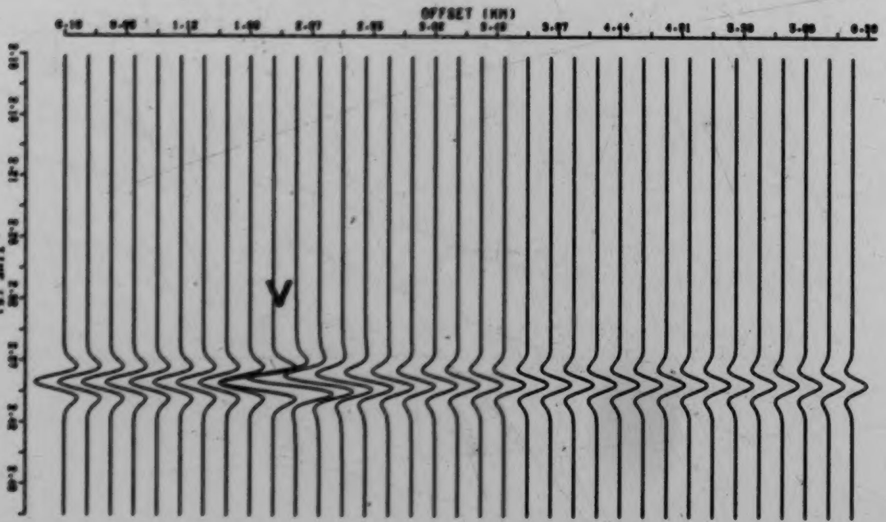

Figure 2.18: The zero order ART approximation of the reflected wave from the third interface, using the adjusted model of Figure 2.11. The critical offset is at 1.79 km.

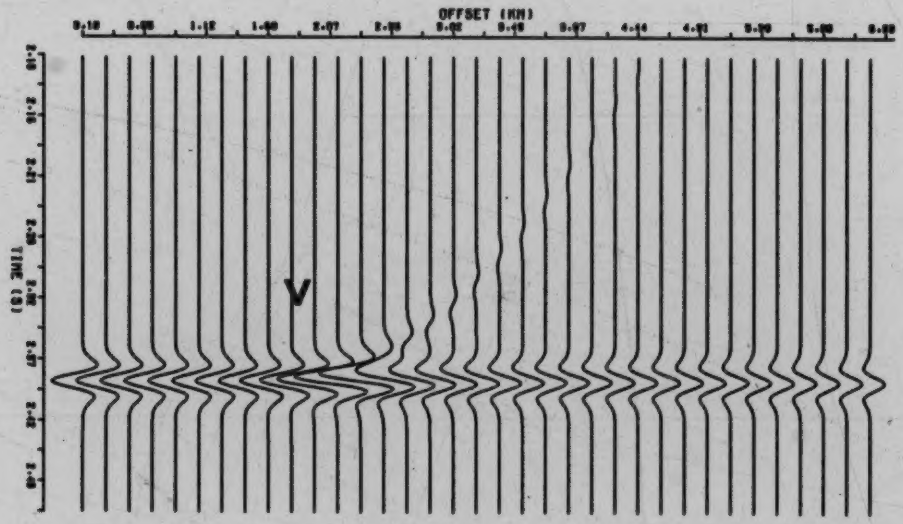

Figure 2.19: The exact reflected wave from the third interface (adjusted model).

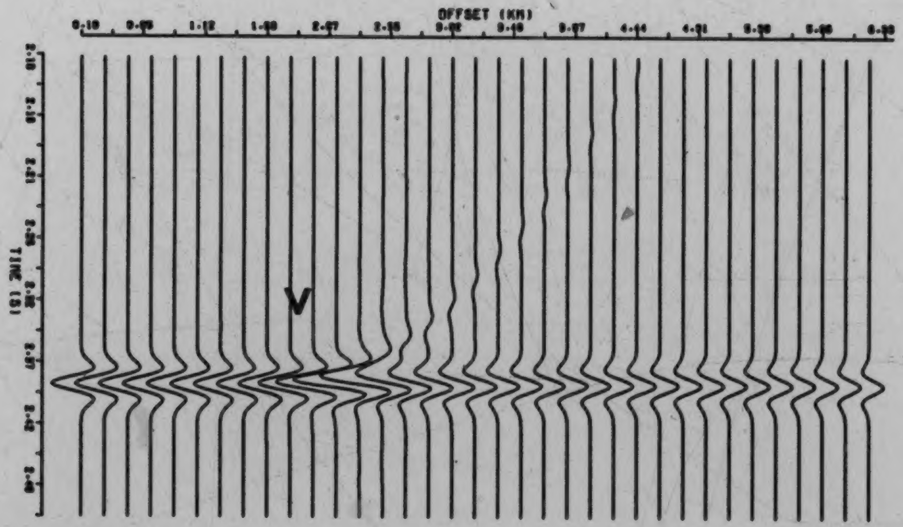

Figure 2.20: The non-uniform asymptotic reflected wave from the third interface (adjusted model).

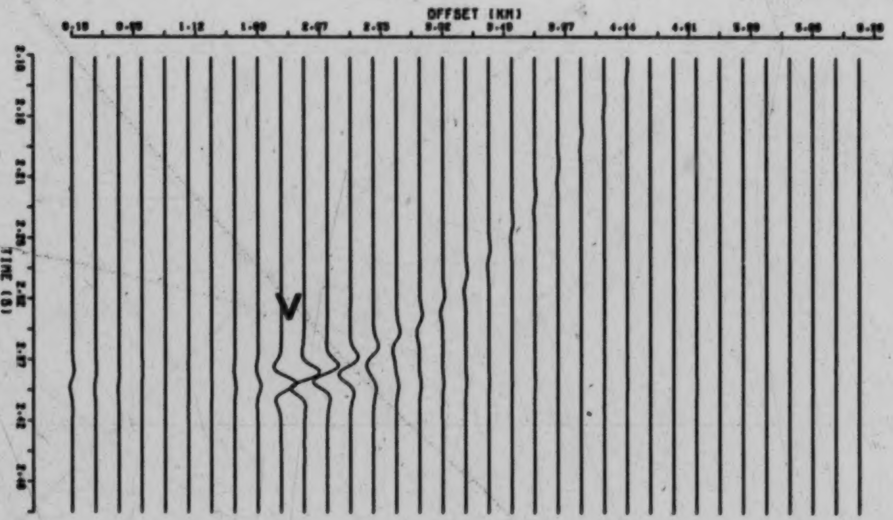

Figure 2.21: Error in ART seismograms for reflection from third interface (adjusted model.

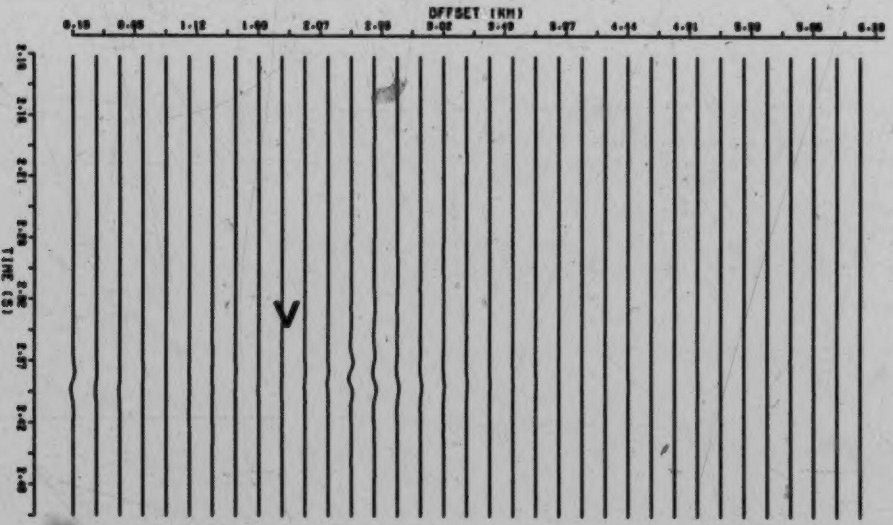

Figure 2.22: Error in asymptotic (Case formulae) seismograms for the reflection from third interface (adjusted model).

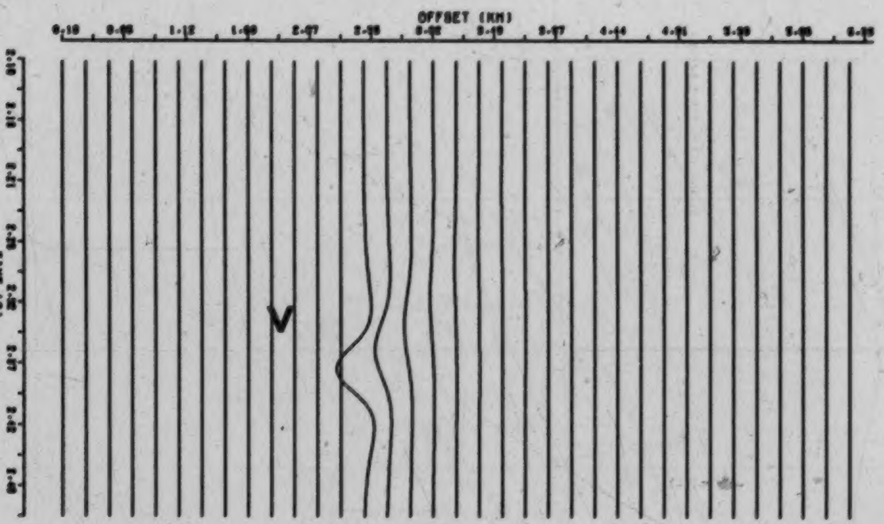

Figure 2.23: The leaky pulse for the reflection from the third interface (arising from the residue contribution). The pulse is quite low amplitude, so in the above figure the pulse has been magnified by a factor of 20.

It is instructive to have some quantitative measure of error in the seismograms, rather than simply looking at the scaled traces. One could look at the peak amplitude error (as a % of the exact peak amplitude); however, this doesn't tell us much about long duration amplitude errors in the time domain. To remedy this, we define the normalized average error (NAE) for a seismic trace as

$$\begin{aligned} E(r) &= \frac{\int_0^T \left(f(t) - \hat{f}(t)\right)^2 dt}{\int_0^T \left(f(t)\right)^2 dt} \\ &\approx \frac{\sum_{j=1}^N \left(f(t_j) - \hat{f}(t_j)\right)^2}{\sum_{j=1}^N \left(f(t_j)\right)^2} \end{aligned} \tag{2.2}$$

where $f(t)$ is the trace computed using exact numerical integration, and $\hat{f}(t)$ is the trace computed using a chosen approximation. The above measure of error represents the overall performance of a particular approximate waveform. The NAE is still a relative measure, but we can at least say that for $NAE \geq 1$ then the approximation is completely invalid, and we would hope for $NAE \ll 1$

(of course $NAE \geq 0$). We have calculated the NAE for the reflected P-wave from the third interface of the salt model, for both zero order ART and the non-uniform asymptotic approximations (Figures 2.24 and 2.25). We use 250 Hz as our sampling frequency, and the peak frequencies for the pulses are labelled. In both figures we see an increase in the NAE for small offsets, which is actually due to the 'exact' seismograms being calculated using the far offset approximation. Starting with Figure 2.24, the first thing we notice is that error is peaked about the two critical offsets, as one would expect. Also, error is greater in post-critical regions since the head wave is not included in zero order ART. We also note that there is no convergence to a constant error for higher frequencies. Presumably, there are higher order terms in the ray series[6] (if higher order terms did not exist we would stop getting improvement and remain at a small constant error level attributable to numerical computational differences). These higher order terms are body wave terms, because we can observe error changes with frequency even for pre-critical angles. Turning our attention to Figure 2.25, one can see a general improvement when we use the non-uniform asymptotic formulae over the zero order ART, by a factor of about 10-100. Two things are apparent: firstly, for pre-critical offsets our Case formulae actually degrade the solution ($r < 2.0$km offset), and secondly, the peak level of error seems to converge near 2.5 km offset, with all frequency curves ($f_0 > 4Hz$) attaining the same approximate NAE. The first artifact is probably due to our overestimating the size of the boundary layer for pre-critical offsets. In fact, you can actually see at what point we switch from ART to another boundary layer in the non-uniform patchwork by the change in character of the lines with offset (it is different for each frequency). The second artifact is a little more disturbing; one expects from the proof of the asymptotic nature of the non-uniform approximation that for higher frequencies the error must continually approach zero as $\omega \to \infty$ (and not halt as it has at $\approx 4Hz$ around 2.5 km offset). On either side of the first critical offset it appears that everything is working properly, since the errors generally get smaller for each frequency increase. The error peak (at about $NAE \approx 10^{-2}$) actually moves inwards (towards the critical offset) at each frequency doubling, for frequencies greater than 4 Hz. This indicates that the error is moving like the edge of a boundary layer, which gives us a clue to the cause of the problem. What happens is that error builds up towards the edge of a boundary layer because we are using non-uniform formulae. It not only accumulates, but increases *in proportion to the frequency*, to offset our asymptotic convergence to zero. The source of the error can be traced to our derivation of the non-uniform formula, where we approximated the exponent as a Taylor series about the saddle point. We assumed that only the leading term in

---

[6] We have established this near the critical offsets back in Chapter 1, but have not shown this to be true for regions of standard reflection. It is intuitively true since zero order ART is only a leading term of a series that follows, but one needs to do the algebra to show the higher terms are actually non-zero.

$$e^{\omega(\phi-\psi(p;p_0))} \sim 1 + O(\omega(\phi - \psi(p;p_0))) \tag{2.3}$$

was significant, where $\hat{\psi}(p;p_0)$ is the two term Taylor expansion of ϕ about the saddle point. Now, for post-critical angles part of the steepest descents contour loops a branch point, and the above approximation gets worse towards the edge of boundary layers (where $\phi - \psi(p;p_0)$ is no longer small on the loop contour). We see that the neglected term on the RHS of equation (2.3) indeed has the frequency dependence that our error in Figure 2.25 clearly has. This also explains why the error peak is located at the edge of a boundary layer for only post-critical offsets, since for pre-critical offsets there is no loop contour.

Based on the convergence of the error to a fixed quantity we can actually make conclusions regarding the accuracy of our non-uniform approximation. We see that the peak error in Figure 2.25 is consistently close to the error in zero order ART for a 4Hz wave under 'clean' conditions, i.e. non-zero reflection coefficient far from a critical offset, which, for us, is $.5 < r < 1.5$km. If we denote the radius of curvature of the wavefront (returning to the surface) in the plane of incidence by r_{curve}, and the wavelength in the top medium by λ_1, then we conclude the following: if a seismologist were satisfied with the result that zero order ART produced for

$$\frac{r_{curve}}{\lambda_1} \approx 13 \tag{2.4}$$

for their particular situation (even though they may be using a higher frequency), then the non-uniform approximations could be expected to produce adequate results when head waves and leaky waves come into play. The above ratio was calculated for a 4Hz wave reflected from the third interface at zero offset.

2.5 Chapter Summary

We have plotted contours of leaky poles on the $(-+++)$ and $(--++)$ sheets by varying the ratio α_1/α_2 and Poisson's ratio in both the top and bottom media. This has provided us with an intuitive picture of the situations when leaky poles are of importance; that is, when they move close to branch points. Generally speaking, strong contrasts in velocity across an interface tend to generate leaky pulses which interfere with head and reflected waves.

The non-uniform formulae derived in Chapter 1 have been visually compared to exact results, using amplitude vs. offset curves at 20Hz and seismograms whose peak frequency is located at 20Hz. The formulae appear to work satisfactorily, although some fine tuning of the size of the boundary layers may further improve the results. It is clear that the formulae of Červený and Ravindra fail when leaky poles approach a branch point in the complex ray parameter plane, and that our new formulae correctly account for the poles' influence. The AVO curves also showed that a pole may have a pronounced influence, even though it has not been crossed by the steepest descents contour (so no residue was taken). Finally, we carried our a numerical comparison of the integrated, normalized mean square error in the time domain, for a variety of peak frequencies. It was found that errors in our non-uniform approximation accumulate at the edge of the boundary layers, and are frequency dependent. This implies that our formulae are not arbitrarily

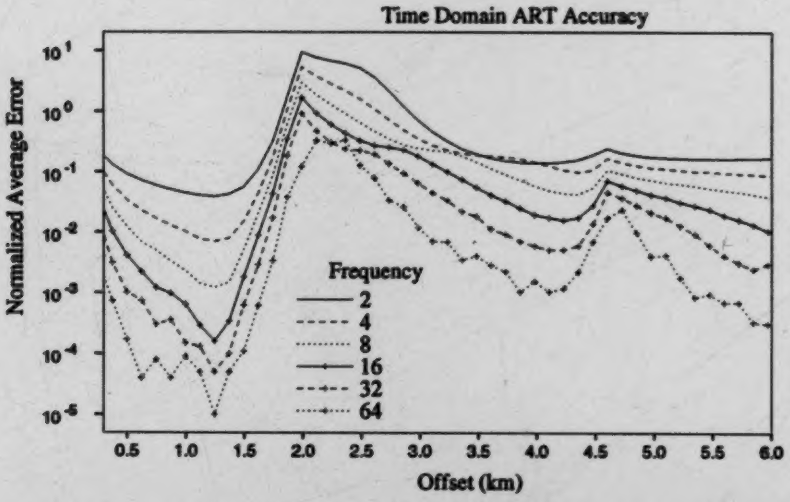

Figure 2.24: The normalized average error for zero order ART and exact seismograms. The wave modelled is the P-wave reflected from the third interface of the salt model. There are 50 receivers at which comparisons are made, and frequencies are measured in Hertz.

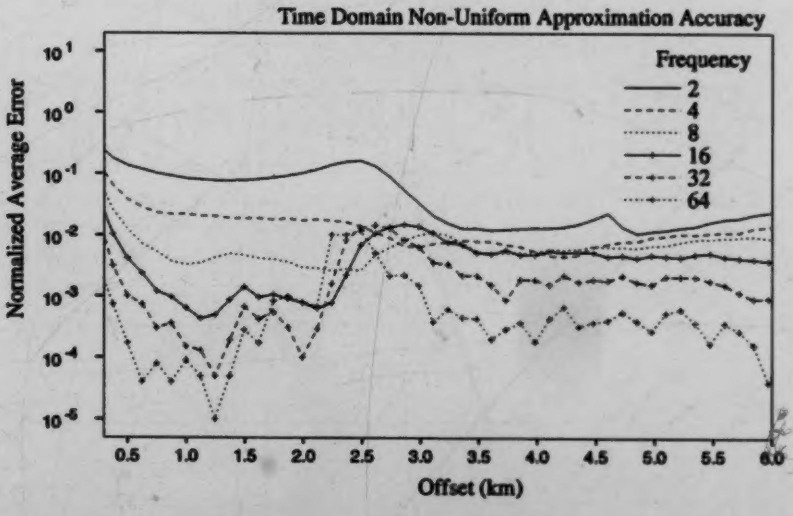

Figure 2.25: The normalized average error for non-uniform asymptotic and exact seismograms. The setup is the same as in Figure 2.24.

accurate as $\omega \rightarrow \infty$ (unlike zero order ART), but rather have an approximately fixed peak error. By comparing with the errors in ART, we found that the error in the non-uniform approximation is consistent with that of zero order ART (away from critical angles) at about 10 wavelengths from the source. Since ART is considered applicable for anything over 3 wavelengths from the source, we can safely say that our results are valid.

Chapter 3

Numerical Techniques

3.1 Introduction

This chapter is devoted to outlining the techniques needed to carry out calculations that arose in our exact and asymptotic characterization of seismic waves from Chapters 1 and 2. We have previously derived a high frequency approximation to an integral of the sort

$$I = \int_{-\infty}^{\infty} f(p) e^{\omega\phi(p)}\, dp. \tag{3.1}$$

To evaluate the accuracy of the asymptotic formulae, it is necessary to compare the results to those of an 'exact' method. That is, we desire a numerical estimate of I, no matter how computationally inconvenient this may prove. In this chapter we shall look at two general approaches for calculating the exact solutions. We assume that f contains no Hankel function, so that the far offset approximation has already been made (this is why we put exact in quotes). A good summary of techniques can be found in Chapman and Orcutt (1985). It is also necessary to evaluate some special functions connected with the asymptotic expansion of equation (3.1). We have found that suitable routines are often not available, and we therefore present methods to calculate these functions. We also briefly look at the technique used to locate our poles in the complex plane.

3.2 Real Contour Method

The contour of integration is taken along the real axis in this case. This is the simplest choice, and coincidentally is also the path for which the method of stationary phase applies, if one were interested in approximating I in this manner. We shall demonstrate this below.

Assuming an n layered medium, that the response is a P-wave along every leg of its path, and that the source and receivers are a height h_1 above the first interface, then we can write

$$\phi(p) = i(rp + \sum_{k=1}^{n} 2h_k\sqrt{1/\alpha_k^2 - p^2}) \tag{3.2}$$

as was shown in Chapter 1. The point of stationary phase (or saddle point for that matter) is given by $\phi'(p_0) = 0$. The path from the stationary point along which $Im\{\phi\}$ changes most rapidly is that for which $Re\{\phi\}$ is constant[1] Thus the stationary phase path is characterized by

$$Re\{\phi(p) - \phi(p_0)\} = 0 \tag{3.3}$$

and p_0 is a point on the positive real axis. For $p \in \Re$ and $|p| < 1/\alpha_k$, $k \leq n$, then we see from equation (3.2) that ϕ is purely imaginary, and so the stationary phase path lies along the real axis in this range of p. We point out that p_0 should lie in this range too, otherwise we are describing waves that decay exponentially in depth (we would like to consider homogeneous waves only).

Now that we have shown that this contour is the path for stationary phase, it so happens that this makes it one of the more challenging types of integral to tackle, from a computational point of view. The problem lies in that highly oscillatory integrands must be sampled rather intensively to prevent aliasing. Most terms in the sum (except around the point of stationary phase) should cancel, but alaising builds up error. This can be put more precisely if we look at some of the work of Frazer and Gettrust (1984), who examine error bounds for various quadrature schemes. These arguments are also necessary to understand the advantage of the Generalized Filon's Method (GFM), also introduced by these authors.

---

[1] If $\phi = u + iv$ is an analytic function and $p = x + iy$, then it satisfies the Cauchy-Riemann equations, $u_x = v_y$ and $u_y = -v_x$. The direction and magnitude of the maximum variation in these functions can be represented in vector form: ∇u and ∇v. It is immediately clear that $\nabla u \cdot \nabla v = 0$, as a consequence of the Cauchy-Riemann equations. Thus $u = constant$ along the path for which v is most rapidly changing.

Approximating an integral using an N^{th} order interpolatory quadrature scheme consists of the following:

$$g(x) = \sum_{k=0}^{N} g(x_k) l_k(x) + \frac{g^{(N+1)}(z)}{(N+1)!}(x-x_0)(x-x_1)...(x-x_N) \tag{3.4}$$

$$\int_a^b g(x)\,dx = \sum_{k=0}^{N} \xi_k g(x_k) + \int_a^b \frac{g^{(N+1)}(z(x))}{(N+1)!}(x-x_0)(x-x_1)...(x-x_N)\,dx \tag{3.5}$$

where ξ_k are the weights, x_k are the nodes and $l_k(x)$ are the well known Lagrange Polynomials. Thus an upper bound on the error expressed as a fraction of the original integral is

$$E_N = \frac{(b-a)^{N+1}\sup[g^{(N+1)}]}{(N+1)!\sup[g]}, \tag{3.6}$$

where sup[] acts upon the closed interval $[a, b]$. So when considering integrating a function of the sort

$$g(x) = f(x)e^{\omega x}, \quad \omega \to \infty \tag{3.7}$$

then we see that since $f^{(N+1)} \sim f\,\omega^{N+1}$ that

$$E_N \sim \frac{(b-a)^{N+1}\omega^{N+1}}{(N+1)!}. \tag{3.8}$$

This leads to a reasonable maximum size for the interval size (assuming a $\beta\%$ error),

$$(b-a)_{MAX} = \left(\frac{\beta\sup[g](N+1)!}{\sup[g^{(N+1)}]}\right)^{\frac{1}{N+1}} \tag{3.9}$$

for regular integrands, and

$$(b-a)_{MAX} = \omega^{-1}[\beta(N+1)!]^{\frac{1}{N+1}} \tag{3.10}$$

for exponential ones. We can see from the above formula that the stepsize is controlled by the large parameter (ω). Thus for higher frequencies the quadrature scheme becomes more unwieldy, requiring a large number of function evaluations. We have assumed that an interpolatory quadrature method is best for evaluating the integral. In the 'Complex Contour' section we shall be using the Runge-Kutta method, and we shall delay our explanation until then, as to why it is not appropriate for highly oscillatory integrals. For now we implement a common

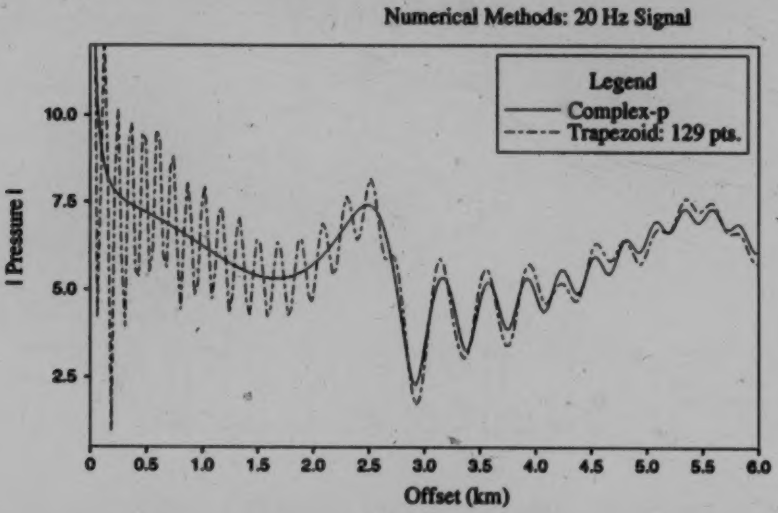

Figure 3.1: Comparison of reflected P-wave from the third interface of the salt model, for the 129 pt trapeziodal numerical integration.

trapezoidal scheme (Press et. al., 1992), to the integral representing the pressure of the wave reflected from the third interface in the salt model defined in Chapter 2. This is done to have a comparison with other methods. We need endpoints for the integration (a and b), and have found that $p \in [0, 1/\alpha_3]$ seems to work. This implies that the reflected wave can be well represented by a sum of homogeneous plane waves with positive angles of incidence. (For $p > 1/\alpha_3$ the exponent $\phi(p)$ would not be purely imaginary, meaning that the wave decays exponentially in the 3^{rd} medium.) Dividing the interval into M subintervals

$$I \approx \Delta/2[g(a)+g(b)] + \Delta \sum_{k=1}^{M-1} g(a+\Delta k) \tag{3.11}$$

where we have applied the trapezoidal rule to each interval. One can see in Figure 3.1 the result for a 20 Hz monochromatic wave. The computation was carried out for 200 receivers. The number of intervals used was 128 (129 points). The accuracy is poor, and in Figure 3.2 we use 256 intervals, and get an improvement, although it is not perfect. For comparison we have used the 'complex-p' method where we integrate along a complex contour, a discussion of which is given in a later section. We see a degradation of the quality of the integration at near offsets. This is a result of the far-offset approximation, as well as having fixed the endpoints of integration at $p = 0$ and $p = 1/\alpha_3$. At near offsets the stationary point (p_0) moves closer to the boundary $p = 0$, and the lower endpoint should be moved to the negative real axis if we are to gain near offset accuracy. When computing seismograms one needs to evaluate many frequencies, and generally they are higher

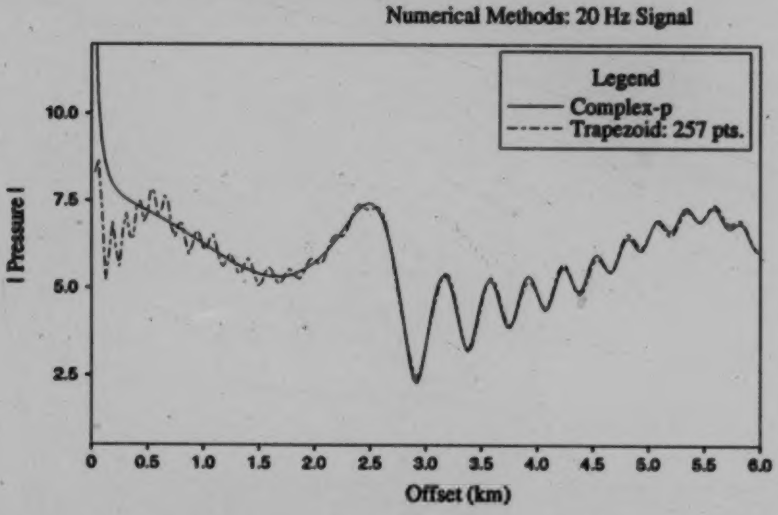

Figure 3.2: Comparison of reflected P-wave from the third interface of the salt model, for the 256 pt. trapezoidal numerical integration.

than 20 Hz. We therefore look to another quadrature scheme which has often been used in seismology in connection with the reflectivity method.

3.2.1 Filon's Method

This method is based upon exactly integrating some oscillatory portion of the integral, while expanding the rest in the usual Lagrange polynomial. Specifically,

$$\int_a^b f(x)e^{\omega x}\,dx = \sum_{k=0}^{N} f(x_k)\eta_k + \int_a^b e^{\omega x}\frac{f^{(N+1)}(z(x))}{(N+1)!}(x-x_0)(x-x_1)\ldots(x-x_N)\,dx \tag{3.12}$$

where now the weights, η_k, are moments of the exponential term (previously they were polynomial). From the previous error expressions we see that now

$$E_N = \frac{(b-a)^{N+1}\sup[f^{(N+1)}]}{(N+1)!\sup[f]} \tag{3.13}$$

so the interval size is independent of the large parameter (frequency). This method rests on being able to calculate η_k easily, which requires a simple exponential function (it is simply x in this example). Unfortunately, our integrals contain a more complicated exponent, as was shown in equation (3.2). One could split the exponent, using Filon's method on $i\omega rp$ and using the interpolatory polynomial on $i\omega\sum_{k=1}^{n} h_k\sqrt{1/\alpha_k^2 - p^2}$. However, this was found to produce negligibly better results. We therefore turn to the method introduced by Frazer and Gertrust (1985), which works for a general function in the exponent.

3.2.2 Generalized Filon Method

To apply this method one need only rewrite our integral in the form

$$\int_a^b f(x)e^{\omega\phi(x)}\,dx = \int_0^{b-a} h(q)e^{\sigma q}\,dq \tag{3.14}$$

where $q = x - a$, $\sigma = \omega[\phi(b) - \phi(a)]/(b-a)$ and

$$h(q) = f(q+a)e^{\omega\phi(q+a)-\sigma q}.$$

This is an exact transformation. Next, Filon's method is applied to the RHS of equation (3.14). Using our error bounds from before, we find that

$$(b-a)_{MAX} = \left(\frac{\beta(N+1)!}{\sup[\phi'']}\right)^{\frac{1}{2N+2}} \omega^{-1/2}, \tag{3.15}$$

since

$$\begin{aligned} \sup[h^{(N+1)}] &\sim \omega^{N+1} \sup\left[h\left(\phi' - \frac{\phi(b)-\phi(a)}{b-a}\right)^{N+1}\right] & (3.16)\\ &= \omega^{N+1} \sup[h(\phi'')^{N+1}](b-a)^{N+1} & (3.17) \end{aligned}$$

due to the Mean Value Theorem. Therefore this method does not require so stringent a restriction upon the maximum interval size, when compared with a regular interpolatory quadrature scheme (contrast the dependence on ω above with that in equation (3.10)). Ultimately, however, the interval size still depends upon the frequency of the wave, making it unattractive computationally.

Conjecture 2 *We could make the exact transform $t = \phi(x)$ to obtain a simple exponential function, and then apply Filon's Method to the resulting integral.*

This turns out to be a bad idea, since

$$\frac{dx}{dt} = \frac{1}{\phi'(x)}$$

and there is always a saddle point at which $\phi'(x) = 0$. Thus the integrand is now singular, and we have merely exchanged one set of problems for another. If we transform to a second order polynomial to alleviate the singularity, we introduce unwieldy integrals as 'primitives'; that is, the weights themselves become special functions.

Here we shall derive the exact formulae used in implementing GFM. Firstly we need to calculate the weights for the Filon Method. We shall use a three point or parabolic interpolation of the integrand, the points being equally spaced. Let the original integral be of the form

$$I = \int_0^1 \Gamma(x)e^{\lambda x}\,dx \tag{3.18}$$

where λ is a constant, and $\Gamma(x)$ is some function to be interpolated. An expansion of the form given in equation (3.5) is clearly exact ($E_N = 0$) if $g(x)$ (or $\Gamma(x)$ for the above equation) is an N^{th} order polynomial (or less). We have chosen a parabolic interpolation, so $N = 2$. That this must be exact for a polynomial of degree two or less allows us to find the weights from the solution of the following system:

$$\begin{aligned} \xi_0 + \xi_1 + \xi_2 &= W_0 = \int_0^1 e^{\lambda x}\, dx \\ 0\xi_0 + 1/2\xi_1 + \xi_2 &= W_1 = \int_0^1 x e^{\lambda x}\, dx \\ 0\xi_0 + 1/4\xi_1 + \xi_2 &= W_2 = \int_0^1 x^2 e^{\lambda x}\, dx. \end{aligned} \tag{3.19}$$

The result is easily evaluated, and we can use the weights to approximate the integral given in equation (3.18). Now, our integral that we want to calculate has limits of integration $[a, b]$, and we divide this into M subdivisions, each of width Δ. Each subdivision contributes to the integral and looks like

$$\Delta I_j = \int_{a+j\Delta}^{a+\Delta+j\Delta} f(p) e^{\omega\phi(p)}\, dp \tag{3.20}$$

to which we apply the transformation in GFM to get

$$\Delta I_j = \int_0^\Delta \left(f(p(q)) e^{\omega\phi(p(q))-\sigma q}\right) e^{\sigma q}\, dq \tag{3.21}$$

where $p = q + a + j\Delta$, and $\sigma = \omega[\phi(a + j\Delta + \Delta) - \phi(a + j\Delta)]/\Delta$. Next we need to transform this to the range [0,1] to make use of our weights calculated in equation (3.19). Thus let $s = q/\Delta$ and then

$$\Delta I_j = \Delta \int_0^1 \left[f(a + j\Delta + s\Delta) e^{\omega(\phi(a+j\Delta+s\Delta)}\right] e^{s\sigma\Delta}\, ds \tag{3.22}$$

and if we identify $\lambda = \sigma\Delta$ and $\Gamma(x) \to \Gamma(x, j)$ as being all terms in square brackets in equation (3.22), then we can write formula approximating the integral as

$$I \approx \Delta \sum_{j=0}^{M-1} \xi_0(j)\Gamma(0, j) + \xi_1(j)\Gamma(1/2, j) + \xi_2(j)\Gamma(1, j). \tag{3.23}$$

We have expressed explicit dependence upon the index j, where it occurs. There is some redundancy in the above formula, in the sense that if one uses this directly as an algorithm, there sometimes will be two function evaluations at the same spot. This reduces efficiency when we have complicated integrands to compute.[2] Let's split apart the function in the integrand as follows:

$$\Gamma(s,j) = \gamma(s,j) \cdot e^{-s\sigma(j)\delta},$$

and we see by inspecting earlier expressions that

$$\gamma(0,j) = \gamma(1,j-1).$$

Therefore we write

$$\begin{aligned} I \;\approx\;& \Delta\left\{\xi_0(0)\gamma(0,0) + \xi_1(0)\gamma(1/2,0)e^{-\sigma(0)\Delta/2} + \right. \\ & \left. \xi_2(M-1)\gamma(1,M-1)e^{-\sigma(M-1)\Delta}\right\} + \\ & \Delta\sum_{j=1}^{M-1}\left\{\left[\xi_0(j) + \xi_2(j-1)e^{-\sigma(j-1)\Delta}\right]\gamma(0,j) + \right. \\ & \qquad \left. \xi_1(j)\gamma(1/2,j)e^{-\sigma(j)\Delta/2}\right\}. \end{aligned} \tag{3.24}$$

Figure 3.3 illustrates the result of applying the GFM to our model, when 129 point evaluations are used. We see that generally the match is better than for the trapezoidal result, even when using one half the number of points. Of course, for a fixed number of points, there is somewhat more computation required for GFM than the trapezoidal rule (one can see by inspection of the formulae). However, for a certain desired accuracy, the savings in time using GFM is very significant, due to the lower number of points needed to achieve the desired accuracy. The decreased performance at near offsets in Figure 3.3 is again a result of our choice that the lower limit of integration be at $p = 0$. As a final note on GFM, we point out that there are instances for which $|\lambda|$ in equation (3.19) can be small, and a straightforward evaluation of the integrals giving the weights W_0, W_1 and W_2 can

---

[2] Remember the number of multiplications needed to produce reflection coefficients!

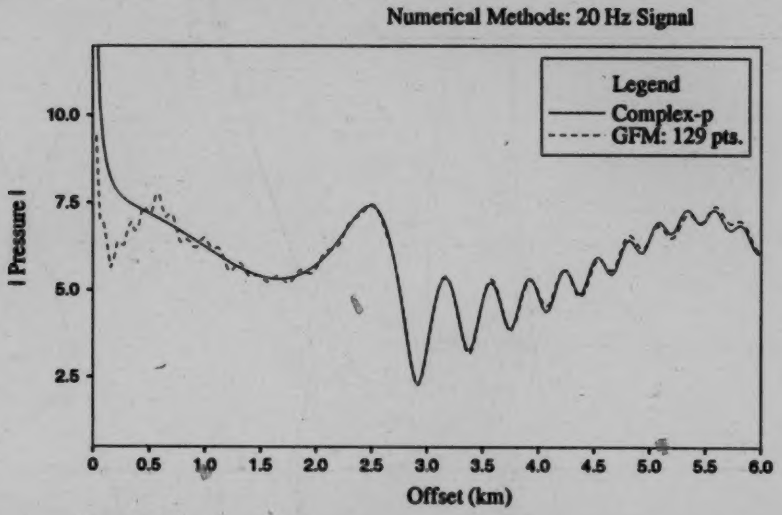

Figure 3.3: Comparison of reflected P-wave from the third interface of the salt model, for the 129 pt. GFM numerical integration.

produce very large errors. This is due to cancellation errors, and can be alleviated by using an alternative series expansion of the integrals, for small $|\lambda|$.

3.3 Complex Contour

Our troubles with oscillatory integrands can be cured if we deform the contour of integration away from the real axis. Instead of following the path of stationary phase, we follow the path of steepest descents. Along this path $Im\{\phi\}$ is constant, and $Re\{\phi\} < 0$. (Recall that this means that the integrand will have minimum oscillation). Although it simplifies the numerical integration, we now have the added complication of calculating the steepest descents contour. For a single interface this can be done in closed form (Aki and Richards, 1980) but for a series of layers this must be computed numerically. Let's use the exponent given in equation (3.2), and use the fact that $Im\{\phi(p)\} = Im\{\phi(p_0)\}$ along the steepest descents contour. Then,

$$\begin{aligned} rp + \sum_{k=1}^{n} 2h_k\sqrt{1/\alpha_k^2 - p^2} &= \\ rp_0 + \sum_{k=1}^{n} 2h_k\sqrt{1/\alpha_k^2 - p_0^2} + iX^2 & \end{aligned} \tag{3.25}$$

where $X \in \Re$. We have introduced a parametric variable X, which describes the steepest descents contour, and has initial point $X = 0$, $p = p_0$. By differentiating both sides we get

$$\frac{dp}{dX} = \frac{2iX}{r - \sum_{k=1}^{n} \frac{2h_k}{\sqrt{1/\alpha_k^2 - p^2}}}. \tag{3.26}$$

It should be pointed out that equation (3.26) can describe the increment of steepest descents path *from any point*, not just p_0. When used from p_0 though, there is a (removable) singularity at $X = 0$. We can resolve this by using l'Hospital's rule to get

$$\left.\frac{dp}{dX}\right|_{X=0} = \pm \frac{e^{-i\pi/4}}{\left[\sum_{k=1}^{n} \frac{2h_k}{\alpha_k^2 (1/\alpha_k^2 - p_0^2)^{3/2}}\right]^{1/2}}. \tag{3.27}$$

where the sign depends upon which way one is going along the steepest descents contour. We can now use a quadrature scheme to calculate

$$I = \int_{C_s} f(p) e^{\omega\phi(p)} \frac{dp}{dX}\, dX \tag{3.28}$$

where the integrand is evaluated at the discrete points, X_j, and it is understood that $p = p(X)$. To find $p(x_j)$ another quadrature must be applied:

$$p(X_j) = p(X_{j-1}) + \int_{X_{j-1}}^{X_j} \frac{dp}{dx}\, dx \tag{3.29}$$

which starts from $X = 0$, $p = p_0$ and continues outwards. Another way to formulate the problem is by writing

$$\frac{dI}{dX} = f(p) e^{\omega\phi(p)} \frac{dp}{dX} \tag{3.30}$$

so in combination with equation(3.26) we have a system of the form

$$\frac{d}{dX}\begin{bmatrix} I \\ p \end{bmatrix} = \begin{bmatrix} f_1(X,p) \\ f_2(X,p) \end{bmatrix}, \tag{3.31}$$

where the initial conditions are

$$\begin{bmatrix} I \\ p \end{bmatrix}_{X=0} = \begin{bmatrix} 0 \\ p_0 \end{bmatrix}$$

and we must sum the contributions from either side of the saddle point (i.e. solve the system twice, once in each direction). Actually, we split this into real and imaginary parts and thus must solve four equations simultaneously. To solve this system we engage the fourth order Runge-Kutta driver with adaptive stepsize control of Press et. al. (1992). The Runge-Kutta method is well known, and hence we shall not derive the formulae here. However, we shall look at the nature of the algorithm to bring to light its strengths and weaknesses when applied to our particular problem. The basic idea can be traced to Euler's method, where given an equation (or system thereof)

$$\frac{dy}{dx} = f(y,x), \qquad y(x_0) = y_0 \tag{3.32}$$

then a recursive algorithm is defined

$$y_{j+1} = y_j + hf(y_j, x_j) \tag{3.33}$$

where $x_j = j(x - x_0)/N$, N being the total number of steps. It is then expected that $y_N \approx y(x)$. Convergence and stability of the algorithm (assuming existence and uniqueness of the solution) is related to the response of $f(y,x)$ to perturbations in y.[3] The concept of 'absolute stability' (Gear, 1971) is perhaps of more practical interest, which relates whether an algorithm amplifies or damps errors that creep into any numerical procedure when using floating point number representation. That is to say, stability implies that the output (y) depends continuously upon the input y_0 for all stepsizes, but absolute stability implies that a perturbation of the input causes a similar (but not larger) perturbation in the output. One can see that to first order

$$\frac{d}{dx}\delta y = \frac{\partial f}{\partial y}\delta y \tag{3.34}$$

---

[3] The RHS of equation (3.32) must satisfy the Lipschitz condition - see Stoer and Bulirsch (1993) for details.

or for a matrix

$$\frac{d}{dx}\begin{bmatrix}\delta y_1\\ \delta y_2\end{bmatrix}=\begin{bmatrix}\frac{\partial f_1}{\partial y_1} & \frac{\partial f_1}{\partial y_2}\\ \frac{\partial f_2}{\partial y_1} & \frac{\partial f_2}{\partial y_2}\end{bmatrix}\begin{bmatrix}\delta y_1\\ \delta y_2\end{bmatrix}, \tag{3.35}$$

where the matrix on the RHS is the Jacobian. $\partial f/\partial y$ is a parameter, which we call λ, that is important in the growth of δy. The above matrix equation can be reduced to a sequence of equations of the form similar to that given in equation (3.34) if it is diagonalizable (i.e. we must find its eigenvalues and eigenvectors). For any particular algorithm, the region of absolute stability is the combination of stepsize h and parameter(s) λ, such that each step does not increase errors (δy). Now, for the system we are considering,

$$\frac{d}{dX}\begin{bmatrix}\delta I\\ \delta p\end{bmatrix}=\begin{bmatrix}0 & \frac{\partial f_1}{\partial p}\\ 0 & \frac{\partial f_2}{\partial p}\end{bmatrix}\begin{bmatrix}\delta I\\ \delta p\end{bmatrix}. \tag{3.36}$$

Clearly $d(\delta I)/dx$ doesn't depend upon δI, and so we say that this calculation is absolutely stable. In addition, δp need not be absolutely stable since analytic deformation of the contour does not affect the value of the integral. Thus our system in equation (3.31) can be considered absolutely stable.

It is natural to wonder why then, if the Runge-Kutta method is absolutely stable for different paths of integration, does it produce poor results for real axis integration? (We referred to this earlier, and it is one of the reasons we used a quadrature scheme for real axis integration). The answer lies in the fact that we are using equation (3.31) to approximate our function (I) locally. Use of this equation implies that for any numerical step routine

$$y(x+h)-y(x)\approx h\frac{dy}{dx}$$

to leading order (or some combination of the above at points interior to $[x, x+h]$ to achieve 4th order accuracy). However, for a highly oscillatory integrand such as is found using the real axis integration, the function itself y is rapidly varying (here we view I as a function of p) and the higher order derivatives are important in determining the dynamic behavior of y. In other words, there are many places for which $dy/dx \rightarrow 0$, and the above approximation is poor. This may seem odd at first based on the form of the integrand in equation (3.28) (where is it zero?), but remember we integrate the real and imaginary parts separately. Therefore the overall result proves to be unreliable, and we only use the Runge-Kutta method in conjunction with the steepest descents contour method.

Adaptive stepsize control allows the numerical routine to quickly jump across smooth function 'territory', while being careful in regions that the function is rapidly varying. This is particularly useful for steepest descents integrals,[4] since the contour length can be fixed at some overestimate, without losing much efficiency. The results of using a complex contour and an ODE solver to evaluate our original integrals has been shown in Figures 3.1 to 3.3, where it really sets the standard for accuracy. Clearly it is more stable than the quadrature methods, at all frequencies, and approximately requires the same computation time as GFM (for the 20 Hz signal studied). The singularity at near offsets is again due to the far offset approximation rather than any instability of our method. It should be pointed out that while we have gained a seemingly superior method, it is more complicated to code, and requires a greater knowledge of the media parameters. For example, when the steepest descents contour crosses a leaky pole (for increasing offsets) the algorithm must recognize this, and add a residue. Otherwise the amplitudes become discontinuous. Similarly, at post critical angles, we need to introduce descents contours from branch points. From this point of view, real axis integration is easier as it requires one contour and no knowledge of the positions of saddle, branch and pole points in the complex ray-parameter plane.

---

[4] The integrand is concentrated at the saddle point, and the length of the contour needed to properly characterise the total integral is frequency dependent. This is in contrast to the real axis integration, where the length of the contour is fixed.

3.4 Special Functions

The asymptotic approximations of Chapter 1 require several parabolic cylinder functions as well as the new function $\mathcal{F}$. Very often one can find existing subroutines for evaluating special functions (IMSL or NSWC compilations). However, we found that parabolic cylinder functions of arbitrary argument and order are not among them. We therefore derived computational schemes, relying heavily on the work of Press et. al. (1992).

3.4.1 $D_{1/2}(z)$ and $D_{3/2}(z)$

These could be calculated from their integral definitions, much as we reduced our integral I into solving a system of 1^{st} order ODE's. However, we choose to take their defining differential equation and do the same thing:

$$\frac{d^2 D_p}{dz^2} + (p + 1/2 - z^2/4) D_p = 0 \tag{3.37}$$

can be rewritten

$$\frac{d}{dz}\begin{bmatrix} C_p \\ D_p \end{bmatrix} = \begin{bmatrix} 0 & z^2/4 - p - 1/2 \\ 1 & 0 \end{bmatrix} \begin{bmatrix} C_p \\ D_p \end{bmatrix} \tag{3.38}$$

where $C_p = dD_p/dz$. The initial vector is given at $z = 0$ by

$$\begin{bmatrix} \frac{\Gamma(1/2)2^{p/2}}{\Gamma((1-p)/2)} \\ \frac{\Gamma(-1/2)2^{(p-1)/2}}{\Gamma(-p/2)} \end{bmatrix}$$

where $\Gamma(x)$ is the gamma function. Again, we actually end up splitting equation (3.38) into a system of four equations, to integrate the real and imaginary parts separately. For the functions $D_{1/2}(z)$ and $D_{3/2}(z)$ we only need z for a fixed argument, namely $z = se^{-i\pi/4}$, $s \in \Re$. The above system can be solved using the Runge-Kutta single step routine as before, starting from $s = 0$ and progressing outward to the desired s. We have problems determining the stability of the stepping routine, since

$$\frac{d}{dz}\begin{bmatrix} \delta C_p \\ \delta D_p \end{bmatrix} = \begin{bmatrix} 0 & z^2/4 - p - 1/2 \\ 1 & 0 \end{bmatrix} \begin{bmatrix} \delta C_p \\ \delta D_p \end{bmatrix} \tag{3.39}$$

and the RHS is a function of z. Unfortunately the coefficients are functions of the independent variable, so we cannot obtain the form $d(\delta D_p)/dz = \lambda \delta D_p$. However, we found through experimentation that the result was absolutely stable when compared to the tables of Kireyeva and Karpov (1961). While the ODE integration leads to an accurate result, we can devise faster methods without much loss in precision. We constructed an algorithm which computes a reasonable approximation to $D_p(z)$ in three regions:

$$\begin{array}{rcl} \text{Zone 1: } |z| \ll 1 & \Rightarrow & \text{Taylor Expansion} \\ \text{Zone 2: } |z| \gg 1 & \Rightarrow & \text{Asymptotic Expansion} \\ \text{Zone 3: Other values of } |z| & \Rightarrow & \text{Interpolating Polynomial} \end{array}$$

The first two zones have formulae described in Kireyeva and Karpov (1961). For Zone 3, we find the coefficients for two polynomials which mimic the behavior of $Re\{D_p(z)\}$ and $Im\{D_p(z)\}$ over intermediate ranges of $|z|$. We employ Chebyshev polynomials, using the subroutines of Press et. al. (1992). There are two properties which make Chebyshev polynomials particularly attractive: the coefficients fall off in amplitude rapidly for higher terms in the series, and the polynomials are oscillatory, so the error in truncating an expansion is spread out over the interval. The exact boundaries for $|z|$ can be found through comparison with the ODE integration, keeping some error bound in mind.

3.4.2 $D_{-1}(z)$

Magnus and Oberhettinger (1954) provides the following relation:

$$\frac{dD_{-1}}{dz} = z/2 - D_0.$$

Using the above as well as $G(z) = e^{z^2/4} D_{-1}(z)$,[5] we find

$$\frac{dG}{dz} = zG - 1 \tag{3.40}$$

---

[5] Note that the Formulae in Chapter 1 actually all require G(z), so this is not an inconvenience.

We have a more complex problem now because z no longer has a fixed argument (see Chapter 1). This makes interpolation more unwieldy, and so while we divide our algorithm into the zones mentioned previously, we actually carry out the ODE integration in Zone 3. Absolute stability becomes an issue here, so we look at the result of applying Euler's method to equation (3.40).[6] Putting $z = se^{i\theta}$, $s \in \Re^+$, and integrating outward from $z = 0$ along the ray $\arg\{z\} = \theta$ to a destination in Zone 3, we find

$$d(\delta G)/ds = e^{i\theta}(e^{i\theta}sG - 1). \tag{3.41}$$

Euler's method produces the recursion

$$\delta G_{j+1} = \delta G_j + he^{i\theta}(e^{i\theta}s\delta G_j - 1)$$

so for absolute stability we require

$$|hse^{i2\theta} + 1| < 1. \tag{3.42}$$

For our ODE integration to be absolutely stable, we require the above condition to hold for real and positive h and s. Actually we have

$$\theta = 0, \pi \iff -2/s < h < 0 \qquad \theta = \pi/2, 3\pi/2 \iff 0 < h < 2/s$$

and a continuum for intermediate values of θ. In practice this means that errors will accumulate whenever we are trying to find $G(z)$ for z near the real axis. Numerical experimentation has shown the above conjecture to be true. However, the errors remain at an acceptable level up to the outer edge of Zone 3, and past this we use an asymptotic expression. Thus we are spared from having to engage more complicated implicit difference techniques.

---

[6] We assume that similar results hold for the Runge-Kutta driver, and this is appropriate since we are looking only at general error trends (and not specific boundaries).

3.4.3 $\mathcal{F}(z,w)$

We actually calculate $\mathcal{F}(z,w)$ from its integral definition,

$$\mathcal{F}(z,w) = \frac{-1}{2\pi}\int_{-\infty}^{+\infty} \frac{\sqrt{t}}{t-w} e^{-t^2/2-zt}\,dt \tag{3.43}$$

although better schemes could perhaps be devised (we were unable to do so). Any type of interpolation seems unlikely, due to the fact that it is a function of two variables, and there is no restriction on the argument of w. However, it is possible to find a differential equation to describe this function, and we include this for completeness.

We can differentiate under the integral sign in equation (3.43) since the integral is uniformly convergent (the contour never crosses the singularities). Carrying this out and using the integral definition of parabolic cylinder functions from Bleistein (1986), we find

$$\frac{\partial \mathcal{F}}{\partial z} + w\mathcal{F} = \frac{e^{i\pi/4+z^2/4}}{\sqrt{2\pi}} D_{1/2}(iz). \tag{3.44}$$

Similarly,

$$\frac{\partial^2 \mathcal{F}}{\partial z^2} + w\frac{\partial \mathcal{F}}{\partial z} = -\frac{e^{i3\pi/4+z^2/4}}{\sqrt{2\pi}} D_{3/2}(iz) \tag{3.45}$$

and

$$\frac{\partial^3 \mathcal{F}}{\partial z^3} + w\frac{\partial^2 \mathcal{F}}{\partial z^2} = \frac{e^{i5\pi/4+z^2/4}}{\sqrt{2\pi}} D_{5/2}(iz). \tag{3.46}$$

Magnus and Oberhettinger (1954) provides the relationship

$$D_{5/2}(y) - yD_{3/2}(y) + 3/2D_{1/2}(y) = 0 \tag{3.47}$$

which, when combined with equations (3.44), (3.45) and (3.46) gives

$$\frac{\partial^3 \mathcal{F}}{\partial z^3} + (w - \frac{2}{3}z)\frac{\partial^2 \mathcal{F}}{\partial z^2} - \frac{2}{3}(1+zw)\frac{\partial \mathcal{F}}{\partial z} - \frac{2}{3}w\mathcal{F} = 0. \tag{3.48}$$

This can then be solved as a system of first order ODE's, if we know $\mathcal{F}, d\mathcal{F}/dz$ and $d^2\mathcal{F}/dz^2$ at some initial point. From the form of the above equations, we know all these terms if we know $\mathcal{F}$ at the initial point. Choosing $z = 0$ we have

$$\mathcal{F}(0,w) = \frac{-1}{2\pi}\int_{-\infty}^{+\infty} \frac{\sqrt{t}}{t-w} e^{-t^2/2}\,dt \tag{3.49}$$

which, unfortunately, is again an unknown function. Perhaps if the integral could be tabulated, then this might be a useful way to find $\mathcal{F}$. However, we do not pursue this option further.

One immediately supposes that it would be better to find a differential equation with w as the independent variable, since $w = 0$ would be an easily evaluated initial condition (in terms of a parabolic cylinder function). However, we have been unable to find such an ODE.

Another method of approximating $\mathcal{F}$ may lie in the use of Padé approximants. These could appoximate $\mathcal{F}$[7] over small and intermediate ranges of w, leaving only the asymptotic region. The approximations have proven very effective in other applications, far outperforming simple power series expansions (see Press et. al., 1992). To find the Padé approximant, one only need know the Taylor series expansion of $\mathcal{F}$ about $w = 0$. Formally differentiating under the integral, the Taylor series can be expressed in terms of parabolic cylinder functions (for arbitrary z), which are easily found. Thus we would arrive at an approximation for $\mathcal{F}$ valid for small and mid-range values of w, expressed in terms of parabolic cylinder functions. One would need to experiment to identify how many terms are needed, in the rational approximation, to obtain a desired accuracy.

3.5 Finding Roots

We have had occasion in the course of our investigation of leaky waves, to find the locations of poles in of the reflection coefficients in the complex ray-parameter domain. This is equivalent to finding the zeros of the denominator, which is common to all reflection-transmission coefficients:

$$\begin{aligned} D(p) = {} & \alpha_1\alpha_2\beta_1\beta_2 p^2 Z^2 + \alpha_2\beta_2\nu_1\nu_2 X^2 + \alpha_1\beta_1\nu_3\nu_4 Y^2 \\ & + \rho_1\rho_2(\beta_1\alpha_2\nu_1\nu_4 + \alpha_1\beta_2\nu_2\nu_3) + q^2 p^2 \nu_1\nu_2\nu_3\nu_4 \end{aligned} \tag{3.50}$$

---

[7] We could also use this for $D_{-1}(z)$.

where the variables are defined in equation 1.10 in Chapter 1. There are a large number of ways to find roots of a real function, however there is considerably less attention in the literature spent on finding roots in the complex plane. We adopt Muller's method (mentioned in passing in Press et. al., 1992). The idea is that given three initial points in the complex plane, one can find a local interpolatory polynomial. The root of the polynomial can be found as an approximation to the root of the original function. Iteratively, the three points can be updated, the point with the largest corresponding value of the function being discarded. In this way the solution is updated until the magnitude of the function is found to be beneath a threshold value, and we take the final point to be the root. We see that three initial points are needed since we must find a polynomial of minimum degree 2. If it were less, then roots would only be found if they were located along the line in the complex plane joining the points. With three or more, we are able to move around freely in the complex plane. Naturally this is a local method, and assumes that the initial three points are sufficiently close to the true root that the function in the region can be approximated by a second order polynomial. (It is also important that the function itself is smooth near the root). If the initial guesses are not close to the true root, then the polynomial will most probably find a local minimum, and no root will be found. Thus the results are dependent upon finding appropriate starting values for the program. Also, since the function $D(p)$ contains branch cuts, one expects difficulties if branch cuts are close to the desired roots. This is due to the function being discontinuous if we seek roots on a single Riemann sheet. We found that fixing our three points so they all have an identical imaginary part helps with this problem, since then the interpolation never crosses a branch cut (for the branch cuts defined along the real axes). Thus when a new 'zero' is located, we simply take the neighbouring points to the left and right in the complex plane to find the new interpolating polynomial. In our program, we use the regular Lagrange polynomials to interpolate the three points.

3.6 Chapter Summary

We have examined several ways of computing the integrals which provide us with the exact forms of the reflected waves given in Chapter 1. The integrals are of a challenging type, due to the frequency dependence of the exponent. Real axis integration using the Generalized Filon's Method can handle the lowest frequencies best, but still requires intensive sampling at high frequencies. The complex contour method was found to be relatively quick, and very stable at all but the lowest frequencies ($< 1Hz$), and was thus our method of choice throughout the calculations in Chapter 2. It should be noted that the complex contour method did require a detailed knowledge of the pole and branch point locations (the contour needed to be adjusted accordingly) making the real axis integration a simpler method to implement. We have also summarized the techniques used to calculate the special functions needed in Chapters 1 and 2. Finally, we looked at the algorithm used to locate zeros of a function in a complex domain (for our purposes the function was the denominator of our reflection coefficient).

Chapter 4

Edge Diffracted Waves

4.1 Introduction

The lack of a useful description for diffracted waves in Asymptotic Ray Theory (ART) has been a drawback of the method for many years. Keller (1962) originally proposed the geometrical theory of diffraction which corrected some of the shortcomings. However, these diffracted waves depend on a diffraction coefficient (essentially a directivity pattern) which is singular at the shadow boundary, the surface dividing the illuminated and the shadow zones. They also do not rectify the discontinuity in the geometrical wave (the zero order ART solution) located at the shadow boundary. Boundary layer techniques (see for example Zauderer, 1990) can be applied in the narrow region surrounding the shadow boundary. Klem-Musatov (1984) and Bakker (1990) have successfully derived the shadow boundary layer solution for seismic diffracted waves (edge waves) in a convenient, general form to be used in conjunction with ART. Klaeschen et. al. (1994) have developed a scheme to incorporate these diffracted waves into existing automatic ray tracing programs. Any useful diffraction theory must be valid in media with multiple interfaces, yet it has not been shown that the diffracted waves themselves satisfy the the relevant boundary conditions, when using the above mentioned formulae. We shall show that for 2-D inhomogeneous media the boundary conditions *are* actually satisfied, provided the interface is smooth. The application of the theory of edge waves to a particular model can be complex, so we present an example here to examine some of the details. In this way we can appreciate the usefulness of edge waves in models that generate significant diffractions, and also look at some of the limitations of the theory, keeping in mind more general geologic situations.

4.2 Review of Theory

For complete review of ART see, for example, Hron and Kanasewich (1971). Let us represent the zero order ART contribution to a given model as $\mathbf{u} = U_o e^{i\omega\tau}\mathbf{e}$. Here we are working in the frequency domain where the angular frequency is ω and τ is the eikonal which satisfies

$$\nabla\tau \cdot \nabla\tau = \frac{1}{v^2} \tag{4.1}$$

where v is the speed of the isotropic, perfectly elastic medium. U_0 is the geometrical wave amplitude and obeys the transport equation

$$2\nabla\tau \cdot \nabla U_o + U_o\nabla^2\tau = 0. \tag{4.2}$$

Unit vector $\mathbf{e}$ denotes the polarization of the wave displacement; this is parallel to the ray for P-waves and perpendicular for S-waves. If the medium contains interfaces, then the above formulation must satisfy the continuity of stress and displacement across these. When these interfaces are not smooth or two or more interfaces intersect at a point, then discontinuities arise in the zero order solution. The surface defining the discontinuity in U_o is the shadow boundary, and this divides the illuminated and shadow zones (see Figure 4.1). ART is not applicable in the region surrounding the shadow boundary. Klem-Musatov (1984) and later Bakker (1990) have derived a formulation for diffracted waves valid in the vicinity of the shadow boundary, known as the shadow boundary layer. These diffracted waves smooth the discontinuities in zero order ART providing a valid

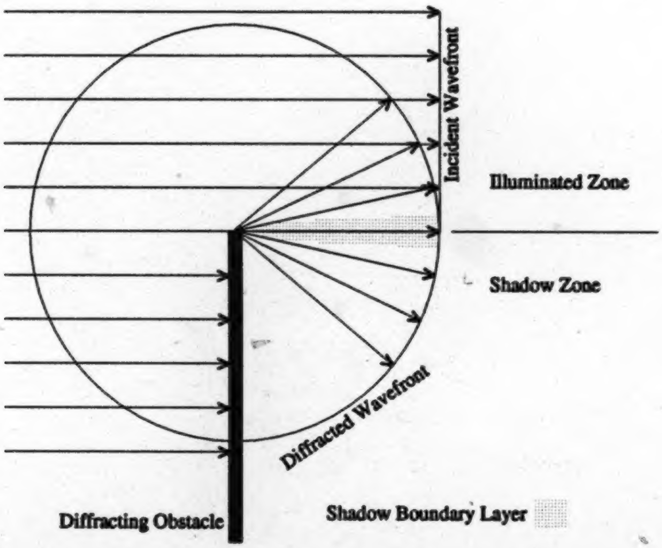
Incident Wavefront
Illuminated Zone
Shadow Zone
Diffracted Wavefront
Diffracting Obstacle
Shadow Boundary Layer

Figure 4.1: An example of the diffraction of a seismic wave. The shadow boundary ray is the ray located at the centre of the shadow boundary layer (shaded). A reflected wave exists (with another shadow boundary layer) but this has not been shown for simplicity.

twice differentiable solution throughout. The formula in the shadow boundary layer is

$$\mathbf{u} = U_o e^{i\omega\tau}\hat{\mathbf{e}} + W(w)\tilde{U}_o e^{i\omega\tau_d}\hat{\mathbf{e}} + O(1/\sqrt{\omega}), \tag{4.3}$$

where τ_d is the diffracted wave eikonal, and

$$W(w) = \pm\frac{1}{2\sqrt{\pi}}\Gamma\left(\frac{1}{2}, -\frac{i\pi w^2}{2}\right)e^{-\frac{i\pi w^2}{2}},$$

where

$$w = \sqrt{\frac{2\omega(\tau_d - \tau)}{\pi}}. \tag{4.4}$$

The incomplete gamma function is represented by $\Gamma(\frac{1}{2}, z)$. The positive and negative signs are for the shadow and illuminated zones respectively. The variable w is a measure of distance from the shadow boundary ($w = 0$); since it is a function of the two eikonals, we must continue the geometrical wave eikonal τ by some method into the shadow zone, as it does not exist there according to the standard ray theory approach. It is worth remarking that the set of all points in space that satisfy $\tau = \tau_d$ defines the shadow boundary; the shadow boundary layer is an asymptotically small region surrounding the shadow boundary ray, and is defined by

$$\omega(\tau - \tau_d) = O(1). \tag{4.5}$$

The factor U_o does not exist in the shadow zone, being abruptly terminated at the shadow boundary, $w = 0$. $\tilde{U}_o$ represents the amplitude continued into the the shadow zone, and is continuous across $w = 0$. Zero order ART has an accuracy of $O(1/\omega)$, however one can see from equation (4.3) that the error is of $O(1/\sqrt{\omega})$. We note in passing that this is the order of magnitude of the diffraction terms resulting from the geometrical theory of diffraction, which are not included in this equation. A graph of equation (4.3) is the solid curve in Figure 4.2, which shows the modulus of the amplitude of **u** using w as the independent variable. This can be contrasted with the dashed curve, which represents the amplitude

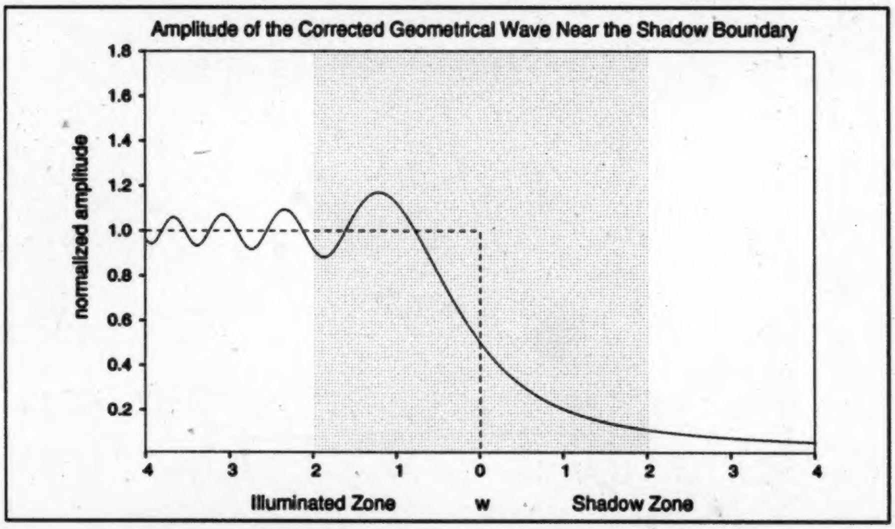

Figure 4.2: Modulus of the normalized geometrical amplitude with diffracted waves included. The dashed line represents the geometrical amplitude without diffracted waves. The shaded area represents the shadow boundary layer, usually taken as $w < 2$.

of the geometrical wave, terminating at the shadow boundary. One can see that the diffracted wave contribution decays with distance from the shadow boundary, and is essentially negligible outside the boundary layer (shaded). The oscillations in the illuminated region are due to the interference between the geometrical and the diffracted waves.

4.2.1 Polarization

The direction of displacement (polarization) of the diffracted wave is parallel to that of the body wave it smooths. However, as Klem-Mustatov (1994) notes, we can actually take the polarization parallel (or perpendicular, if we are dealing with S-waves) to the diffracted ray, as the difference is very small in the shadow boundary layer. We shall outline why this is true. Inside the boundary layer,

$$\tau \approx \tau_d + (1/2)(m - m_d)p^2 \tag{4.6}$$

where p is the distance normal to the shadow boundary, m and m_d are the second partial derivatives in the direction normal to the shadow boundary, and $p = O(1/\sqrt{\omega})$ defines the boundary layer. We can write the gradient of τ and τ_d in ray coordinates, and from equation (4.6) we find that

$$|\nabla\tau - \nabla\tau_d| = O(1/\sqrt{\omega}) \tag{4.7}$$

and hence it follows that

$$|\mathbf{e} - \mathbf{e}_d| = O(1/\sqrt{\omega}). \tag{4.8}$$

This shows that the difference is negligible, since we have an error of $O(1/\sqrt{\omega})$ in the solution anyways. In our numerical example we take the polarization parallel and perpendicular to the diffracted rays for P-waves and S-waves, respectively.

4.2.2 Continuation of the Geometrical Eikonal

We noted before that τ doesn't exist in the shadow zone and must be continued there so we can make use of equation (4.3). One might at first be attracted by the simplicity of a plane wave continuation; however, this leads to significant errors. Technically this is incorrect since it is required that the solution be twice differentiable everywhere, and we can show that a plane continuation of the geometrical eikonal leads to a discontinuity in the first derivative at the shadow boundary. Specifically, for a proper solution we require

$$\left[\frac{\partial \mathbf{u}}{\partial p}\right] = 0 \tag{4.9}$$

where the large brackets denote the jump in the quantity across the shadow boundary, located at $p = 0$. After some expansion using equation (4.3), it becomes clear that this is equivalent to

$$\left[\frac{dW}{d\alpha}\frac{\partial \alpha}{\partial p}\right] = 0 \tag{4.10}$$

where $\alpha = -i\pi w^2/2$. Using a plane wave continuation gives

$$\alpha = \begin{cases} (1/2)i\omega p^2(m - m_d) & \text{in the illuminated zone,} \\ -(1/2)i\omega p^2 m_d & \text{in the shadow zone.} \end{cases} \tag{4.11}$$

Using equation (4.11) combined with the integral definition of the incomplete gamma function in equation (4.4), we quickly find that equation (4.10) is not satisfied for the plane continuation of the geometrical eikonal into the shadow zone. Although the solution itself is still continuous at the shadow boundary and the jump in the derivative may be quite small, the consequence of using a plane continuation of the eikonal turns out to be numerically significant. One can calculate the wave amplitude and compare it to the solution using a properly continued eikonal. The mismatch increases with distance from the shadow boundary, and exceeds 100% within the shadow boundary layer. Therefore the plane continuation of the eikonal is not suitable.

The simplest way to continue the eikonal is using equation (4.6); the wavefront curvature needs to be calculated at each point for the geometrical spreading, so this poses no additional burden. This was the method used in the Numerical Example section.

4.2.3 Continuation of the Geometrical Amplitude

Unlike the geometrical eikonal, a plane wave continuation of this parameter is valid. This is due to the fact that changes in U_o within the shadow boundary layer are of $O(1/\sqrt{\omega})$. Bakker (1990) derived equation (4.3) using the paraxial approximation, where $\tilde{U}_o$ is the amplitude along the central ray, equivalent to a plane continuation of U_o in the shadow boundary layer. What is worth noting is that U_o contains a plane wave reflection/ transmission coefficient for waves having encountered an interface during the course of their propagation. This then means that within the boundary layer differences in geometrical amplitude perpendicular to the shadow boundary are of $O(1/\sqrt{\omega})$, providing the reflection/transmission coefficient is not too rapidly varying (that is, we're not near critical or grazing angles). It can be shown that[1] equation (4.3) satisfies the boundary conditions at a smooth interface to $O(1/\sqrt{\omega})$, when a plane wave continuation of the amplitude is used. If the interface is not smooth, then the edge wave formulation given in equation (4.3) is no longer valid for all the diffracted waves leaving the interface. A particular case of this will be shown in the Numerical Example section.

4.3 Diffracted Waves at Interfaces

Under normal circumstances, boundary conditions are satisfied in ART in the frequency domain by matching terms with corresponding powers of frequency in the ray series on either side of an interface. Such a treatment may be found in Hron and Kanasewich (1971). In the presence of diffractions, **u** is to be specified everywhere to $O(1/\sqrt{\omega})$, so that at an abrupt discontinuity in the elastic parameters of a medium, the diffracted amplitudes must satisfy the relevant boundary conditions to this order of accuracy. Consider the interface shown in Figure 4.3. Naturally the first term of equation (4.3) will satisfy the boundary conditions as has been outlined previously for conventional ART, for example by Červený and

---

[1] This is the subject of the next section.

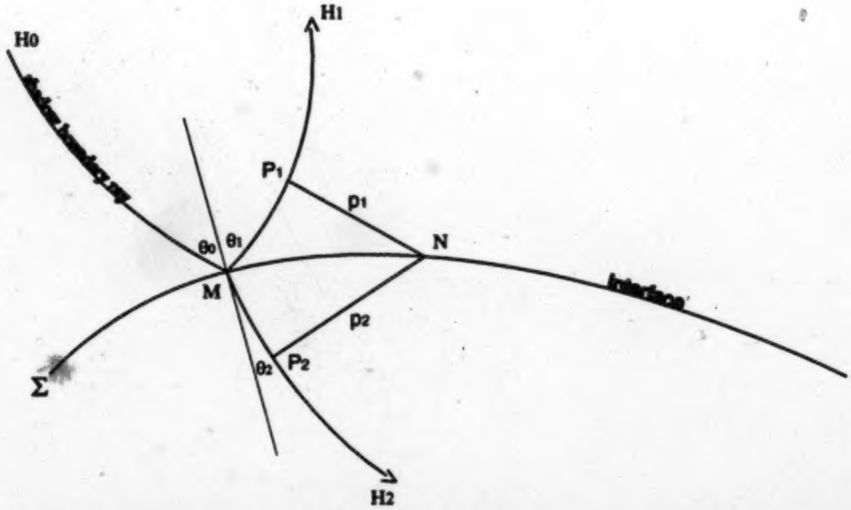

Figure 4.3: Geometry of the smooth interface **Σ** between 2D inhomogeneous media. Symbols $\mathbf{H}_0, \mathbf{H}_1$ and $\mathbf{H}_2$ stand for the paths of the incident, the reflected and the transmitted shadow boundary rays respectively (originating from some previous diffracting obstacle). Point M is the point of incidence of the shadow boundary ray on the interface, and N is a point on the interface lying within the shadow boundary layer. Symbols p_1 and p_2 represent the distances from P_1 and P_2 to N, perpendicular to the respective rays. To avoid clutter, $\mathbf{H}_3, \mathbf{H}_4$ and p_0 have not been depicted.

Ravindra (1971). However, it is not immediately obvious that the second term of equation (4.3) will also satisfy the boundary conditions. Our function $W(w)$ is $O(1)$ only inside the shadow boundary layer, hence this is where we must investigate.

Consider two media separated by an interface, **Σ**. For simplicity we require that the media be isotropic, and contain no inhomogeneity perpendicular to our plane of incidence, making all geometrical and diffracted rays plane curves. The intersection of the plane of incidence with the interface can be expressed as a vector function $\mathbf{\Sigma}(\sigma)$, where σ is arc length measured from point M (See Figure 4.3). The following relationship holds by differentiating the Frenet formulae describing the space curve $\mathbf{\Sigma}(\sigma)$ (see for example Guggenheimer (1977)):

$$\mathbf{\Sigma}(\sigma) = \mathbf{\Sigma}\Big|_M + \mathbf{t}^\sigma_M \sigma + \kappa^\sigma_M \mathbf{n}^\sigma_M \frac{1}{2}\sigma^2 + (\frac{d\kappa^\sigma}{d\sigma}\Big|_M \mathbf{n}^\sigma_M - {\kappa^\sigma_M}^2 \mathbf{t}^\sigma_M)\frac{1}{6}\sigma^3 + \dots \quad , \tag{4.12}$$

where $\mathbf{t}^\sigma$ and $\mathbf{n}^\sigma$ are the unit tangent and normal vectors, respectively, and κ^σ is the curvature. Note that the superscript σ here is a label, and this is true for the superscript h in equation (4.13). At any point along $\mathbf{\Sigma}(\sigma)$, the directions parallel to unit vectors $\mathbf{t}^\sigma, \mathbf{n}^\sigma$ and the binormal $\mathbf{b}^\sigma$ form a local orthogonal coordinate system.

In this Figure 4.3 the shadow boundary ray $(\mathbf{H}_0)$ from some previous unspecified obstacle is incident upon $\mathbf{\Sigma}$. The resulting reflected and transmitted shadow boundary rays are represented by $\mathbf{H}_\nu$ ($\nu = 0, 1, 2, 3, 4$ correspond to the incident (P or S), reflected P, transmitted P, reflected S and transmitted S, respectively). It is unimportant in the following discussion on which side the illuminated and shadow zones are located, the main point being that we are inside the shadow boundary layer. We can expand the rays as a function of the arc length, h_ν, measured from point M:

$$\mathbf{H}_\nu(h_\nu) = \mathbf{H}\Big|_M + \mathbf{t}^h_M h_\nu + \kappa^h_M \mathbf{n}^h_M \frac{1}{2}h_\nu^2 + (\frac{d\kappa^h}{dh_\nu}\Big|_M \mathbf{n}^h_M - {\kappa^h_M}^2 \mathbf{t}^h_M)\frac{1}{6}h_\nu^3 + \dots \quad . \tag{4.13}$$

For notational brevity we have not included a subscript ν on $\mathbf{t}^h, \mathbf{n}^h$ or κ^h, but it should be kept in mind that these quantities are different for each ray. The interface $\mathbf{\Sigma}(\sigma)$ is a welded contact. Let $U^\nu_0 e^{i\omega\tau}\mathbf{e}^\nu$ be the zero order term for the geometrical body wave along the shadow boundary, which at point M satisfies the continuity of stress and displacement boundary conditions. Referring to Figure 4.3, point M is where the shadow boundary ray strikes the interface, and point N lies within the boundary layer. At N we need to satisfy the continuity of displacement for all diffracted waves, so

$$\sum_{\nu=0,1,3} \left(\tilde{U}^\nu_0 W(w^\nu)\right)_j = \sum_{\nu=2,4} \left(\tilde{U}^\nu_0 W(w^\nu)\right)_j \tag{4.14}$$

where subscript j refers to the scalar component of the displacement in the direction specified by the unit vectors of tangent, normal and binormal to Σ at N. The equation to be satisfied for continuity of stress at N is:[2]

$$\sum_{\nu=0,1,3} \lambda_1 \delta_{nj} \left(\tilde{U}_0^\nu W(w^\nu)\right)_i \frac{\partial \tau_d}{\partial x_i} + \mu_1 \left(\frac{\partial \tau_d}{\partial x_j} \left(\tilde{U}_0^\nu W(w^\nu)\right)_n + \frac{\partial \tau_d}{\partial x_n} \left(\tilde{U}_0^\nu W(w^\nu)\right)_j \right)$$
$$= \sum_{\nu=2,4} \lambda_2 \delta_{nj} \left(\tilde{U}_0^\nu W(w^\nu)\right)_i \frac{\partial \tau_d}{\partial x_i} + \mu_2 \left(\frac{\partial \tau_d}{\partial x_j} \left(\tilde{U}_0^\nu W(w^\nu)\right)_n + \frac{\partial \tau_d}{\partial x_n} \left(\tilde{U}_0^\nu W(w^\nu)\right)_j \right), \tag{4.15}$$

where subscripts 1 and 2 differentiate between elastic parameters on each side of the boundary (1 is the medium containing the incident ray) and subscript n refers to the direction normal to the boundary. We are using the Einstein summation convention for the subscript i. First we need to examine $W(w^\nu)$. To expand $W(w^\nu)$ at point N we see from equation (4.4) that w^ν depends on the travel times τ and τ^d, which can be approximated in the boundary layer using equation (4.6). This means finding expressions for both m and m^d at point P_ν (see Figure 4.3), as well as relating the distance p_ν to the arc length along the interface. Using equations (4.6), (4.12), and (4.13) and assuming small h_ν and σ, one can find that to leading order

$$p_\nu \approx (\kappa_P^h / \kappa_M^h) \cos\theta_\nu \sigma \approx (\kappa_P^h / \kappa_M^h) \cot\theta_\nu h_\nu. \tag{4.16}$$

Next, along each of the rays $\mathbf{H}_\nu$ both m and m_d obey the Ricatti equation

$$\frac{dm}{dh} + vm^2 + v_{,pp} v^{-2} = 0, \tag{4.17}$$

derived by Červený and Hron (1980). Hence

$$(m - m_d)_\nu \Big|_{P_\nu} = (m - m_d)_\nu \Big|_M + \xi_\nu \quad , \tag{4.18}$$

where

$$\xi_\nu = \int_M^{P_\nu} v(m^2 - m_d{}^2)_\nu dh_\nu \tag{4.19}$$

---

[2] It can be shown that we are using the leading (asymptotically largest) term for the traction. We also are using fixed cartesian coordinates, which is possible due to the 'principal of locality' (see C& R for details).

and $(m - m_d)_\nu\big|_M$ are proportional to the post reflection/transmission wavefront curvatures at point M. Clearly,

$$|\xi_\nu| \le |(m^2 - {m_d}^2)_\nu|_M v^* h_\nu \tag{4.20}$$

with v^* representing the maximum velocity on the ray segment MP_ν, the length of the latter being h_ν. Next, to elicit a common factor from the wavefront curvatures above, we make use of

$$\nabla^2\tau = \frac{1}{v}\frac{d}{ds}\left(\frac{1}{v}\right) + \frac{1}{v}\left(\frac{1}{r_1} + \frac{1}{r_2}\right) \tag{4.21}$$

where s is the distance along a given ray, and $r_{1,2}$ are the principal curvatures of the wavefront, and then the Gel'chinsky formula (Gel'chinsky, 1961). The latter describes the change in the radius of curvature of a wavefront after encountering the interface at M. If r_0 and r_ν are the radii of curvature of the wavefront in the plane of incidence before and after reflection/transmission respectively, $l_{1\nu}$ is the direction tangent to the wavefront at M in the plane of incidence and l_2 is the direction tangent to the interface at M in the plane of incidence, then for the situation we are considering the Gel'chinsky formula reads

$$\begin{aligned}\frac{1}{r_\nu} = \frac{1}{r_0}\frac{v_\nu \cos^2\theta_0}{v_0\cos^2\theta_\nu} + \frac{\kappa_M^\sigma}{\cos^2\theta_\nu}(v_\nu/v_0\cos\theta_0 \pm \cos\theta_\nu)\\ + \frac{\tan\theta_\nu}{v_\nu}\frac{\partial v_\nu}{\partial l_{1\nu}} + \frac{\sin\theta_0}{\cos^2\theta_\nu}\frac{\partial(v_\nu/v_0)}{\partial l_2} - \frac{v_\nu \sin 2\theta_0}{2v_0^2\cos\theta_\nu}\frac{\partial v_0}{\partial l_{10}}, \quad \nu \neq 0.\end{aligned} \tag{4.22}$$

The upper and lower signs correspond to to the reflected and transmitted waves respectively. Note that there is only one term in equation (4.22) that contains the radius of curvature of the wavefront prior to its reflection/transmission, and that the directions $l_{1\nu}$ are identical for the geometrical body wave and the diffracted wave since point M lies on shadow boundary. Combining equations (4.6), (4.21), (4.16), (4.18) and (4.22) we obtain

$$\begin{aligned} i\omega(\tau - \tau_d)_\nu &= i\omega\sigma^2\left(\frac{\kappa_N^h}{\kappa_M^h}\right)^2 \frac{\cos^2\theta_0}{2v_0}\bigg|_M \left(1/r_0\big|_M - 1/r_{d_0}\big|_M + \xi_\nu\frac{v_0\cos^2\theta_\nu}{\cos^2\theta_0}\right) + O(\sigma^3)\\ &= \alpha + \beta_\nu \end{aligned} \tag{4.23}$$

where α is common to all waves at the interface, and β_ν is not. From equation (4.16) we can see that $\dot{h}_\nu$ and σ are $O(1/\sqrt{\omega})$ provided $\cos\theta_\nu = O(1)$,[3] ie. θ_0 is not near the critical angle. This further implies that

$$\alpha = O(1) \qquad \text{and} \qquad \beta_\nu = O(1/\sqrt{\omega}) \tag{4.24}$$

provided κ_P^h/κ_M^h is $O(1)$. Appendix C shows that this situation results in

$$W(w^\nu)/W(w^0) = 1 + O(1/\sqrt{\omega}). \tag{4.25}$$

This simplifies equations (4.14) and (4.15), since the term $W(w^\nu)$ cancels from both sides, leaving residuals of $O(1/\sqrt{\omega})$. Therefore we are left to deal with the amplitude term $\tilde{U}_0^\nu$. It is worthwhile re-emphasizing that this holds while the incident boundary ray does not approach a critical angle. It can easily be shown, using the approximations already presented, that inside the boundary layer $\tilde{U}_0^\nu$ can be approximated by the body wave amplitude calculated at point M. This then satisfies equations (4.14) and (4.15) to $O(1/\sqrt{\omega})$.

While this accounts for the majority of cases, it is conceivable that the boundary layer will intersect an interface that is not smooth during the course of its propagation through diffracting media. Indeed, the ray tracing scheme of Klaeschen et al. (1994) encounters this situation in the first example of their paper. When this happens, the arguments presented in this section become invalid.

4.3.1 Interface Complications

When the interface is not smooth, we can no longer use the previous section's approximations. Consider Figure 4.4, an identical model to that in Figure 4.3, except that there exists a discontinuity in the tangential derivative of $\Sigma(\sigma)$ at point Q. We previously showed that for a smooth interface, $W(w^\nu)$ is identical to

---

[3] This is a bit vague; we really just mean that the shadow boundary layer must not intersect the interface more than a few multiples of $1/\sqrt{\lambda}$ away from the point of incidence of the shadow boundary ray (λ=wavelength).

$W(w^0)$ to $O(1/\sqrt{\omega})$ at point N (equation (4.25)). However, in the present case the discontinuity at Q invalidates the approximation in equation (4.16). Hence neither σ nor h_ν can be shown to be $O(1/\sqrt{\omega})$, implying $i\omega(\tau - \tau_d)_\nu$ and thus $W(w^\nu)$ are distinct at N for all ν. Therefore the boundary conditions will not be satisfied using conventional diffraction terms for the case depicted in Figure 4.4. We have assumed that the reflected and transmitted diffracted waves leaving the interface to the right of Q in Figure 4.4 have the form given in equation (4.3). Below we explain why this is not appropriate. The amplitude of a diffracted wave in the boundary layer is tied to the amplitude of the geometrical wave, through the factor $\tilde{U}_o$ in equation (4.3). This link is attributed to the diffusion of energy from the illuminated zone to the shadow zone across the shadow boundary (Klem-Musatov, 1994). Outside the boundary layer the geometrical theory of diffraction applies (Keller, 1962) and energy is transported parallel to the diffracted rays. With the presence of interface complications, the point Q in Figure 4.4 becomes

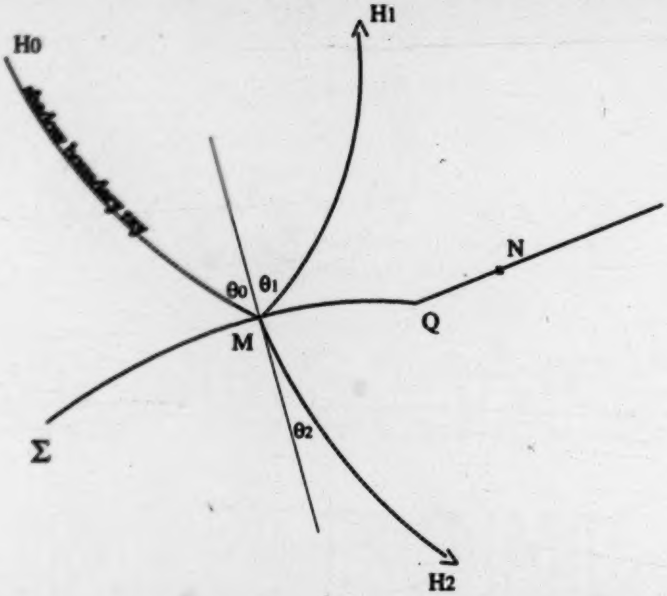

Figure 4.4: Geometry of the interface Σ with discontinuous tangential derivative at point Q. In all other respects this model is identical to that in Figure 4.3.

the source of secondary diffracted waves, which smooth the discontinuity of the reflected and transmitted primary diffracted waves leaving the interface to the left of point Q. These secondary diffracted waves now account for the energy being diffused from the illuminated zone to the shadow zone. We must conclude that after reflection/transmission, the primary diffracted waves leaving the interface to the right of point Q no longer receive energy diffused from the illuminated zone, and hence cannot have the form given in equation (4.3).

4.4 Numerical Example: The Amoco Model

The example we present employs the Amoco model used earlier by Hron and Chan (1994), who studied SH diffracted waves. It is a simplified version of a tar sands deposit in northern Alberta, which was used by Amoco researchers to determine the experimental and theoretical role of diffracted waves in field records (Hron and Covey, 1988). Here we investigate the P-SV case rather than the SH case. The model itself (Figure 4.5) is two dimensional and is composed of a box shaped low velocity zone embedded in a constant velocity layer between two half spaces. The vertical component receivers and the impulsive source are buried to avoid free surface effects. The ratio of P-wave to S-wave speeds is $\sqrt{3}$. The source wavelet is described by:

$$f(t) = A\sin(2\pi t)e^{-\left(\frac{\pi}{2}t\right)^2} \tag{4.26}$$

where A is constant. Multiples and head waves were not calculated in the seismograms. Figure 4.6 (top) contains the zero order ART results for this model. There are 12 geometrical body waves calculated here (each with a different type of raypath), and the dominant six are labelled. Figure 4.7 contains the ray diagrams corresponding to these arrivals. Many discontinuities are present in Figure 4.6 (top), and it is clear that standard ART provides a very unsatisfactory solution. The wavefield with diffractions included (Figure 4.6, bottom) has all discontinuities smoothed using 30 unique diffracted wave contributions (each one is defined by the geometrical body wave discontinuity it smooths). The advantage of the Amoco model is that it presents several different cases of diffraction and we can use these to study the application of diffracted waves. We shall look at two arrivals in a detailed manner.

The first is a P-wave reflection from interface L2, labelled (2) in Figure 4.6. The

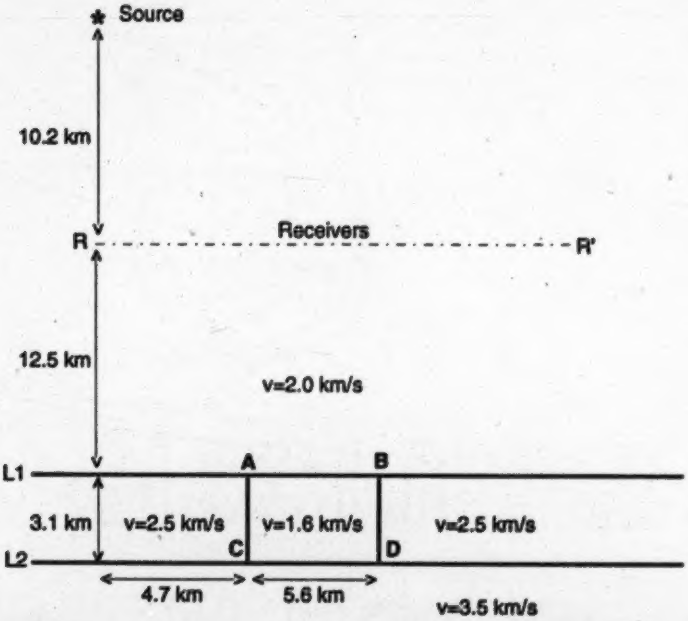

Figure 4.5: The so called Amoco model used for computation of synthetic seismograms. The vertical axis is depth and densities are equal to unity everywhere. The speeds indicated are for P-waves. The line RR' represents 60 equally spaced vertical displacement geophones.

geometrical rays (Figure 4.7) are completely truncated by the vertical interfaces AC and BD. The corner which terminates the reflections (A or B) gives rise to diffracted waves which smooth the transition from the presence to the absence of a reflection. The geometrical eikonal and amplitude are discontinuous across the shadow boundary, which divides the illuminated and shadow zones. The shadow boundary is represented by the last ray in the geometrical set of rays which approach the diffracting corner from a particular direction. In Figure 4.8 (bottom) we see the effect of adding the diffracted waves (labelled 2a) generated when the shadow boundary ray is the last geometrical ray whose path lies to the left of the vertical interface. Figure 4.8 (top) is a ray diagram illustrating this. The geometrical reflection is still incomplete, and more diffracted waves are needed. The last geometrical ray lying to the right of the vertical boundary (top of Figure 4.9) is a shadow boundary ray, and when we include the diffractions caused by it (labelled 2b) the zero order approximation reflection becomes nearly complete (bottom of Figure 4.9). There still exists a small discontinuity in the wavefield, located around 23 seconds at an offset of 4.7 km. It is here that the diffracted waves (2b) are themselves truncated by the vertical interface AC. We can introduce secondary diffracted waves at point A corresponding to the rays in Figure 4.10 (top) to smooth this. The shadow boundary ray in this case is a primary diffracted ray that travels vertically down from the point of diffraction (A), reflects at the interface L2 and travels upwards striking point A again causing secondary diffracted waves. The result is shown in Figure 4.10 (bottom) and labelled (2c). Although these particular secondary diffracted waves seem to complete the wavefield adequately, we expect some additional error has been introduced. This is because the shadow boundary ray travels along the interface AC, and boundary conditions are not satisfied here without the presence of another wave travelling along the left side of AC. In our numerical example this is a relatively small defect, since the amplitude along the boundary ray in Figure 4.10 is low (it is near the edge of the shadow boundary layer). However, this represents one of the limits from the theory of edge waves; specifically, when an interface runs nearly parallel to a shadow boundary ray, boundary conditions are not satisfied and equation (4.3) is not correct to $O(1/\sqrt{\omega})$. (Equation (4.3) gives the formula for geometric and diffracted waves in the boundary layer).

The second case we shall consider is the P-wave reflection from the top interface

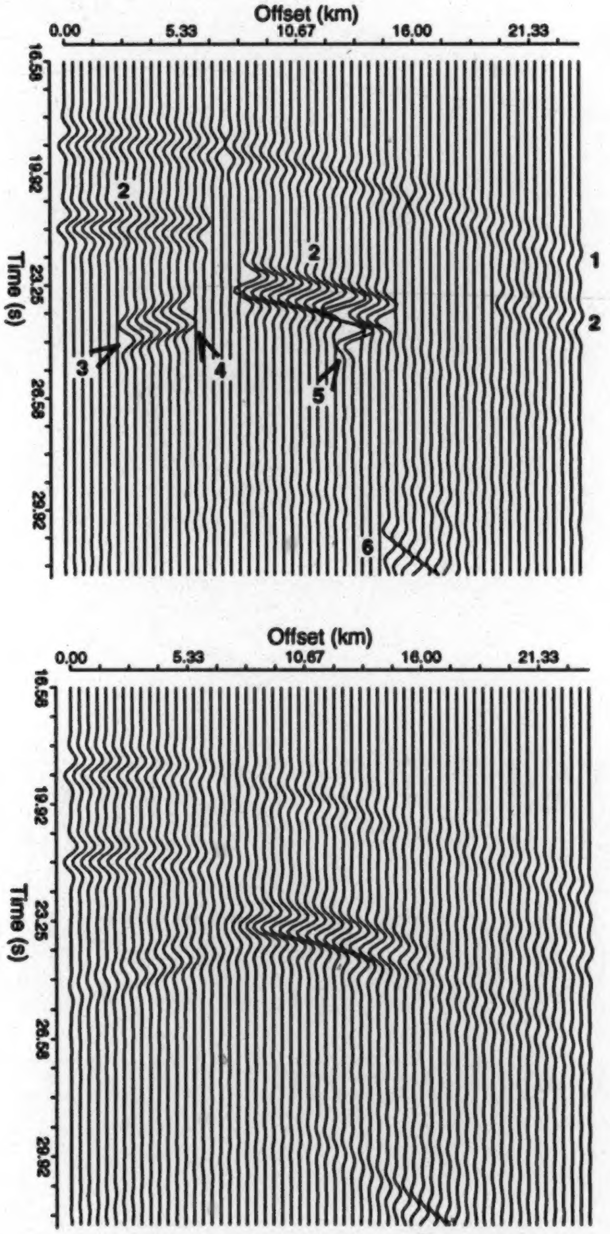

Figure 4.6: (top) The zero order ART response to the Amoco model. No multiples or diffractions are included. The six largest contributions are labelled here and described in the text. Their raypaths (using corresponding labels) can be found in Figure 4.7. (bottom) The zero order ART solution to the Amoco model with diffracted waves included.

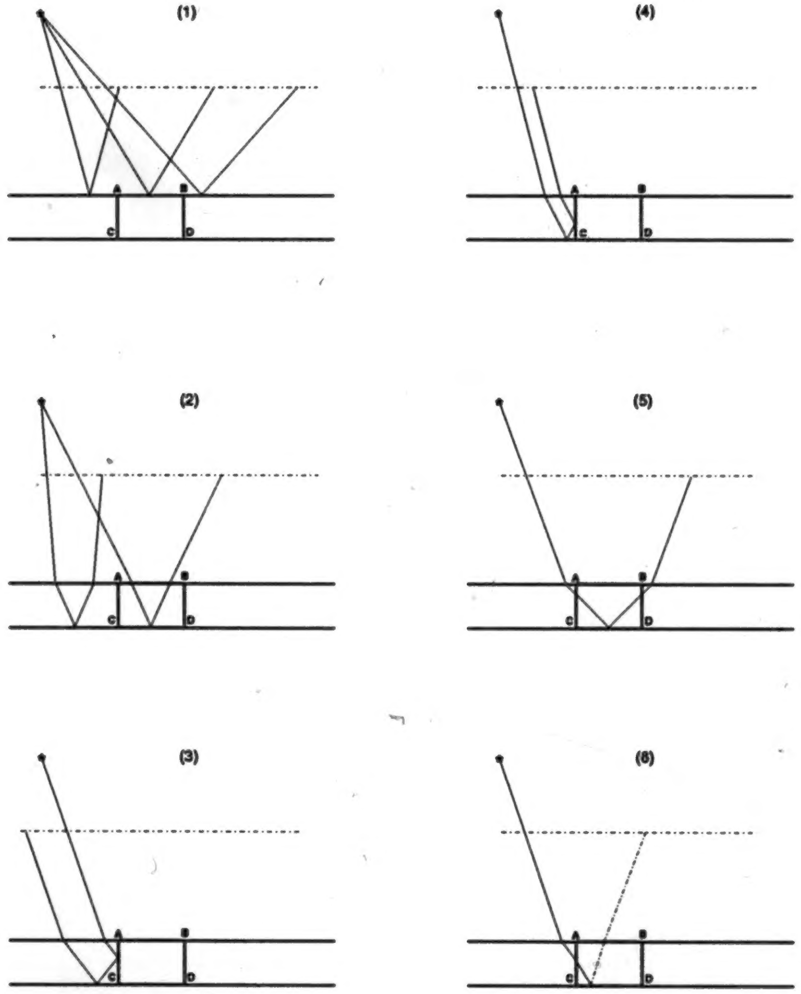

Figure 4.7: Ray diagrams containing sample rays for the six dominant arrivals of zero order ART for the time frame shown in Figure 4.6. Diagrams are not to scale. All arrivals are P-waves except (6), where the dashed ray segment indicates conversion to an S-wave. The numbers shown correspond to the labels in Figure 4.6.

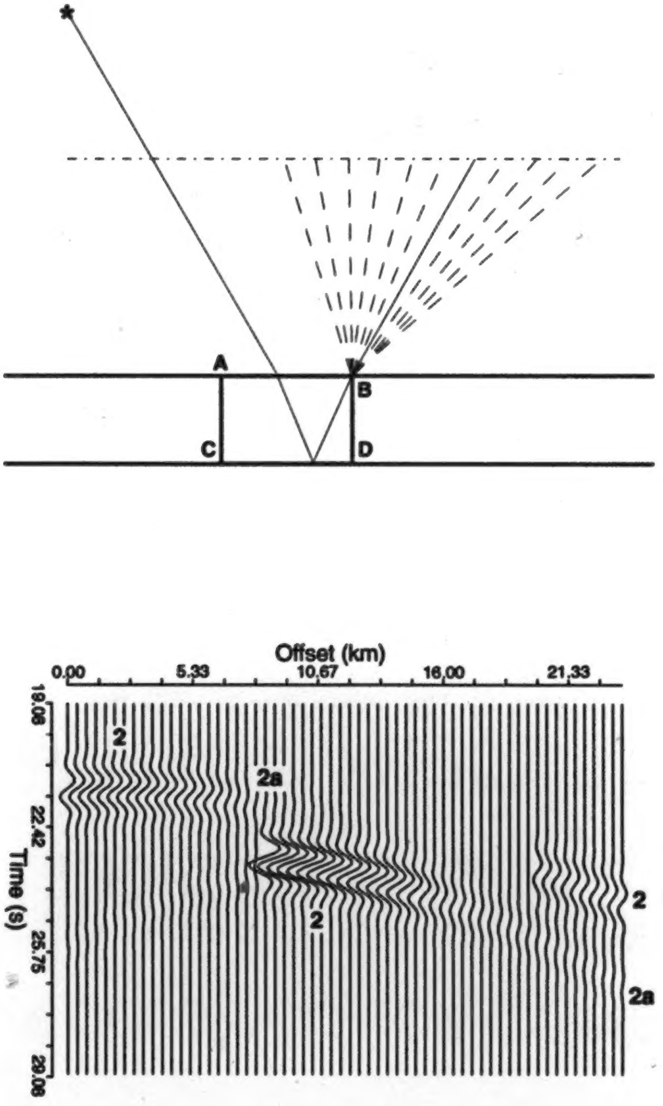
A
B
C
D
Offset (km)
0.00
5.33
10.67
16.00
21.33
Time (s)
19.08
22.42
25.75
29.08
2
2a
2
2
2a

Figure 4.8: (top) Ray diagram (not to scale) showing the diffracted rays (dashed) from point B that smooth arrival (2), the P-wave reflection from the bottom interface (L2). The boundary ray is shown as the solid line. Note that diffractions of the same type occur at corner A. (bottom) Seismograms of the geometrical arrival (2) with diffracted waves from corners A and B, labelled (2a).

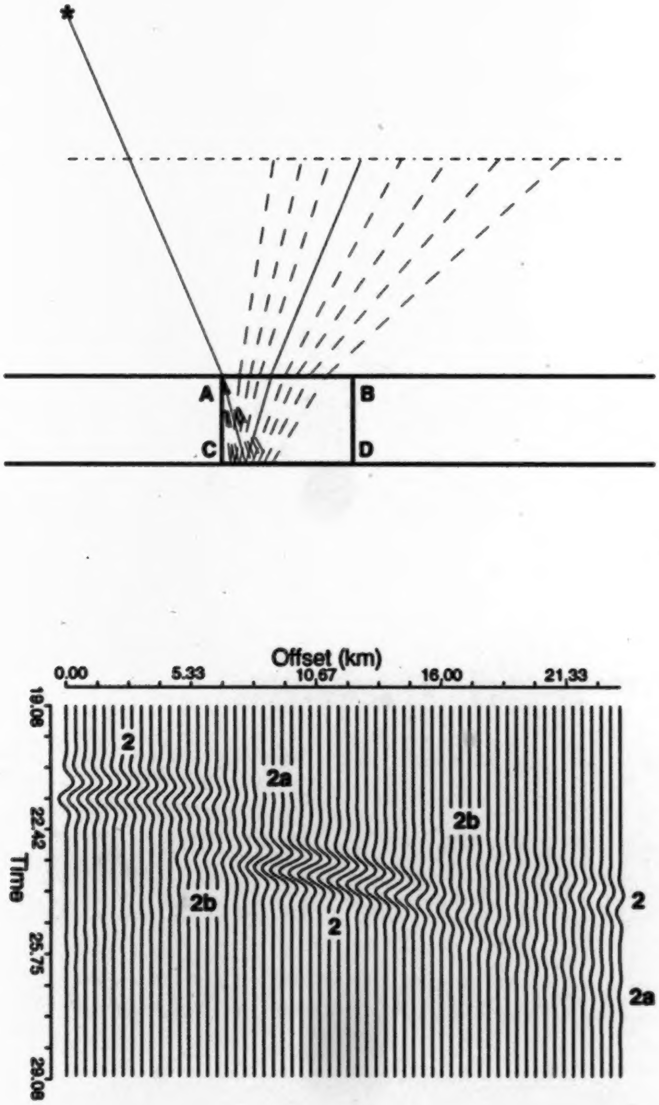

Figure 4.9: (top) A ray diagram for the diffracted waves (dashed) originating at point A that smooth arrival (2). The boundary ray is shown as the solid line. Similar diffractions originate at corner B. (bottom) Seismograms of the geometrical arrival including the diffracted wave (2a) and the above type of diffracted wave, labelled (2b).

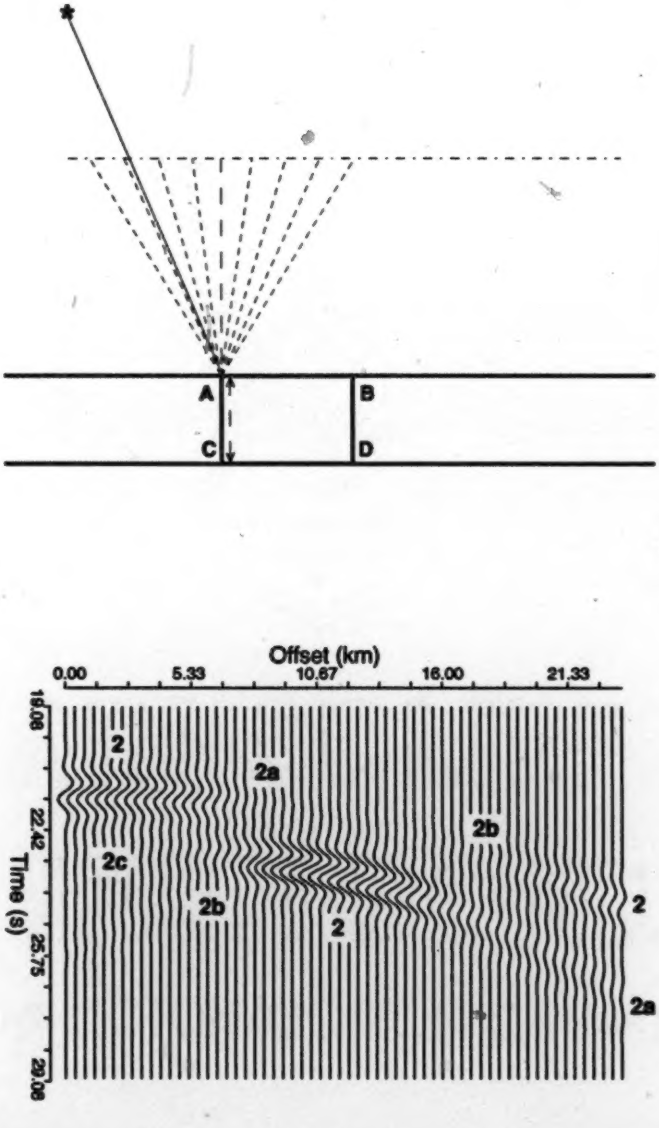
A
B
C
D
Offset (km)
0.00
5.33
10.67
16.00
21.33
Time (s)
19.08
22.42
25.75
29.08
2
2a
2b
2c
2b
2
2
2a

Figure 4.10: (top) Ray diagram of doubly diffracted waves. The geometrical ray (solid) is diffracted at point A and travels vertically downwards (long dash). It then reflects at the bottom interface, travels upwards to point A creating secondary diffracted rays (short dash). (bottom) Seismograms including the geometrical wave (2), diffracted waves (2a) and (2b) and the above doubly diffracted wave, labelled (2c).

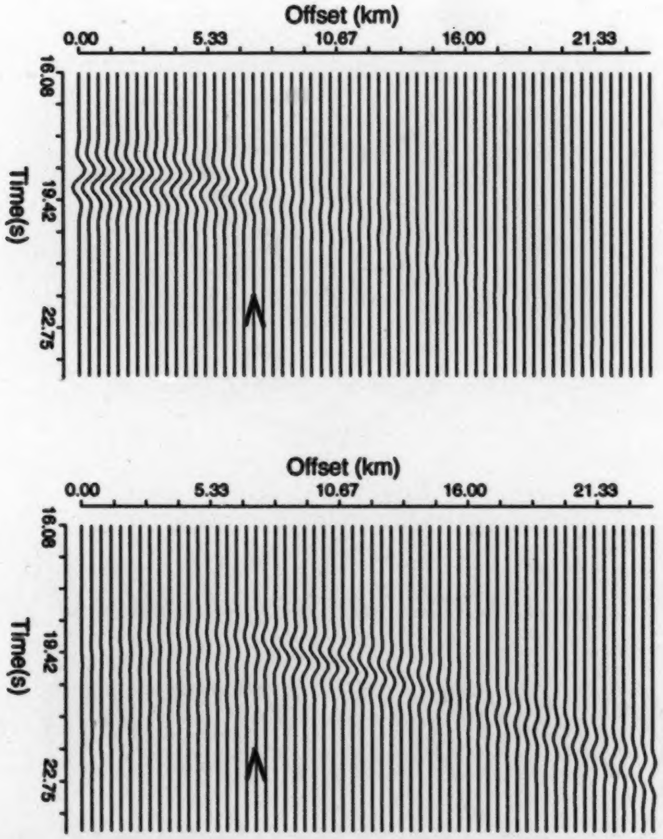

Figure 4.11: (top) Seismograms of the geometrical arrival (1), the P-wave reflection from the top interface (L1), for the group of rays reflecting to the left of point A. Included are diffracted waves from A which smooth this arrival and decay to the right (the shadow zone for this group). (bottom) Seismograms of the geometrical arrival (1), for the rays reflecting to the right of point A including the diffracted waves from point A which smooth this arrival and decay to the left (into the shadow zone for this group). (Diffracted waves from point B have been used to make the bottom seismograms fully continuous.) The arrows indicate the position of the shadow boundary being examined.

L1 (labelled (1) in Figure 4.6). The shadow boundaries are defined by the rays reflecting from interface L1 at the points A and B. Unlike reflection (2), across the shadow boundaries the eikonal for reflection (1) is continuous and the amplitude of the wave wave doesn't vanish (it changes amplitude according to its reflection coefficient). The solution offered by equation (4.3) decays to zero in the shadow zone (see Figure 4.2), where no geometrical wave exists. In Figure 4.6 we see that a geometrical wave is present on both sides of the shadow boundary, the latter being visible in the seismograms where there is a reversal of polarity in the reflection. Hence to use equation (4.3) we need to break up the reflection into reflected ray groups lying to the left and right of each corner. Each of the two groups is defined by the continuity of its reflection coefficient. Kinematically each group is identical at the shadow boundary, leading to a continuous eikonal. Focussing on corner A (which produces the leftmost discontinuity in reflection (1) in Figure 4.6), we can use equation(4.3) by first making $\tilde{U}_o$ the geometrical amplitude associated with the rays reflecting from interface L1 to the left of point A. The diffracted amplitude decays in the shadow zone to the right of the shadow boundary ray (Figure 4.11, top). Similarly, for the other diffracted wave we make $\tilde{U}_o$ the geometrical amplitude associated with the rays reflecting to the right of point A (see Figure 4.11, bottom). We can now appeal to the principal of superposition and combine the two as shown in Figure 4.6 (bottom), where there is a smooth transition from one reflection coefficient to another across the shadow boundary. In our model the change in polarity emphasizes this transition.

The previous two examples demonstrate that the presence of diffracted waves can be identified by sharp changes in geometrical wave amplitude or travel time. This fact was recognized by Klaeschen et. al. (1994), and used in their automated 2-D ray tracing scheme which augmented standard ray theory with diffracted waves.

4.4.1 Interface Complications

The model we have used contains no significant interface complications as defined in the previous sections. However, we can adjust the model to consider how these complications might arise. Consider the shadow boundary shown in Figure 4.9, which is due to the reflected P-wave from interface L2. If we move the vertical interface BD closer to AC the result would look like the situation in Figure 4.12. The shaded area represents the boundary layer, where the diffracted waves are of significant amplitude. The model without adjustment had no diffracted rays in the boundary layer intersecting BD. One can see that for the rays intersecting the vertical interface BD the amplitude cannot be continued from the shadow boundary ray (the solid ray in Figure 4.12) as they have, for example, very different reflection transmission coefficients if boundary conditions are to be satisfied on BD. Also the description of diffracted waves given by equation (4.3) is no longer valid for the primary diffracted rays passing through BD, once they have transmitted through the top (L1) interface. The secondary diffracted waves from point B smooth the discontinuity in the primary diffracted waves that transmit through L1 to the left of B; hence the primary diffracted waves that transmit to the right of B no longer smooth any discontinuity, and cannot be represented by the form given in equation (4.3).

4.5 Chapter Summary

We have summarized the theory of edge-diffracted waves as set out by Klem-Musatov (1984). In so doing we focussed on several points of practical interest for implementing these diffracted waves: the polarization of the diffracted wave, the continuation of eikonal and the continuation of the geometrical amplitude into the shadow zone. The problem as to whether the diffracted waves satisfy boundary conditions when crossing further interfaces (in the formulation of Klem-Musatov,

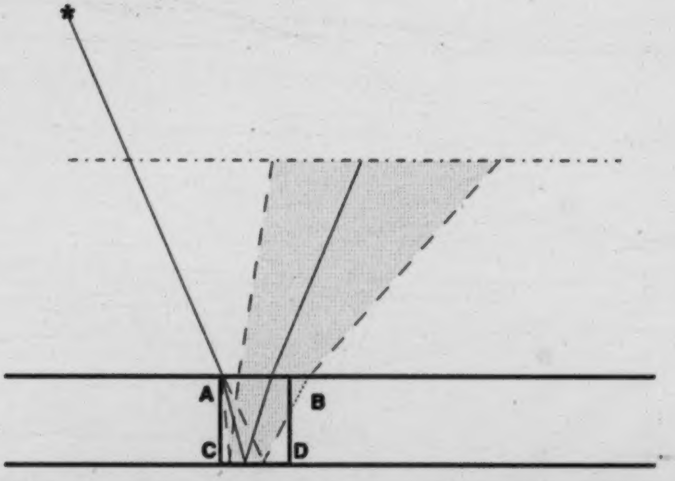

Figure 4.12: A ray diagram illustrating where boundary complications might arise. Interface BD has been moved to the left to intersect the boundary layer (shaded) caused by the diffraction of waves at point A. The solid ray represents the shadow boundary ray.

1984) was addressed. It was found that boundary conditions are indeed satisfied, so long as 1) the interface is smooth within the shadow boundary layer and 2) the shadow boundary ray is not close to the critical angle. We ended up by looking in detailed at the use of edge waves on the Amoco model, which consists of many subsurface edges (truncated layers). This highlighted how modelling P and and SV waves using zero order ART can benefit from the inclusion of edge diffracted waves, which smooth the wavefield. In practice one would need to derive an automatic scheme for such calculations, as has been done by Klaeschen et. al. (1994). Any such algorithm must encompass the steps carried out in detail on the Amoco model, while also alerting the user of potential violations in boundary conditions (where amplitudes would be unreliable).

Conclusions

This body of work has focussed on two areas of seismology in which standard Asymptotic Ray Theory fails: incorporating diffracted waves, and zones of interference between head, reflected and leaky waves. We have derived local formulae that correctly describe the interference of any of the above waves when our medium is rather ideal: layers are both homogeneous and isotropic, and interfaces are plane. We have also explored the size of the regions throughout which interference arises. More general formulae have been derived by Thomson (1990) which account for curved interfaces and inhomogeneous media, but only for the acoustic waves, which lack the complexity of elastic waves. Therefore this work is important for several reasons: i) it explains the complications involved when dealing with seismic waves reflected near critical angles, which should be useful when deriving more complex formulae involving inhomogneous media with curved interfaces, ii) it provides a rapid way of computing partial wavefields (corresponding to rays) when the assumption of homogeneous layers *is* valid, and iii) it completes the theory surrounding Cagniard's Problem of classical seismology, when using frequency domain methods of analysis. While reflection seismograms have been calculated quite accurately using the Cagniard-de Hoop method (see Aki and Richards, 1980), it fails to take advantage of possible asymptotic approximations making it less efficient than frequency domain methods.

Future work should include looking into exact transformations of the special functions used in our asymptotic (non-uniform) formulae into the time domain. This would enable us to use a simple convolution operator in the time domain when we are modelling the interference between waves. This should be contrasted with the present situation where the solution must be calculated for each frequency, and then an inverse Fourier Transform is performed.

The use of diffracted waves has been shown to be very useful when confronted with a model containing discontinuous interfaces. We have looked at relatively simple media, but the theory of edge diffracted waves (derived by K.M. Klem-Musatov, 1984) is actually much more general. To be useful one needs to incorporate the theory of edge waves with zero order Asymptotic ray Theory in an automatic fashion, and studying the Amoco model provided us with insights that can be (in the future) used to this end. We have also provided proof that the diffracted waves given by Klem-Musatov actually satisfy boundary conditions when crossing additional interfaces, provided that the interface is smooth and that there is no critical refraction. This is really an important point in the theory that has been assumed to be true, until now.

Appendix A

Proof that Truncation of the Steepest Descents Contour Introduces Asymptotically Small Errors

Let

$$I = \int_{C_s} f(p)e^{\omega\phi(p)}\,dp \tag{A.1}$$

Then if $\tilde{C}_s$ is the truncated contour,

$$I = \int_{\tilde{C}_s} + \int_{C_s - \tilde{C}_s} = \tilde{I} + E_T. \tag{A.2}$$

Claim 2

$$I \sim \int_{\tilde{C}_s} f(p)e^{\omega\phi(p)}\,dp, \qquad \omega \to \infty. \tag{A.3}$$

Proof 2 *Thus we must show that*

$$\left|\frac{E_T}{\tilde{I}}\right| = \left|\frac{\int_{C_s - \tilde{C}_s} f(p)e^{\omega\phi(p)}\,dp}{\int_{\tilde{C}_s} f(p)e^{\omega\phi(p)}\,dp}\right| \to 0, \qquad \omega \to \infty. \tag{A.4}$$

Let's use the transformation

$$\phi(p) = \phi(p_0) - t, \qquad \frac{dp}{dt} = \frac{-1}{\phi'(p)} \tag{A.5}$$

which clearly puts $t \in \Re^+$. *Thus,*

$$E_T = e^{\omega\phi(p_0)} \int_T^{+\infty} g(t)e^{-\omega t}\,dt \tag{A.6}$$

and

$$\tilde{I} = e^{\omega\phi(p_0)} \int_0^T g(t)e^{-\omega t}\,dt \tag{A.7}$$

where $g(t) = f(p)dp/dt$ and T is the endpoint of the truncated contour. Next, let us assume bounds on the $g(t)$, which contains no exponential terms or singularities along it, save at $t = 0$:

$$|g(t)| \leq e^{at}, \qquad t \geq T, \tag{A.8}$$

where a is a frequency independent constant. We may therefore write

$$|E_T| \leq |e^{\omega\phi(p_0)} \int_T^{\infty} e^{a-\omega t}\, dt| \tag{A.9}$$

$$= \left| e^{\omega\phi(p_0)} \frac{e^{a-\omega T}}{\omega - a} \right|. \tag{A.10}$$

Next we may invoke Watson's lemma upon $\tilde{I}$ (Bender and Orszag, 1978) which states that provided we can represent $g(t)$ by

$$g(t) \sim t^{\alpha} \sum_{n=0}^{\infty} a_n t^{\beta n} \tag{A.11}$$

then

$$\tilde{I} \sim e^{\omega\phi(p_0)} \sum_{n=0}^{\infty} \frac{a_n \Gamma(\alpha + \beta n + 1)}{\omega^{\alpha+\beta n+1}}. \tag{A.12}$$

We can assume the form given in equation (A.11) since the singularity at $t = 0$, arising from dp/dt, is integrable (proportional to $t^{-1/2}$). We may now write

$$\left|\frac{E_T}{\tilde{I}}\right| = O(\omega^{\alpha} e^{-\omega T}) \to 0, \qquad \omega \to \infty. \tag{A.13}$$

Thus our error is asymptotically negligible, so long as we choose T to be non-zero and frequency independent. However, we are restricted by the next step in the asymptotic analysis, which is to approximate the exponent by the first two terms of its Taylor expansion about the saddle point. We require then that $p_T = p(t = T)$ be sufficiently close to the saddle p_0 so that this replacement generates errors that are asymptotically negligible. This presents a frequency dependent upper bound on the size of T. (A variation of the following argument can be found in Bender and Orszag, 1978). Thus the two competing conditions we want to satisfy are:

$$\begin{cases} (A) & \omega Re\{\phi(p_0) - \phi(p_T)\} = \text{asymptotically large} \\ (B) & \omega[\phi(p_T) - \phi(p_0) - (1/2)\phi''(p_0)(p_T - p_0)^2] = \text{asymptotically small} \end{cases}$$

If we let $p_T - p_0 = O(\omega^q)$ *then (B) gives us the relation (using the next higher term in the Taylor series)*

$$1 + 3q < 0 \tag{A.14}$$

and condition (A) gives us

$$1 + 2q > 0, \tag{A.15}$$

leaving us with

$$-1/2 < q < -1/3. \tag{A.16}$$

The two conditions are compatible, and T *can be found such that equation (A.13) is asymptotically negligible:*

$$T = O(\omega^{2q}), \qquad -1/2 < q < -1/3. \tag{A.17}$$

Therefore we have found that the contour can be truncated and that the exponent can be replaced by its two term Taylor expansion, only introducing asymptotically negligible errors into the solution. □

Appendix B

Proof of Asymptotic Nature of Approximation

Claim 1 *An asymptotic sequence of functions can be found for the case involving a pole-saddle-branch point in proximity,*

$$\begin{aligned}\Phi_0 &= a_{00}\int_{C_s}\frac{1}{p-p_L}e^{\omega\phi(p)}\,dp + a_{10}\int_{C_s}e^{\omega\phi(p)}\,dp \\ &\quad + b_{00}\int_{C_s}\frac{\sqrt{p_b-p}}{p-p_L}e^{\omega\phi(p)}\,dp + b_{10}\int_{C_s}(p_b-p)^{1/2}e^{\omega\phi(p)}\,dp \\ &\quad + b_{20}\int_{C_s}(p_b-p)^{3/2}e^{\omega\phi(p)}\,dp \end{aligned} \tag{B.1}$$

and

$$\begin{aligned}\Phi_j &= \frac{a_{1j}}{\omega^j}\int_{C_s}e^{\omega\phi(p)}\,dp + \frac{b_{1j}}{\omega^j}\int_{C_s}(p_b-p)^{1/2}e^{\omega\phi(p)}\,dp \\ &\quad + \frac{b_{2j}}{\omega^j}\int_{C_s}(p_b-p)^{3/2}e^{\omega\phi(p)}\,dp \qquad j \geq 1\end{aligned} \tag{B.2}$$

and we claim that[1]

$$u_z^{ref} \sim \sum_{n=0}^{\infty}\Phi_n, \qquad |\omega\phi''(p_0)| \to \infty \tag{B.3}$$

with respect to the auxiliary asymptotic sequence

$$\begin{aligned}\{\phi_j\} &= \frac{1}{|\omega\phi''(p_0)|^j}\left\{\left|\int_{C_s}e^{\omega\phi(p)}\,dp\right| + \left|\int_{C_s}(p_b-p)^{1/2}e^{\omega\phi(p)}\,dp\right|\right. \\ &\quad \left. + \left|\int_{C_s}(p_b-p)^{3/2}e^{\omega\phi(p)}\,dp\right|\right\}.\end{aligned} \tag{B.4}$$

---

[1] In actuality it is $|\omega\phi''(p_0)|/\alpha_1^2| \to \infty$ to keep things dimensionless, but this is just constant factor.

There should be no confusion between the exponent ϕ *and the sequence of functions* $\{\phi_j\}$, *the latter always having a subscript.*

Proof 1 *Since the above sequences of functions* $\{\Phi_j\}$ *and* $\{\phi_j\}$ *are asymptotic, we only must establish that*

$$R = \lim_{\omega\to\infty} \left| \frac{u_z^{ref} - \sum_{j=0}^{N} \Phi_j}{\phi_N} \right| = \lim_{\omega\to\infty} \left| \frac{\mathcal{E}_N}{\phi_N} \right| = 0. \tag{B.5}$$

We start by recognizing that the functions $(p - p_L)A(p)$ *and* $(p - p_L)B(p)$ *are smooth (continuous and infinitely differentiable) in some region* D *surrounding the saddle point.*[2] *That this is true follows from the fact that we have factored out any nearby branch point or pole, while leaving distant critical points implicit in* A *and* B. *We see that the use of the approximations in equations (1.32) and (1.34) leads to errors of the form*

$$\begin{aligned} e_A^0(p) &= (p-p_0)(p-p_L)E_A^0(p) \\ e_B^0(p) &= (p-p_0)(p-p_L)(p-p_b)E_B^0(p) \end{aligned} \tag{B.6}$$

where $E_A^0(p)$ *and* $E_B^0(p)$ *are smooth in* D. *This leads to an error in approximating the integral of*

$$\mathcal{E}_0 = \int_{C_s} E_A^0 (p-p_0) e^{\omega\phi(p)}\, dp - \int_{C_s} E_B^0 (p-p_0)(p_b-p)^{3/2} e^{\omega\phi(p)}\, dp \tag{B.7}$$

where the factor $(p - p_L)$ *has cancelled out. We now see that there is one dominant point in the first integral* (p_0) *and two in the second integral* (p_0, p_b). *If we repeatedly expand the smooth terms about the dominant points,*[3]

$$\begin{aligned} E_A^j &= a_{1j}(p-p_0) + e_A^{j+1} \\ E_B^j &= b_{1j} + b_{2j}(p-p_b) + e_B^{j+1} \qquad j \geq 1 \end{aligned} \tag{B.8}$$

---

[2] See Appendix A for an estimate of the size of D.

[3] The expansion in equation (B.8) looks a little cryptic. Since there is only one dominant point for E_A^j, we need to expand in a power series about this point, rather than using the Lagrange polynomial which requires two or more distinct points.

where the top expansion is exact at p_0 *and the bottom is exact at* p_0 *and* p_b. *The above expansion leads us to the terms in the asymptotic sequence* Φ_j. *The error in the* j^{th} *term is then*

$$\begin{aligned} e_A^j &= (p-p_L)(p-p_0)^{j+1}E_A^j \\ e_B^j &= (p-p_L)(p-p_0)^{j+1}(p-p_b)^{j+1}E_B^j \end{aligned} \tag{B.9}$$

and so we can express the error in the partially expanded integral as

$$\mathcal{E}_j = \int_{C_s} E_A^j(p-p_0)^{j+1}e^{\omega\phi(p)}\,dp + (-1)^{j+1}\int_{C_s} E_B^j(p-p_0)^{j+1}(p_b-p)^{j+3/2}e^{\omega\phi(p)}\,dp. \tag{B.10}$$

Next we need to estimate the size of $\mathcal{E}_j$. *One can see that upon integration by parts* $j+1$ *times,*[4]

$$\mathcal{E}_j \le \frac{1}{|\omega\phi''(p_0)|^{j+1}}\left\{\left|\int_{C_s}\frac{d^{j+1}E_A^j}{dp^{j+1}}e^{\omega\tilde{\phi}(p)}\,dp\right| + \left|\int_{C_s}\frac{d^{j+1}}{dp^{j+1}}\left(E_B^j(p_b-p)^{j+3/2}\right)e^{\omega\tilde{\phi}(p)}\,dp\right|\right\}. \tag{B.11}$$

There also exist constants for the bounded region about the saddle D, such that

$$\begin{aligned} \left|\frac{d^{j+1}E_A^j}{dp^{j+1}}\right| &\le \xi_1, \qquad p\in D \\ \left|\frac{d^{j+1}}{dp^{j+1}}\left(E_B^j(p_b-p)^{j+3/2}\right)\right| &\le \xi_2|(p_b-p)^{1/2}| + \xi_3|(p_b-p)^{3/2}|,\ p\in D \end{aligned} \tag{B.12}$$

We can bound the size of $\mathcal{E}_j$ *with these constants, introducing asymptotically negligible errors (think of truncating and re-extending the contour* C_s*). Thus,*

$$\begin{aligned} \mathcal{E}_j \ \le\ & \frac{1}{|\omega\phi''(p_0)|^{j+1}}\left\{\xi_1\left|\int_{C_s}e^{\omega\tilde{\phi}(p)}\,dp\right| + \xi_2\left|\int_{C_s}(p_b-p)^{1/2}e^{\omega\tilde{\phi}(p)}\,dp\right|\right. \\ & \left. +\xi_3\left|\int_{C_s}(p_b-p)^{3/2}e^{\omega\tilde{\phi}(p)}\,dp\right|.\right\} + O(\omega^{-j-1-q}), \qquad q>0, \end{aligned} \tag{B.13}$$

the last term arising from the use of the bounding constants ξ_k *(and it can be neglected for large* ω*). It follows that*

$$R = lim_{\omega\to\infty}\left|\frac{\mathcal{E}_j}{\phi_j}\right| \ \le\ \lim_{\omega\to\infty}\frac{1}{\omega}\times \textit{frequency independent factor}$$

---

[4] Here we assume that the exponent is replaced with the first two terms of its Taylor expansion about p_0, $\phi \to \tilde{\phi}$. To make the resulting series valid for terms other than the first, one must include the truncated part of the exponent in the integrand $\exp(\omega(\phi-\tilde{\phi}))$ as a slowly varying factor and expand it like the other smooth terms.

$$= 0. \tag{B.14}$$

□

Appendix C

Effect of small perturbations on the function $W(w)$

Given that

$$i\omega(\tau - \tau_d)_\nu = \alpha + \beta_\nu, \quad \beta_\nu = O(1/\sqrt{\omega}), \quad \alpha = O(1) \tag{C.1}$$

and

$$W(w^\nu) = \frac{e^{\alpha+\beta_\nu}}{2\sqrt{\pi}} \int_{\alpha+\beta_\nu}^{\infty} \frac{e^{-t}}{\sqrt{t}} dt, \tag{C.2}$$

we can rewrite the integral in equation (C.2) as

$$W(w^\nu) = \frac{e^{\alpha+\beta_\nu}}{2\sqrt{\pi}} \left(\int_\alpha^\infty \frac{e^{-t}}{\sqrt{t}} dt - \int_\alpha^{\alpha+\beta_\nu} \frac{e^{-t}}{\sqrt{t}} dt \right). \tag{C.3}$$

Using the substitution $s = t - \alpha$, and then expanding the integrand for small s/α we get

$$W(w^\nu) = \frac{e^{\alpha+\beta_\nu}}{2\sqrt{\pi}} \left(\int_\alpha^\infty \frac{e^{-t}}{\sqrt{t}} dt - \frac{e^{-\alpha}}{\sqrt{\alpha}} \beta_\nu \right) + O(\beta_\nu^2), \tag{C.4}$$

from which it follows that

$$\frac{W(w^\nu)}{W(w^0)} = 1 + O(1/\sqrt{\omega}). \tag{C.5}$$

Bibliography

[1] M. Abramowitz and I. Stegun. *Handbook of Mathematical Functions*. Dover, 1965.

[2] K. Aki and P. G. Richards. *Quantitative Seismology*, volume 1. W.H. Freeman and Company, 1980.

[3] P. M. Bakker. Theory of edge diffraction in terms of dynamic ray tracing. *Geophys. J. Int.*, 102:177–189, 1990.

[4] C.M. Bender and S.A. Orszag. *Advanced Mathematical Methods for Scientists and Engineers*. McGraw-Hill, 1978.

[5] N. Bleistein. Uniform asymptotic expansions of integrals with stationary point near algebraic singularity. *Communications in Pure and Applied Mathematics*, 19(4):353–370, 1966.

[6] N. Bleistein and R. A. Handelsman. *Asymptotic Expansions of Integrals*. Dover, 1986.

[7] L. M. Brekhovskikh. *Waves in Layered Media*. Academic Press, 1980.

[8] V. Červený and F. Hron. The ray series method and dynamic ray tracing system for three-dimensional inhomogeneous media. *Bull. Seism. Soc. Am.*, 70:44–77, 1980.

[9] V. Červený and I. Pšenčík. Gaussian beams in two dimensional elastic inhomogeneous media. *Geophys. J. R. astr. Soc.*, 72:417–433, 1983.

[10] V. Červený and R. Ravindra. *Theory of Seismic Head Waves*. University of Toronto Press, 1971.

[11] G. H. Chan. *Seismic Diffraction from Wedges*. PhD thesis, University of Alberta, 1986.

[12] C. H. Chapman. Lamb's problem and comments on the paper 'on leaking modes' by usha gupta. *Pure Appl. Geophys.*, 94:233–247, 1972.

[13] C. H. Chapman and J. A. Orcutt. Computation of body wave synthetic seismograms in laterally homogeneous media. *Rev. Geophys.*, 23(2):105–163, 1985.

[14] R. V. Churchill and J. W. Brown. *Complex Variables and Applications*. McGraw-Hill, 1990.

[15] P. J. Davis and P. Rabinowitz. *Methods of Numerical Integration*. Academic Press, 1984.

[16] L. N. Frazer and J. F. Gettrust. On a generalization of filon's method and the computation of the osc illatory integrals of seismology. *Geophys.J.R.astr.Soc.*, 76:461–481, 1984.

[17] J. B. Gallop and F. Hron. Asymptotic solutions to cagniard's problem. *Geophys. J. Int.* submitted.

[18] J. B. Gallop and F. Hron. An example of the computation of edge diffracted waves. *Can. J. Expl. Geophys.* in press.

[19] J. B. Gallop and F. Hron. Diffractions and boundary conditions in asymptotic ray theory. *Geophys. J. Int.*, 5:47–53, 1998.

[20] C. W. Gear. *Numerical Initial Value Problems in Ordinary Differential Equations*. Prentice-Hall, 1971.

[21] B. Y. Gel'chinsky. Expression for the spreading function. *Problems in the Dynamic Theory of Seismic Wave Propagation*, 5:47–53, 1961 (in Russian).

[22] F. Gilbert and S. J. Laster. Excitation and propagation of pulses on an interface. *Bull. Seism. Soc. Am.*, 52(2):299–319, 1962.

[23] H. W. Guggenheimer. *Differential Geometry.* Dover, 1977.

[24] U. Gupta. On leaking modes. *Pure Appl. Geophys.*, 80:27–37, 1970.

[25] F. Hron and G. H. Chan. Tutorial on the numerical modelling of edge diffracted waves by the ray method. *Studia geoph. et geod.*, 39:103–137, 1995.

[26] F. Hron and J. D. Covey. Theory of seismic waves diffracted by the linear edges of seismic interfaces. Technical Report F88-E-13, Amoco Research Center, 1988.

[27] F. Hron and E. R. Kanasewich. Synthetic seismograms for deep sounding studies using asymptotic ray theory. *Bull. Seism. Soc. Am.*, 61:1169–1200, 1971.

[28] J. B. Keller. Geometrical theory of diffraction. *J. Opt. Soc. Am.*, 52(2):116–130, 1962.

[29] I. Y. E. Kireyeva and K. A. Karpov. *Tables of Weber Functions.* Pergamon Press, 1961.

[30] D. Klaeschen, W. Rabbel, and E.R. Flueh. An automated ray method for diffraction modelling in complex media. *Geophys. J. Int.*, 116:23–38, 1994.

[31] K. D. Klem-Musatov. *Theory of Seismic Diffractions.* Society of Exploration Geophysicists, 1994.

[32] K. D. Klem-Musatov and A. M. Aizenberg. The ray method and the theory of edge waves. *Geophys. J. R. astr. Soc.*, 79:35–50, 1984.

[33] W. Magnus and F. Oberhettinger. *Formulas and Theorems for the Functions of Mathematical Physics.* Chelsea Publishing Company, 1954.

[34] J. S. Ogilvie and G. W. Purnell. Effects of salt related mode conversions on subsalt prospecting. *Geophysics*, 61(2):333–348, 1996.

[35] R. A. Phinney. Propagation of leaking interface waves. *Bull. Seism. Soc. Am.*, 51:527–555, 1961.

[36] W. H. Press, S. A. Teukolsky, W. T. Vetterling, and B. P. Flannery. *Numerical Recipes in Fortran.* Cambridge University Press, 1992.

[37] R. E. Sheriff and L. P. Geldart. *Exploration Seismology: Data Processing and Interpretation*, volume 2. Cambridge University Press, 1983.

[38] N. S. Smirnova. On the problem of calculation of wavefields in the region of critical rays. In G.I.Petrashen, editor, *Problems in the Dynamic Theory of Propagation of Seismic Waves*, volume 8, pages 5–15 (in Russian). Nauka, Moscow-Leningrad, 1966.

[39] J. Stoer and B. Bulirsch. *Introduction to Numerical Analysis.* Springer-Verlag, 1993.

[40] C. J. Thomson. Corrections for critical rays in 2-d seismic modelling. *Geophys. J. Int.*, 103:171–210, 1990.

[41] E. Zauderer. *Partial Differential Equations of Applied Mathematics.* John Wiley and Sons, 1989.